INVESTIGATION OF GRAPHENE FORMATION FROM GRAPHITE OXIDE AND SILICON CARBIDE

A Thesis
Presented to
The Academic Faculty

by

Denis A. Sokolov

In Partial Fulfillment
of the Requirements for the Degree
Doctor of Philosophy in the
School of Chemistry and Biochemistry

Georgia Institute of Technology
May 2013

INVESTIGATION OF GRAPHENE FORMATION FROM GRAPHITE OXIDE AND SILICON CARBIDE

Approved by:

Dr. Thomas M. Orlando, Advisor
School of Chemistry and Biochemistry
Georgia Institute of Technology

Dr. Clifford L. Henderson
School of Chemical and Biomolecular Engineering
Georgia Institute of Technology

Dr. Facundo M. Fernandez
School of Chemistry and Biochemistry
Georgia Institute of Technology

Dr. Laren M. Tolbert
School of Chemistry and Biochemistry
Georgia Institute of Technology

Dr. Phillip N. First
School of Physics
Georgia Institute of Technology

Date Approved: [February 5, 2013]

To my family and friends

ACKNOWLEDGEMENTS

This work would have never been possible without my advisor Dr. Thomas M. Orlando, whose patience with a novice scientist was much appreciated. I am grateful for the guidance that he provided. My Thesis committee (Dr. Facundo M. Fernandez, Dr. Phillip N. First, Dr. Clifford L. Henderson and Dr. Laren M. Tolbert) deserves a special thank you. Their valuable suggestions helped shape my work.

I would like to say a special thank you to my parents (Lyudmila L. Sokolova and Aleksandr I. Sokolov) and grandparents (Lidia I. Kulikova, Mariya I. Sokolova, and Leonid A. Kulikov). I thank them for raising me to be the man I am now. I will never forget the sacrifices they made for me. My brother Dmitry A. Sokolov is a great motivator. His innovative spark always makes me more creative. My aunt, uncle and cousin (Galina I. Porshneva, Gennadij N. Porshnev and Sergey G. Porshnev) are wonderful people and we always had a great time at the countryside of Russia near my hometown Lipetsk. I am extremely grateful to Mark E. Matthews. I thank him for giving me the opportunity to attend a college in the United States of America. I would have never been where I am now without his support.

My wife Dr. Margaret Michele Dawley is the best motivation a man can have. Her strength and determination inspire me every day, and the completion of this Thesis would have been a long and windy road if not for her continuous encouragement. I enjoyed every moment of sitting across the table from her, writing my Thesis, while she was writing hers. Our two cats (Pumpkin and Pearlie) should be thanked as well for their consistent purrs of encouragement.

There are many other people that contributed to my development as a scientist. I thank my collaborators Dr. Alexandr Aleksandrov, Dr. Kristin Shepperd, Dr. Anton Sidorov, Dr. Christopher Rouleau and Dr. David Geohegan for being great sources of ideas and scientific reason. My past and present labmates must be thanked as well for their useful suggestions and feedback on many topics. They are Dr. Gregory Grieves, Dr. Jason McLain, Dr. Heather Abbott-Lyon, Dr. Babajide Olanrewaju, Dr. Christopher Lane, Dr. Doogie Oh, Michael J. Poston, Alice Johnson DeSimone, Joshua Symonds, Lan Sun, Irene Anestis Richard, Marcus Johnson, Torri Rose, Hannah Barks, Dr. Jianming Shi, Dr. Reuben Gaan, Dr. Chris Bennett and Dr. Claire Pirim. A note of gratitude is also due to my friends Dr. Dmitry V. Liskin, Robert and Susan Ainsworth.

I would like to thank the Georgia Institute of Technology cleanroom staff for being an excellent resource and for proving valuable training on numerous tools and instruments. I am also grateful to Georgia Institute of Technology Materials Research Science and Engineering Center for its continuous financial support of my work during my doctoral studies.

TABLE OF CONTENTS

LIST OF FIGURES

Page

SUMMARY

Graphene is a novel two dimensional material that is revolutionizing many areas of science and it is no surprise that a lot of effort is dedicated to its investigation. One of the major areas of graphene research is the development of procedures for its large scale production. Chapter 1 describes in detail approaches that are most prevalent for growing graphene. Among many recently developed methodologies, graphene oxide reduction stands out as a straightforward and scalable procedure for producing final material with properties similar to graphene. Graphene oxide reduction approaches are a rapidly developing area of research with new procedures frequently emerging.

One of the novel approaches for producing multilayer graphene is the laser reduction of graphite oxide. This work is presented in chapter 2 and it describes the entire production cycle: synthesis of graphite oxide, fabrication of graphite oxide thin films and a detailed explanation of the laser reduction procedures. Irradiation parameters for achieving best possible reduction are determined and the role of the background environment during the reduction process is investigated. It is determined that laser reduction has to take place in an oxygen-free environment. For pulsed laser systems, incubation doses at appropriate laser fluences are required to initiate reduction. Extensive material characterization with spectroscopic and microscopic techniques is presented as well. An extension of this work geared towards applications is presented in chapter 3. It is determined that the combination of laser reduced graphite oxide-unreduced graphite oxide produces a photosensitive material. The efficiency of light conversion into the electrical current is greatly dependent on the oxygen content of the underlying graphite

oxide. Sensors based on the laser reduced graphite oxide-low oxygen content unreduced graphite oxide exhibit best light sensing characteristics in the full visible light range.

Developing novel ways for reducing graphite oxide is an ongoing effort. Chapter 4 presents a new method for achieving complete reduction of graphite oxide for producing predominantly sp^2 hybridized material with a carbon to oxygen ratio of ~ 215. This approach is based on the irradiation of graphite oxide with a high flux 3 keV Ar ions in vacuum. Reduced material is characterized in detail with microscopic and spectroscopic techniques. It is determined that angle of irradiation greatly influences the final surface morphology of reduced graphite oxide. It is also concluded that ion energy and flux has a significant effect on the final carbon to oxygen ratio in addition to influencing the surface morphology.

Lastly, the study presented in chapter 5 investigates multilayer epitaxial graphene growth on silicon carbide ceramic in ultra-high vacuum conditions. Epitaxial graphene growth on silicon carbide is of immense technological relevance and understanding the mechanisms governing the formation of graphene layers is essential for being able to control the final properties of the grown material. Quadrupole mass spectrometry is utilized for characterizing the molecular and atomic species that sublime from silicon carbide during the high temperature epitaxial growth. The masses are monitored as a function of temperature and heating time. This work allows the determination of energy of silicon sublimation from silicon carbide. Final characterization of the prepared film is performed with X-ray photoelectron spectroscopy coupled with Ar ion depth profiling.

CHAPTER I

INTRODUCTION

1.1 Graphene – a novel two dimensional material

1.1.1 Background

Graphene in its pristine form can be described as a network of sp^2 hybridized carbon atoms arranged in a hexagonal network, similar to chicken wire (Figure 1.1). The first theoretical work describing the band structure of a single layer of graphite was published by Wallace in 1947 [3]. The first experimental observation of a graphite monolayer was by Boehm in 1961 [4]. The first measurements of the electrical properties of an isolated graphene sheet were performed by Novoselov and coworkers in 2004 [5]. The work by Novoselov and coworkers stimulated scientific interest in graphene, which led to the blossoming of the area of science dedicated to the interdisciplinary investigation of graphene's properties and discovery of its novel applications. This chapter will briefly introduce the reader to the area of science dedicated to graphene research and will explain its importance.

Graphene can be viewed as a starting building block for some of the carbon allotropes: zero-dimensional fullerene, one-dimensional nanotubes and three-dimensional graphite (Figure 1.1). In principal, these allotropes can be interconverted into each other, with some of the transformations being more readily achievable than others. Of all carbon allotropes, graphene can be most closely compared to carbon nanotubes, both in its structure and properties. Not surprisingly, graphene nanoribbon can be viewed as just unzipped single wall nanotube. This conversion was first achieved in 2009 [6]. The

reverse transformation has not being experimentally shown so far, despite several theoretical predictions [7,8]. Folding a nanographene to make a fullerene, though, has been experimentally demonstrated and the process has been observed with a transmission electron miscroscope (TEM) [9].

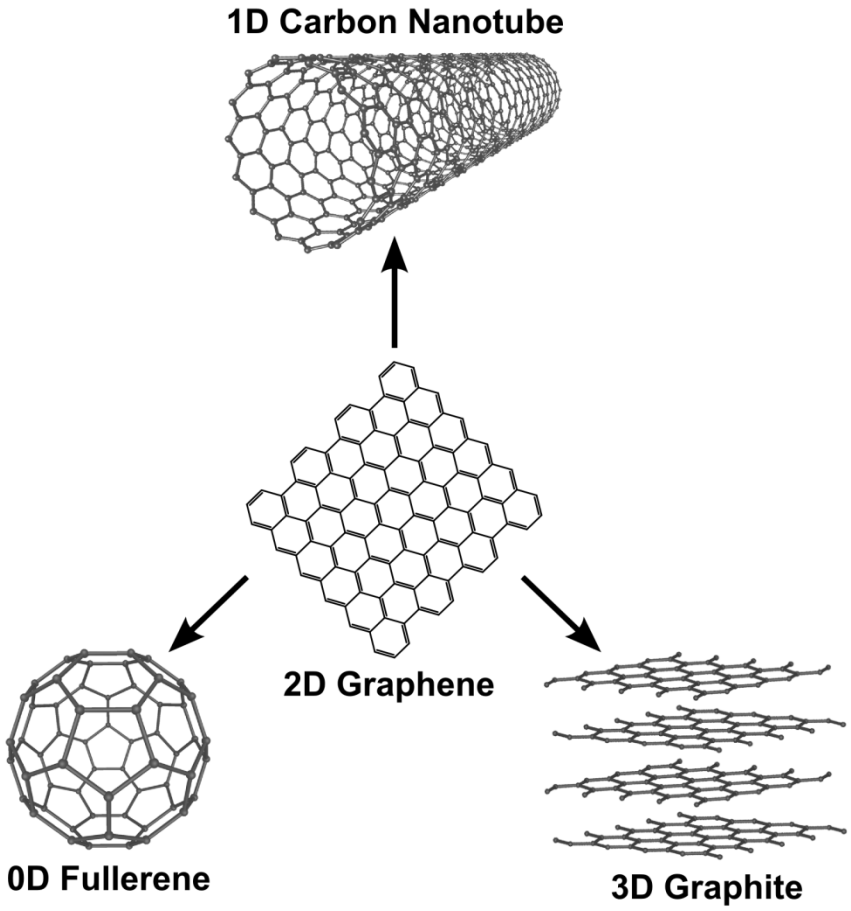

Figure 1.1: Graphene is a starting building material for fullerene, nanotube and graphite.

Due to the unique sp^2 hybridized hexagonal carbon network structure, graphene possesses properties that are unique from other materials. Specifically, graphene is reported to be the strongest material known to date with a breaking strength of ~ 42 N/m and a Young's modulus of ~ 1 TPa [10]. Thermal conductivity of graphene is remarkable

as well, with its measured value of ~ 5000 W m^{-1} K^{-1} [11] exceeding that of a ^{13}C enriched diamond (~ 3320 W m^{-1} K^{-1}) [12]. But the property that graphene is most sought after is its electrical characteristics. Due to graphene's unique electronic structure, it is capable of effectively conducting electrical charge, with mobilities reaching ~ 2×10^4 cm^2 V^{-1} s^{-1} at 4 K and ~ 1.5×10^4 cm^2 V^{-1} s^{-1} at 300 K [13].

Because of these characteristics as well as the technological and commercial potential that graphene holds it is not surprising that a lot of resources have been dedicated to the challenge of its production on a large scale. As a result, novel methods have been developed for producing both pristine and modified graphene. Both of these materials have significant value.

1.1.2 Production methods

The methods that are commonly used for producing graphene are as follows: mechanical exfoliation of graphite, epitaxial graphene growth on silicon carbide, chemical vapor deposition (CVD) growth on metals and reduction of graphene oxide. Section 1.2 in this chapter will discuss graphene oxide and its reduction in detail.

Mechanical exfoliation of graphene has been first achieved in 2004 by peeling individual layers of graphene from a piece of graphite using a sticky tape [5]. By repeating this process numerous times and then rubbing the residue left on the sticky tape onto the specially prepared substrate, a single layer of graphite has been isolated, observed by an optical microscope and its electrical properties investigated for the first time. The substrate that allows this direct optical visualization is prepared by growing ~ 300 nm of silicon dioxide on a silicon substrate. This combination of materials

produces the contrast necessary for observing graphene, even though it is an atomically thin material. Though this approach is suitable for academic investigation of graphene, it is not technologically relevant or viable for large scale production. At the time this chapter is written, the mechanical exfoliation approach has been also successfully applied for isolating individual single layers of other materials that exist in nature as bulk layered structures. The number of these materials is expanding every day, with the most relevant candidates for electronic applications being molybdenum disulfide and titanium disulfide.

At about the same time as the development of the mechanical exfoliation approach, a group of scientists at Georgia Institute of Technology has been perfecting another promising approach for a large scale production of graphene. The method, known as epitaxial graphene growth on silicon carbide (SiC) [14,15], relies on the precise control of parameters to achieve uniform growth of graphene. Depending on the desired number of graphene layers, the silicon carbide ceramic is heated to a temperature of ~1500 °C at a pressure of ~ 1×10^{-4} Torr, for various periods of time. The mechanism of graphene growth in this method is generally understood in terms of silicon sublimation and reorganization of the remaining carbon atoms to a lower energy state – graphene. This approach is viewed as most easily adaptable for the industrial implementation and device fabrication.

Several years after the introduction of the mechanical exfoliation of graphite, another strategy for graphene growth came to light – CVD graphene growth. It relies on the use of metallic substrates (Cu, Ni, Ru, Ir and Pt), carbon bearing precursor gases and high temperatures to grow graphene both in vacuum and in inert gas environments [2,16-19]. An interesting characteristic of this method is that it is possible to grow precise

number of graphene layers, depending on the metal substrate. This is explained in terms of carbon diffusion into the metal substrate; with copper, having low carbon solubility, producing primarily individual layers of graphene. The main challenge with this approach is that the quality of graphene is greatly dependent on the quality of the underlying metal substrate. Additionally, it is necessary to separate graphene from the metal substrate, if it is to be utilized. This step can introduce defects and impurities that have negative impact on the final properties of graphene.

Last but not least, the method for graphene production that will be greatly discussed in this Thesis is the reduction of graphene oxide and graphite oxide. Section 1.2 of this chapter will introduce this material and the methods currently employed for producing graphene-like materials from graphene oxide and graphite oxide.

1.1.3 Applications

Investigation of graphene has led to the development of numerous applications that use it directly or in conjunction with other materials. Academic studies that bring unique properties of graphene to light are fueling this process. Complete review of all possible applications is beyond the scope of this chapter, but briefly some of them will be mentioned in this section.

As mentioned in Section 1.1.1, the main interest in graphene is for its high electrical conductivity, therefore the use of graphene sheets as transparent electrodes with very low electrical resistance is of a great interest [2,20,21]. Naturally, most of the graphene production methods that are scalable, such as epitaxially grown graphene on

silicon carbide, CVD graphene and reduced graphene oxide have direct relevance for this application.

Mechanical strength of graphene is leading to the creation of composites that incorporate individual graphene flakes to produce materials with higher strength to weight ratios [22-24]. Additionally, these composites can have an added benefit of being conductive. An offshoot of this approach is the creation of the carbon based conductive inks [25]. This can lead to being able to print electrical circuitries on any insulating flexible substrate.

Graphene's strength and its chemical inertness are prompting researchers into investigating the use of graphene as a coating on metallic substrates to prevent corrosion due to the environmental exposure [26-28]. This has direct relevance to extending the lifetime of the iron based infrastructure. The method of coating these structures with graphene is largely based on growing graphene on these metallic structures from carbon bearing precursor molecules at elevated temperatures in inert environments. Alternatively, coating metal structures directly with a pre-grown graphene film can also be accomplished.

More recently graphene has found its uses in solar cell applications. When a single layer of graphene is deposited on a n-doped silicon substrate and exposed to AM1.5 illumination, the efficiency of power conversion has been reported to achieve 8.6% [29]. This also leads to the development of broadband light sensors, which are extremely efficient even in infrared region [30,31]. This high sensitivity in the infrared range can lead to the development of better night vision equipment as well as improved

space based infrared telescopes. Graphene based biosensors and gas sensors are also in development with many promising results [32-36].

Each year of research of graphene technology leads to the abundance of novel applications that, when fully developed, can have a significant and lasting impact on societies throughout the world, leading to improvements ranging from energy conversion and storage to inhibiting corrosion of iron based infrastructure.

1.2 Graphene oxide

1.2.1 Background

Graphene oxide is a single layer of oxidized graphite, just like graphene can be thought of as a single layer of graphite (Figures 1.2b and 1.2c). Oxidized graphite is generally referred to as graphite oxide (GO). The first reported synthesis of GO was by Brodie in 1858 [37]. Hummers and Offeman in 1957 modified the procedure to make it safer [38]. To this day this synthetic procedure, which is now generally referred to as Hummers method, remains one of the primary ways of producing bulk GO, though there are other methods that have been also developed and will be briefly described in the next subsection 1.2.2.

Graphene oxide, in its as prepared form, has a structure similar to that of graphene, except that most of the sp^2 hybridized carbon atoms become sp^3 hybridized due to the introduction of the oxygen containing functional groups (Figure 1.2a). Though there are variations in the amounts and types of the functional groups introduced into graphene upon oxidation, generally the following functionalities are present: hydroxyl, epoxy, carbonyl and carboxyl. The structure of graphene oxide is still debated, but it is

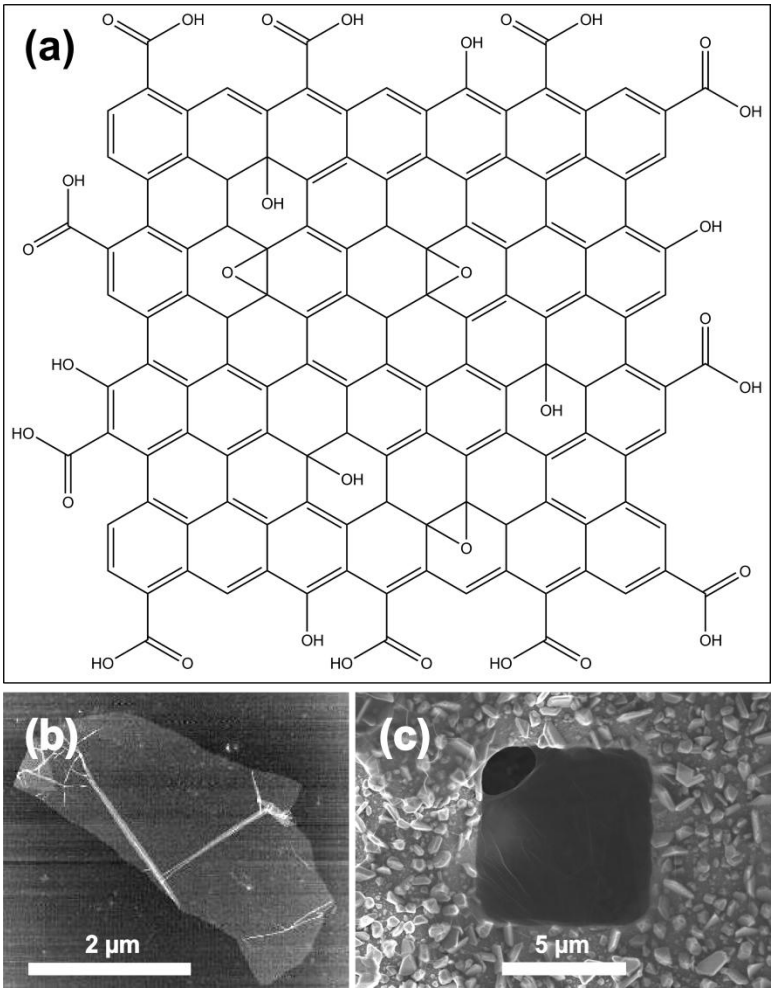

Figure 1.2: (a) Proposed graphene oxide structural model [1]. (b) AFM image of a single layer graphene oxide on silicon substrate. (c) SEM image of a suspended sheet of multilayer graphene oxide.

generally agreed upon that epoxy and hydroxyl groups are present above and below the basal plane of graphene oxide; carbonyl and carboxyl functionalities decorate the edges. These polar groups significantly change both chemical and electronic properties of graphene oxide, compared to graphene. Due to the polar nature of the attached functional groups, GO can form stable colloidal dispersions in water and other polar solvents. Because of the same functional groups, GO can be a wide-bandgap semiconductor or an insulator with a bandgap as large as ~4 eV, depending on the level of oxidation [39].

Additionally, sheet resistance of GO is $\sim 10^{10}$ Ω/sq [40] compared to ~ 30 Ω/sq for pristine graphene on SiO_2 [41]. Because of these inferior electrical conductivity values, oxygen containing functionalities have to be removed from GO (the process is termed graphene oxide reduction), if this material to be used for graphene production.

Though graphite oxidation has been studied due to the technological importance of this reaction, the value of GO was not recognized until 2006 when the search for new ways of making graphene prompted scientist to look into chemical approaches for its production. For the first time researchers determined that GO can be readily exfoliated in water to form single layer graphene oxide sheets which can be deposited on any substrate and, when most of the oxygen containing functionalities are removed, the sheets can have properties resembling those of graphene [42]. Other studies soon followed, exploring additional ways of synthesizing, exfoliating and reducing GO. Research on this subject is ongoing and this Thesis will introduce several new ways for reducing GO.

1.2.2 Production methods

As mentioned in subsection 1.2.1, GO was first synthesized by Brodie. The procedure involves a reaction between graphite powder, potassium chlorate ($KClO_3$) and fuming nitric acid (>90% HNO_3) [37]. Due to the nature of the reactants, the procedure is reported to be inherently dangerous, with a possibility for an explosion. Hummers and Offeman modified the procedure to make it safer [38], by reacting graphite with sodium nitrate ($NaNO_3$), potassium permanganate ($KMnO_4$) and concentrated sulfuric acid (H_2SO_4).

Because of an increased interest in GO, new procedures for its production are frequently introduced. One of the procedures excludes sodium nitrate from the reaction mixture. The method calls for an increased amount of $KMnO_4$, and reaction has to be performed with a 9:1 mixture of sulfuric/phosphoric acids (H_2SO_4/H_3PO_4) [43]. The procedure produces GO with and increased oxygen content compared to the one produced with the Hummers method. Recently, a method that does not rely on the use of strong oxidizing agents has been demonstrated. This approach produces edge-carboxylated material, in many of its properties similar to GO, by ball milling graphite in the presence of dry ice in a sealed container [44]. The advantage of the method is in its edge-selective functionalization of graphite - the basal plane remains unoxidized, thus milder reduction procedure have to be performed.

To produce graphene oxide from any of the previously mentioned methods, graphite oxide has to be exfoliated in solution. This is generally accomplished via mild sonication in water or other polar solvents. The resulting solution, when diluted, contains predominantly single layer graphene oxide sheets.

1.2.3 Reduction

Previous sections provided introduction for why GO is important for graphene research and also the reader was introduced to several currently widely used methods for making GO. Due to the abundance of oxygen containing functional groups in GO, the material has properties that are too dissimilar from graphene. Removal of these functional groups is an essential step for producing highly conductive material that closely resembles graphene. There are many ways for achieving this objective, with some

procedures being better than others, and a brief overview of these methods is presented below.

Chemical reduction approaches are widely used for removing oxygen containing functionalities from graphene oxide. Reduction with hydrazine hydrate ($NH_2NH_2 \bullet H_2O$) of GO solution [42] and with hydrazine vapor of GO thin films [43] are most commonly used methods. One of the disadvantages of using hydrazine reduction method is the introduction of heteroatomic impurities, specifically in the form of covalently bound nitrogen species (e.g. hydrazones, amines, aziridines) which can act as n-type dopants [45]. Reduction with sodium borohydride ($NaBH_4$) [44] is advantageous over hydrazine approach, because no impurity incorporation occurs. Unfortunately the overall reduction efficiency with sodium borohydride is not as high as with hydrazine. Another approach that rivals the hydrazine reduction method, yet lacks its drawbacks is based on treating GO films for 1 h at 100 °C in 55% hydroiodic (HI) acid [46].

Thermal reduction of GO is another widely used approach. Unlike chemical reduction, thermal reduction can be subdivided on bulk and nanoscale reduction. Bulk reduction is generally performed in vacuum [47,48] or in an inert environment [49] at temperatures as high as 1900 °C to achieve the best possible quality of the reduced material. Nanoscale reduction is performed with a heated atomic force microscope (AFM) tip [50] at temperatures approaching ~1100 °C. Thermally reduced graphite oxides, depending on the reduction temperatures, vary in their final oxygen content and the sheet resistance values. Overall, GO films that are thermally reduced exhibit better characteristics then their chemically reduced counterparts. This is primarily due to a more complete removal of the oxygen containing functionalities.

Photoreduction approaches encompass both broadband and narrowband light sources. Broadband photoreduction is generally achieved with either a xenon discharge lamp, camera flash or solar radiation [51-53]. The quality of reduced GO greatly depends on the intensity of the irradiation. Narrowband light source photoreduction is performed with either continuous or pulsed laser systems with a variety of pulse widths (ranging from nanosecond to femtosecond) [54-60]. Laser reduction will be discussed in great detail in chapter 2.

Non-thermal and non-chemical approaches based on radiation processing of GO are also emerging as promising methods for producing graphitic materials from graphite oxide. So far, these techniques have been limited to electron [61,62] and plasma [63,64] irradiation. Chapter 4 of this Thesis will describe a highly efficient Ar ion beam GO reduction approach. To the best knowledge of this Thesis' author, no prior work has been done on ion beam GO reduction.

1.2.4 Applications

An increased interest in graphene also heightened researchers' interest in graphene oxide and graphite oxide. Unique applications for these two materials emerge with surprising frequency, which at times rival that of graphene itself. The areas where graphene oxide and graphite oxide are found to be useful can be categorized into broad categories: transparent conductive films, composites, energy harvesting/storage, medicinal and environmental applications. This list is by no means a comprehensive review of all possible application – it is rather a glimpse of where the research is heading at this point in time.

The use of thin films of GO as transparent conductive coatings is a logical choice, since it is easy to produce well dispersed single layer graphene oxide films that can be deposited on any substrate (rigid or flexible). As previously mentioned, graphene oxide has a high sheet resistance, which renders it primarily insulating. With a continuous improvement of the reduction protocols, full restoration of the conductive properties to graphene oxide is within sight. The hydroiodic acid reduction procedure already produces films with sheet resistances of ~ 1.6 kΩ/sq [46]. The laser reduction approach, described in chapter 2 of this Thesis as well as the corresponding peer-reviewed publications, demonstrates methods for producing reduced graphite oxide films with sheet resistances of ~ 100-500 Ω/sq [57,60].

Due to a rather high Young's modulus of graphene oxide (~ 207.6 GPa) [65] and its ease of blending with many polymers, graphene oxide is a great choice for improving mechanical and electrical properties of these materials. Depending on whether the final composite needs to be conductive or remain insulating, the graphene oxide additive can be either reduced or remain unreduced. Recent examples of work in this area produced conductive hydrogel materials [66,67].

Energy harvesting and storage applications of graphene oxide and graphite oxide are one of the most rapidly developing areas of research. Recently published reports on the use of laser reduced GO as supercapacitors [68,69] pave the way for future development of the GO based energy storage technology. Chapter 3 of this Thesis presents an approach for converting light energy to electrical current with laser reduced GO without the use of any additional hybrid materials. Other reports also demonstrate the use of reduced GO for solar cell applications [70-72].

Medicinal applications of graphene oxide and graphite oxide are just beginning to be investigated. Recent reports indicate promising application for graphene oxide as an effective antibacterial agent, disrupting bacterial activity by causing membrane and oxidation stress [35,73,74]. Cellular imaging and drug delivery with the use of graphene oxide are other rapidly developing applications [75,76]. Cellular imaging with graphene oxide is possible due to its inherent photoluminescence in the visible and infrared regions. Drug delivery is achieved through an additional functionalization of the sheets to render them biocompatible. The sheets can be also loaded with cytotoxic drugs, the release of which is initiated by the pH-sensitive release mechanism [76]. This targeted drug delivery can be further enhanced when graphene oxide sheets are loaded with magnetic nanoparticles, which would allow the sheets to be easily delivered to the targeted location in the body [77-79]. Of course, effects of graphene oxide and its derivatives will have to be carefully examined, if they are to be safely used as therapeutic delivery agents.

Environmental applications of GO hold tremendous promise as well. A recently published report indicates the high sorption affinity of graphene oxide towards highly toxic radionuclides, which allows for their rapid removal from contaminated water [80]. The report indicates high removal efficiency of actinides, including Am(III), Th(IV), Pu(IV), Np(V), U(VI) and typical fission products Sr(II), Eu(III) and Tc(VII). Similar high removal efficiencies with graphene oxide composites are observed for arsenic as well [81,82].

1.3 Thesis Organization

The remaining chapters of the Thesis are organized as follows. Chapter 2 will introduce the reader to the GO laser reduction approach. Careful spectroscopic, microscopic and electrical characterization of GO before and after laser reduction will be presented. Mechanism of laser reduction is investigated as well. Chapter 3 will build on the laser reduction work and will introduce a novel GO-laser reduced GO light sensing device. The effects of the oxygen content of the starting GO substrate on the efficiency of laser reduced GO light sensing will be examined. Chapter 4 focuses on the novel and highly efficient Ar ion beam GO reduction approach that has not been previously seen in the literature. Extremely high carbon to oxygen ratio of ~ 215 is achieved for the reduced material, compared to the ~ 2.37 of the untreated GO. Careful spectroscopic, microscopic and electrical characterization of the reduced material is performed. Chapter 5 is a related study on the multilayer graphene growth on silicon carbide substrate. Quadrupole mass spectrometric (QMS) investigation of the subliming species is performed, and their evolution as a function of growth time and temperature is monitored. The final films are characterized with Raman and X-ray photoelectron spectroscopy (XPS), and the distribution of carbon and silicon species within the film is evaluated with XPS depth profiling. Chapter 6 will provide concluding remarks for the performed work and its broader application will be suggested.

CHAPTER II

LASER INDUCED GRAPHITE OXIDE REDUCTION[1,2]

2.1 Introduction

As the motivation for reproducible, inexpensive growth strategies for macroscale graphene production continues to intensify, synthetic chemistry approaches have emerged as appealing alternatives to methods that require (ultra) high vacuum pressures or cleanroom facilities. Laser reduction of graphite oxide has emerged as one of the promising methods for producing high quality graphitic materials and several groups have been investigating this photoreduction approach [54-59]. Even though many GO reduction methods have been reported so far, very few groups have demonstrated definitive graphene formation from GO as verified by observation of the characteristic G' peak in the Raman spectra [48,52,57] and a corresponding low sheet resistance.

In this chapter, a technique for the production of the high-quality multilayer graphene features from direct laser irradiation of graphite oxide using both CW and pulsed nanosecond laser (248, 355 and 532 nm) is described. Laser reduction approaches that rely upon the use of inert background gases have been shown to achieve the best reduction of graphite oxide as verified with Raman spectroscopy [57]. This aspect of the GO laser reduction is explored in detail in subsection 2.4.3 and the characterization of the laser-produced features to verify their graphitic nature is described in subsections 2.4.1 and 2.4.2.

[1] Reprinted with permission from [57]. Copyright 2010. American Chemical Society.
[2] Reprinted with permission from [60]. Copyright 2013. Elsevier.

In addition to conventional lasers, pulsed excimer lasers have been enabling tools at the forefront of laser processing that includes state-of-the-art lithographic nanopatterning, where their deep ultraviolet (UV) wavelengths, coupled with new interferometric techniques [83], have overcome previous concepts of optical lithography limitations to routinely allow the fabrication of feature sizes well below 100 nm [84,85]. In the case of the graphite oxide reduction, the strong laser-induced electric fields and deep ultraviolet (UV) wavelengths can provide electronic excitation and non-thermal desorption pathways for the oxygen functionalities as well. Since fully oxidized GO has a strong absorbance at 5.37 eV (231 nm) [86], it was also natural to extend the process to 4.99 eV (248 nm).

In subsection 2.4.3 248 nm excimer laser light is used to examine the role of pulsed deep-UV reduction of GO. Micro-Raman spectra, X-ray photoelectron spectroscopy (XPS) spectra, laser-pulse and power dependence data are presented in section 2.4. These results collectively demonstrate that the use of a high purity inert background gas or a vacuum environment in conjunction with the appropriate number of incubation laser pulses is the key to successful laser reduction of graphite oxide. It is determined that the very low oxygen content (~ 2-4%) on/in the graphene lattice produced via laser irradiation of GO results in a minimal disruption of the graphene structure. Mechanism of the laser induced GO reduction and the potential utility of this approach in device fabrication strategies is discussed in subsections 2.4.4 and 2.4.5. Merging of the well-established excimer laser lithographic techniques with the laser based approaches for GO reduction allows microscale patterning and will allow fabrication of graphene features with nanoscale resolution in the near future.

2.2 Sample preparation

Graphite oxide was synthesized using a modified Hummers method by reacting graphite powder (325 mesh, Alfa Aesar) with sulfuric acid (H_2SO_4), potassium permanganate ($KMnO_4$) and sodium nitrate ($NaNO_3$) [37,38]. The reaction time was increased to 7 days to allow for a complete oxidation of graphite. The final product was purified through the cycles of dilution with nanopure water followed by centrifugation. The purification procedure was repeated until the solution reached pH 7. The graphite oxide solution was then concentrated using centrifugation and was stored in a brown glass container to prevent exposure to light. Concentration of the stock solution (~ 3.115 mg mL^{-1}) was determined by weighing a dried GO film produced from a known volume of the concentrated GO solution. Thick GO films were produced with a 47 mm diameter high pressure filtration funnel (Pall Corporation). The thickness of the produced films depends on the concentration of the graphite oxide solution. For these experiments 5 mL of concentrated GO solution was pipetted out and mixed with enough deionized water to make a 50 mL solution. The solution was pressure-filtered through a Whatman 47 mm nylon filter membrane with 200 nm pores at 170 psi of head pressure. The filtered graphite oxide on the nylon membrane was either dried in a Drierite desiccator for 48 hrs or for 24 hours at 105 °C in an oven to produce uniformly thick free standing GO films. These films were approximately 5-8 μm thick and were stored in a dessicator prior to being used. These two drying methods resulted in a ~ 29% oxygen content GO film.

For some of the experiments, samples with lower oxygen content were produced by heating graphite oxide films at 150 °C for 24, resulting in a graphite oxide with ~ 18% oxygen content. To produce samples with ~ 10% oxygen content, graphite oxide films

were heated at 500 °C in vacuum (~ 1×10^{-6} Torr) for 2 hours. These films were used in the evaluation of the reduction of graphite oxide with laser irradiation.

It is necessary to clarify that in the literature there appears to be a wide discrepancy as to the exact amount of oxygen present in GO. The variations might arise because of the drying and storage procedures utilized by the experimenters. In this work, by following the experimental procedure outlined above, the starting GO films always contained identical amounts of oxygen (~ 29%) as determined by XPS analysis (the typical XPS detection limit ranges between 0.05-0.1 atomic percent for all elements). Due to the ease of GO partial photo- and thermal reduction, it is necessary to protect both the solution and dried powder from exposure to ambient light and temperatures in excess of 105°C, unless it is desired to obtain samples with decreased oxygen content.

2.3 Experimental setup

In order to achieve best quality reduced material, graphite oxide laser reduction has to be performed in oxygen-free environments. This can be readily achieved by irradiating GO either in a gas flow cell, purged with an inert gas, or in a vacuum chamber. The schematic diagram of the experimental setup used for the reduction of GO in a gas flow cell is shown in Figure 2.1. The gases that are evaluated include nitrogen, argon, helium and ambient air. Gas flowing can be accomplished with a precision mass flow controller or direct purging with ~ 5 psi of gas pressure through the gas inlet. The desired outcome is to evaluate what role the background gases play in improving the GO reduction process. Presumably, their main contribution is in the decrease of the oxygen

concentration in the gas flow cell during the laser irradiation, which improves the quality of the laser reduced GO.

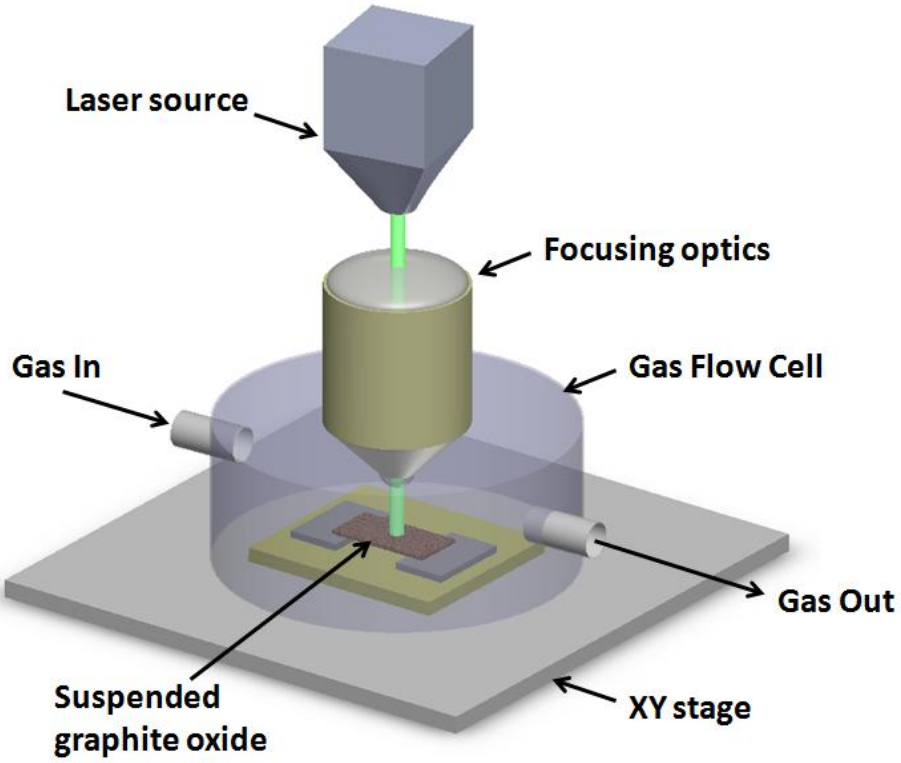

Figure 2.1: Experimental setup for the CW laser irradiation of GO in inert gas environment

A complementary GO laser reduction approach is to perform irradiation of GO in vacuum environments. The experimental setup for the irradiation of GO in vacuum is similar to the one used for the gas flow cell experiments, except the gas flow cell is replaced with a vacuum chamber evacuated with vacuum pumps to pressures as low as $\sim 1 \times 10^{-6}$ Torr. The laser light is delivered to the sample through the quartz viewport, which has excellent transmission characteristics both in the utraviolet and visible wavelength ranges.

For the laser reduction experiments, several laser sources have been evaluated including continuous and pulsed systems. Continuous wave laser, in the form of a laser diode with an excitation wavelength of 532 nm and 20 mW power, has been used for the reduction of GO in the inert-gas purged gas flow cell. The laser light was delivered to the sample through the 20× microscope objective. Pulsed Nd:YAG laser system (pulse width ~ 9 ns) was used for evaluating the reduction of GO in a gas flow cell as well. Experiments involving nanosecond Nd:YAG laser system were performed with an unfocused laser beam with a repetition rate of 20 Hz. KrF excimer laser system was used for irradiation of graphite oxide both in vacuum and in inert gas environments. A 10 × 10 mm aperture was imaged onto the sample at approximately 5:1 reduction using a projection beamline, and produced a rectangular spot on the GO sample that was ~ 1.8 × 1.98 mm. The KrF laser with a 248 nm wavelength and a pulse width of ~ 25 ns was operated at a repetition rate of 1 Hz, and an attenuator was used to achieve laser fluences that ranged from 60 to 400 mJ cm^{-2}. Three experimental conditions were employed to promote a reducing environment: high vacuum (~ 10^{-6} Torr), low vacuum (~ 9.8×10^{-2} Torr), and flowing (500 sccm) ultrahigh purity N_2. The advantage of pulsed laser systems is in the ability to evaluate the reduction of graphite oxide on a pulse by pulse basis and in achieving tunable wavelengths and laser fluences. Additionally, energy is delivered in short bursts resulting in a minimal heating of the sample, especially when shorter wavelengths are utilized.

2.4 Results and Discussion

2.4.1 Raman characterization

Raman spectra were acquired with a Bruker Senterra micro-Raman spectrometer (~ 9 cm^{-1} spectral resolution) using a 532 nm excitation wavelength and a 20× objective (Olympus M Plan 20X/0.40 ∞/0). Micro-Raman mapping was performed through a 100× objective (Olympus M Plan 100×/0.90 ∞/0). The laser power was attenuated to 2 mW. At this low level, laser-induced reduction and damage of the GO surface is negligible.

For the sake of comparison, Raman spectral signatures from highly oriented pyrolytic graphite (HOPG) are shown in Figure 2.2a. Two major peaks are assigned to the G mode (~ 1590 cm^{-1}) and the G′ mode (~ 2720 cm^{-1}). The G mode is the in-plane vibration of the carbon atom sp^2 network. This one phonon process involves E_{2g} optical phonons near the Γ point [87]. The G' mode is formed as a result of a two-phonon resonant scattering process. Though the D-band is not present in HOPG and defect free samples, the G' feature is always observed with widths defined by the thickness and stacking order along the c-axis. For single layer graphene, a single Lorenztian line shape centered at 2690 cm^{-1} can indicate electronic structure that is dominated by Dirac-Weyl dispersion [87]. It is therefore accepted as one of best optical signatures regarding the presence of graphene.

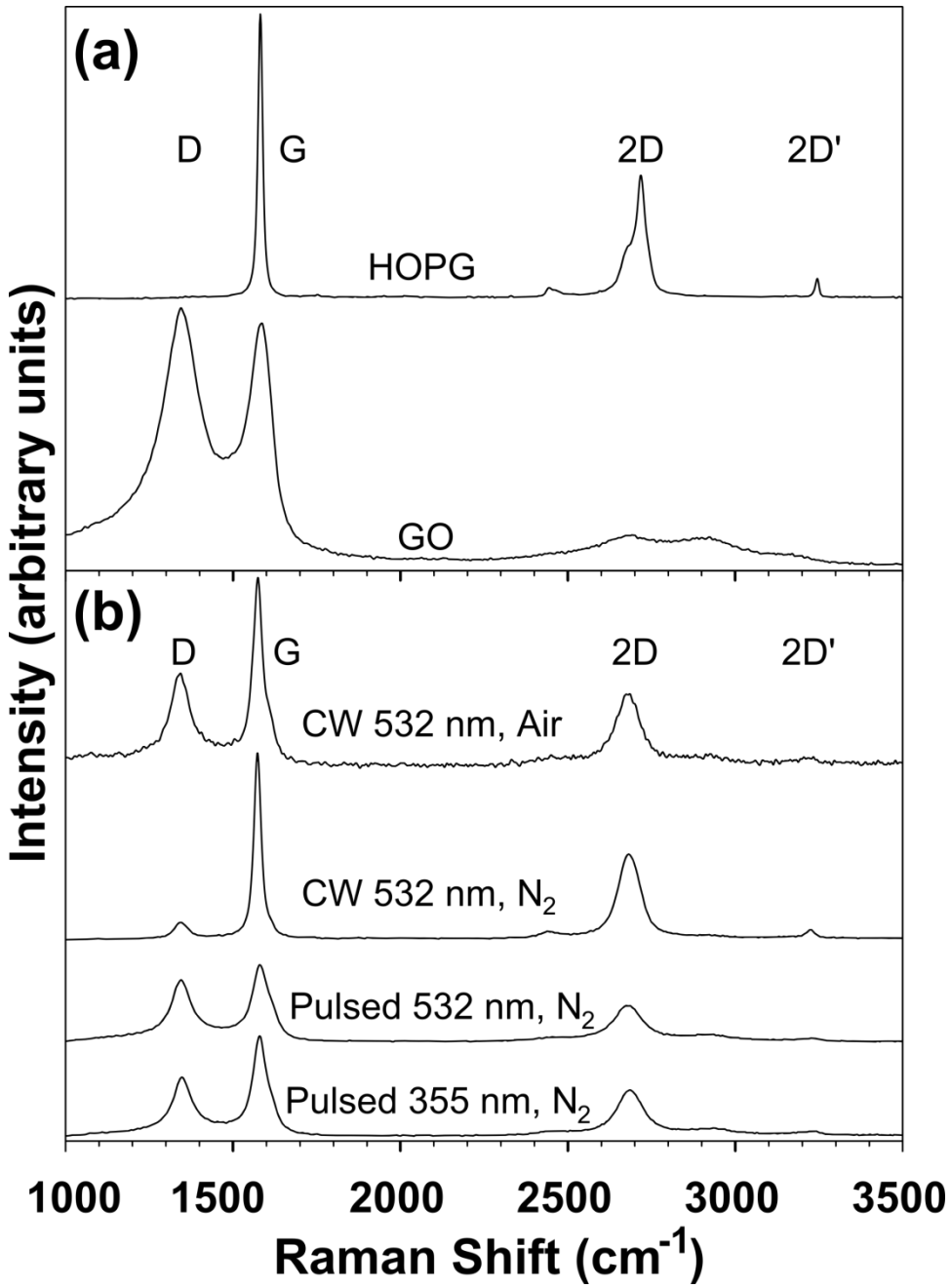

Figure 2.2: (a) Raman spectra of HOPG and a graphite oxide (GO) flake. (b) Raman spectra of GO after treatment with CW (20 mW at 532 nm) excitation in air and N_2 background and pulsed (~ 5 mJ/pulse, 9 ns, 20Hz) 532 and 355 nm laser excitation in N_2.

The Raman spectrum of GO is also shown in Figure 2.2a. It is vastly different than that from HOPG. Specifically: i) the G-band is much broader and blue shifted (~ 5 - 10 cm^{-1}); ii) there is a strong D-band at 1345 cm^{-1}; and iii) the G' band is nearly absent. These dramatic changes are correlated with structural changes and defects associated with the hydroxyl and epoxy groups in the basal plane and a variety of alkyl and oxygen-containing functional groups terminating the edges. Figure 2.2b shows the Raman spectrum of GO irradiated with a CW 532 nm beam in the presence of ambient air. The G'-band is observed and there is a narrowing of the G-band as well as diminution of the D-band. When using N_2 background gas, the G'-band is further enhanced, the G-band is much narrower and the D-band is nearly removed. Figure 2.2b also shows the Raman spectra of GO irradiated with pulsed 532 and 355 nm photons in N_2 background. Formation of the G'-band and G-band narrowing also occurs. However, the D-band feature, though reduced relative to untreated GO, remains independent of the laser flux. This indicates an intrinsic difference in the defect density and material quality relative to that formed using CW excitation.

Since the width of the G' feature can yield valuable information regarding the graphene thickness, Figure 2.3 shows a detailed view of the measured G' band for the CW 532 nm laser reduced GO in N_2 environment. The primary peak can be fit with a single Lorentzian with a full width at half maximum (FWHM) of ~ 65 cm^{-1}. The FWHM for mechanically exfoliated graphene supported on a SiO_2 surface is known to be ~ 30 cm^{-1} [88]. According to the width and thickness correlation, the measured FWHM value implies a multilayer graphene thickness.

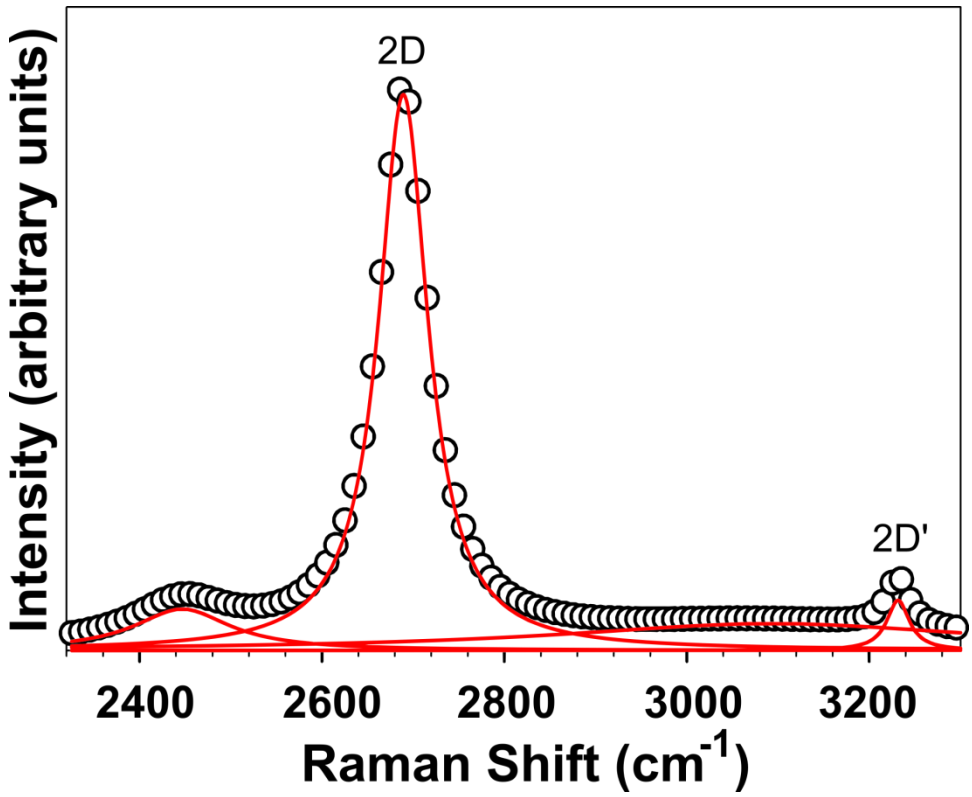

Figure 2.3: G' feature obtained in the bottom of the depression after CW 532 laser irradiation of graphite oxide. The peak is well fit by a single Lorentzian and the FWHM indicates the presence of multilayer graphene.

Figure 2.4 represents the typical Raman spectra obtained for unirradiated graphite oxide and excimer laser-reduced graphite oxide in high vacuum after 32 pulses at ~ 138 mJ/cm^2. Figure 2.4 inset shows GO reduction as a function of the number of laser pulses at ~138 mJ/cm^2 laser fluence. The spectra were normalized to the G peak. In the untreated graphite oxide two main peaks were observed, D (~ 1351 cm^{-1}) and G (~ 1590 cm^{-1}). Due to the sp^3 hybridization nature of the graphite oxide carbon bonds, the D peak is very prominent. Upon excimer laser irradiation, the D peak position is shifted by ~ 9 cm^{-1} to ~ 1342 cm^{-1} and the intensity is greatly reduced; the G peak position is shifted by ~ 25 cm^{-1} to ~ 1575 cm^{-1} and a prominent G' peak grows at ~ 2672 cm^{-1} indicating production of graphitic features.

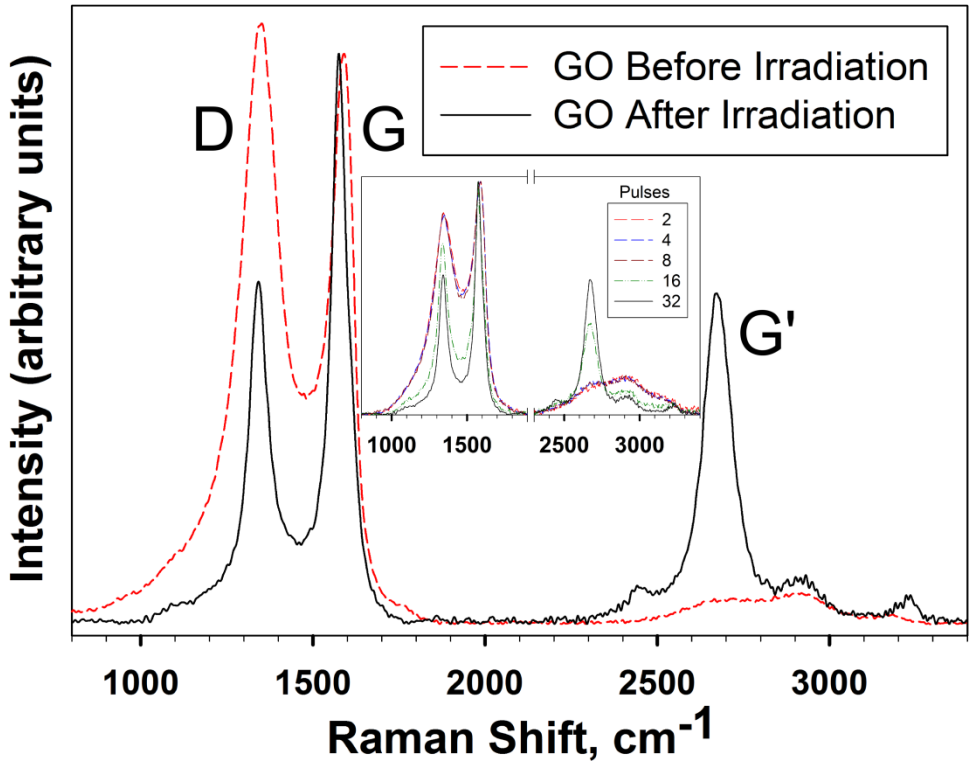

Figure 2.4: Typical Raman spectrum of untreated GO (red curve) compared with a spectrum of excimer laser-reduced GO (black curve) produced with 32 pulses at ~138 mJ/cm^2 laser fluence in high vacuum (~10^{-6} Torr). The inset is the pulse dependence of GO reduction at 138 mJ/cm2 in high vacuum (~10-6 Torr).

This G' peak can be fit with a single Lorentzian with a typical FWHM between ~ 50-65 cm^{-1} [57]. Previous work has indicated that the G' peak with a single Lorentzian profile can reveal the presence of turbostratic graphite, which is composed of multiple randomly oriented graphene sheets [89,90]. The presence of the D peak in the laser-reduced graphite oxide spectrum can be attributed either to the remaining oxygen species present after the reduction or possibly to the defects associated with the edge scattering in the graphene sheets. Alternatively, due to the laser reduced layer being directly on top of graphite oxide, the D band can be partially attributed to the Raman scattering from the underlying GO support. Additionally, Raman spectroscopy can be used to estimate the mean domain sizes or interdefect distances $L_a(nm)$ in graphene from the empirical

relationship $L_a(nm) = (2.4 \times 10^{-10})\lambda_l^4(\frac{I_D}{I_G})^{-1}$, where λ_l is the probe laser wavelength in nanometers and I_D and I_G are the integrated Raman intensities of the D and G bands [91,92]. From Figure 2.4, the L_a values of 18.2 nm and 31.5 nm were calculated for the untreated and the laser reduced graphite oxide, respectively. An increase in the L_a value indicates a transition of the laser-reduced graphite oxide to a more ordered state with fewer defects [92].

2.4.2 XPS characterization

XPS spectra were collected with a Thermo Scientific K-Alpha XPS system using an Al Ka X-ray source. The spot size of the X-ray beam was set to 200 μm. XPS is often used as a technique for verifying reduction of graphite oxide. XPS is capable of quantitative measurement of material composition and elucidating the chemical environment surrounding atoms by measuring core level shifts, which are affected by bonding states. Since it is difficult to extract detailed information regarding defects and structure within the graphene lattice, XPS analysis is generally more useful when done in conjunction with Raman spectroscopy. Collectively these two approaches can provide a more definitive verification of graphene formation from GO. Figures 2.5 and 2.6 illustrate the individual XPS spectra of the graphite oxide film before (Figures 2.5a and 2.6a) and after (Figures 2.5b and 2.6b) excimer laser irradiation in vacuum (~ 10^{-6} Torr) with 32 pulses at ~ 138 mJ/cm^2. It should be noted that this data is only representative of the surface of the samples as the escape depth of X-ray photoelectrons at these energies is on the order of ~ 10 nm. More specifically, the film's surface was sampled, which includes micron-size domains, but the bulk is not sampled.

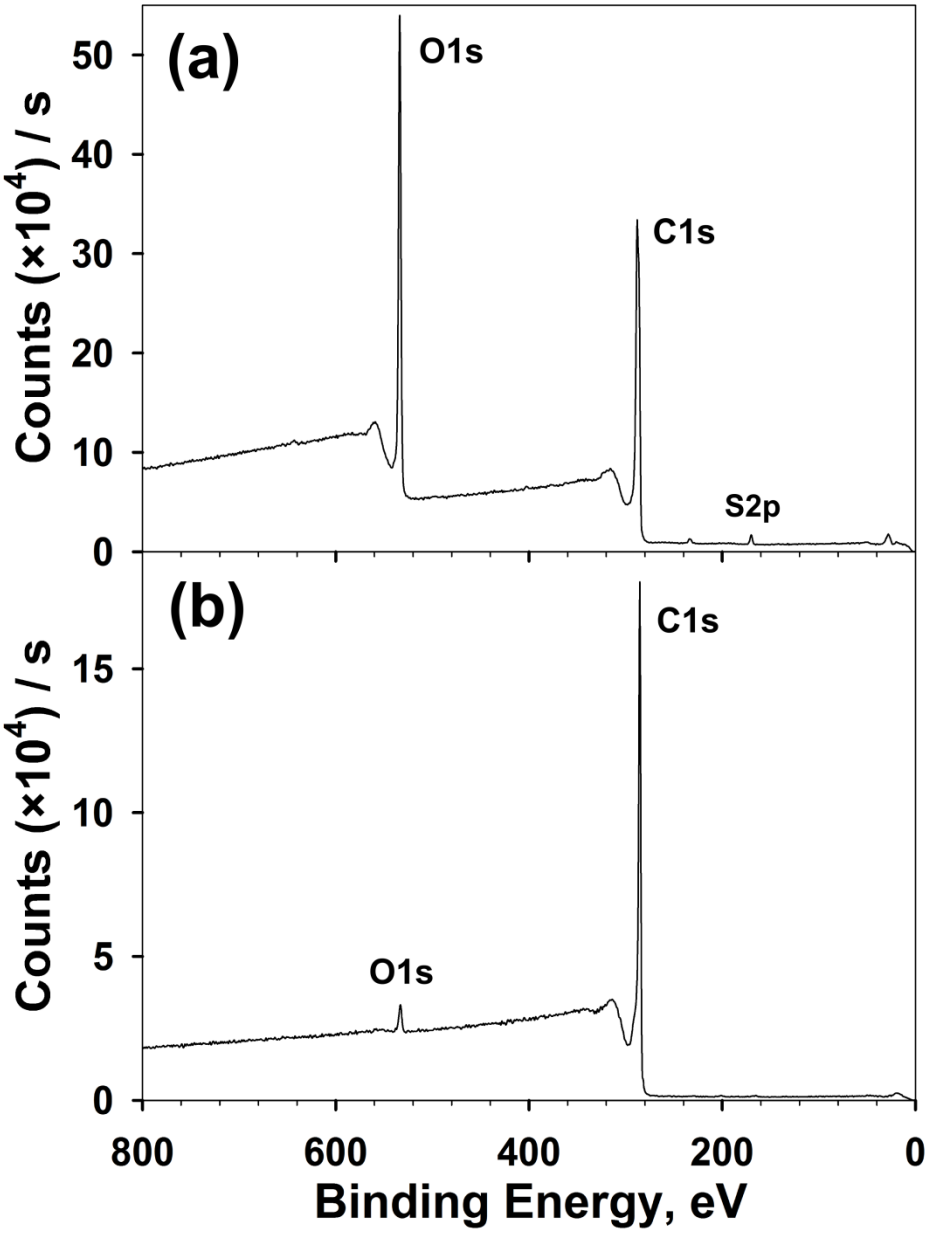

Figure 2.5: XPS spectra of graphite oxide before (a) and after (b) excimer laser irradiation in high vacuum after 32 pulses at ~ 138 mJ/cm^2 laser fluence. Graphite oxide before irradiation has ~ 29% of oxygen and C/O ratio of 2.43. After the excimer laser irradiation, the oxygen content is decreased to ~ 2-3% and the C/O ratio is increased to 40.

The untreated graphite oxide (Figure 2.5a), as expected, has dominant carbon and oxygen features with a trace amount of residual sulfur left over from the synthesis of graphite oxide via the modified Hummers method. The initial oxygen content is ~ 29% and the C/O ratio is ~ 2.43 (based on the ratio of areas under the curve of C1s and O1s peaks). Curve fitting of the C1s peak (Figure 2.6a) reveals the presence of oxygen containing functionalities in the form of epoxy, hydroxyl and carbonyl groups. Once the laser reduction is performed, a drastic change in the amount of oxygen is observed (Figure 2.6b). The oxygen content is decreased to as little as ~ 2-3%, and the C/O ratio reaches ~ 40. Curve fitting of the C1s peak in the laser-reduced sample (Figure 2.6b) confirms a predominance of the sp^2 hybridized carbon, indicating graphene formation; although a contribution from carbonyl peaks is also observed.

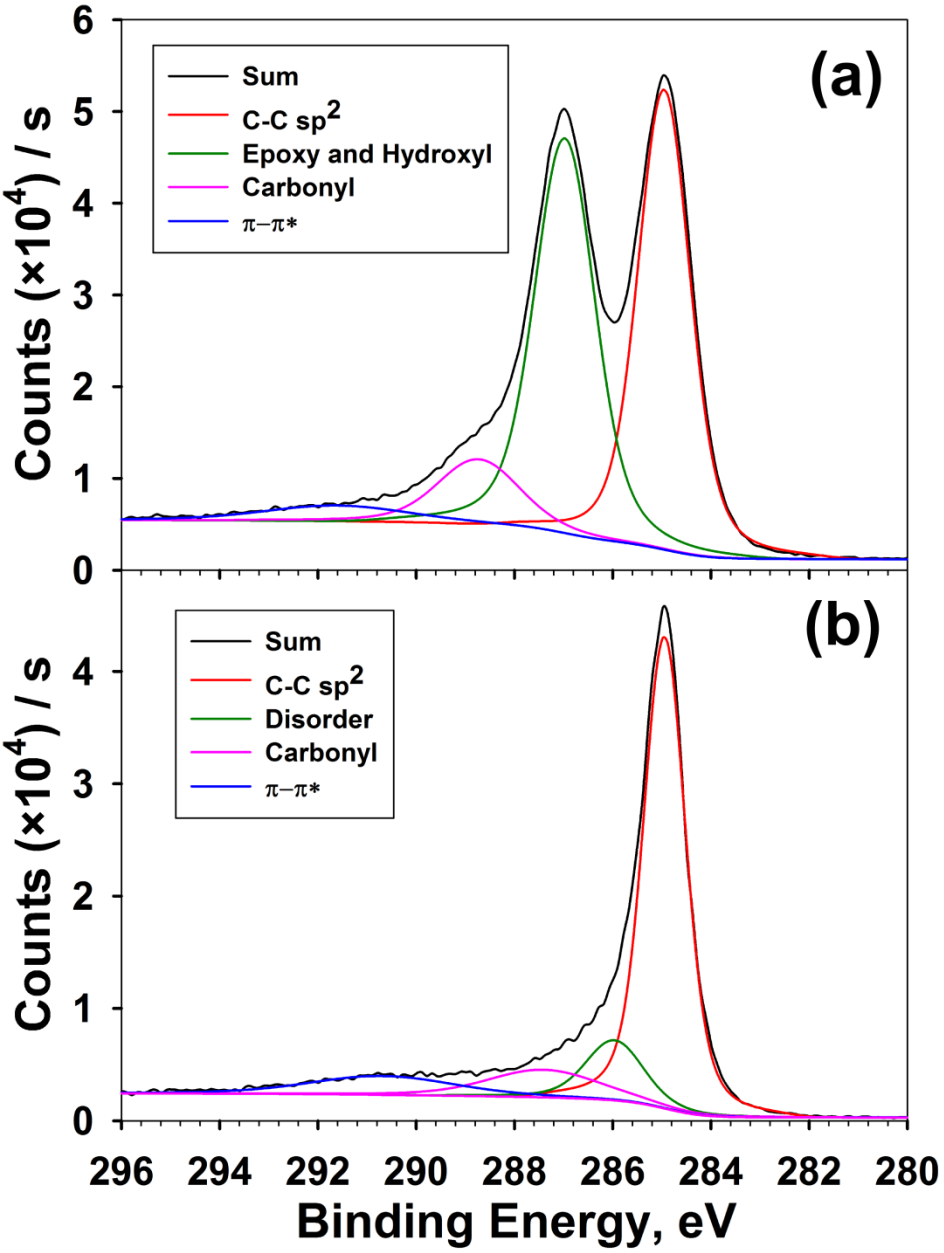

Figure 2.6: XPS C1s peak spectra of graphite oxide before (a) and after (b) excimer laser irradiation in high vacuum with 32 pulses at ~ 138 mJ/cm^2 laser fluence. Before irradiation, the C1s peak analysis of the untreated graphite oxide reveals the presence of oxygen containing functionalities in the form of epoxy, hydroxyl and carbonyl groups. After laser irradiation, the peaks associated with the oxygen containing functionalities are diminished, and the predominance of the sp^2 hybridized carbon peak (red curve, peak position at ~ 284.9 eV) confirms graphene formation.

2.4.3 Laser Reduction Parameters

The CW approach for graphene production utilized the Raman microscope 532 nm diode laser. In this case, the laser (~ 20 mW) was focused on the GO sample using a 20× objective for a 1 second exposure time. Exposure was carried out either in ambient air or in a custom built gas flow cell purged with N_2. Graphene formation using pulsed (~ 9 ns, 20 Hz) irradiation was carried out using the frequency doubled (532 nm) and tripled (355 nm) outputs of a Nd:YAG laser. As with the CW measurements, the GO was suspended between two pieces of carbon tape. The unfocused laser beams irradiated the GO foil for approximately 20 seconds with typical energies of a few mJ/pulse or total power densities in the MW/cm^2 regime.

Figure 2.7 displays integrated D and G' peak intensity ratios ($I_D/I_{G'}$) as a function of laser pulse power for the nanosecond Nd:YAG laser with 355 and 532 nm laser excitations. When using 355 nm photons, the G'-band is produced at the lowest powers and the ($I_D/I_{G'}$) ratio is about 1–1.5. Though sample surface non-uniformity causes variability, this ratio remains close to 1–1.5 even at the highest power. On the contrary, the $I_D/I_{G'}$ ratio is very dependent on the power when using 532 nm photons and discernable 2D-band features are not evident until ~ 5 mJ/pulse. The 355 nm light excites single-photon mediated valence-to-conduction band transitions. This produces electron-hole plasmas in the material at all pulse energies studied. Since at least two 532 nm photons are required to exceed the band-gap, a coherent multiphoton or incoherent multiple photon process is required to create a similar electron-hole plasma. This is consistent with the 532 nm G'-band formation threshold of 2.8 MW/cm^2 which is well below the pre-ablation threshold of graphite [93].

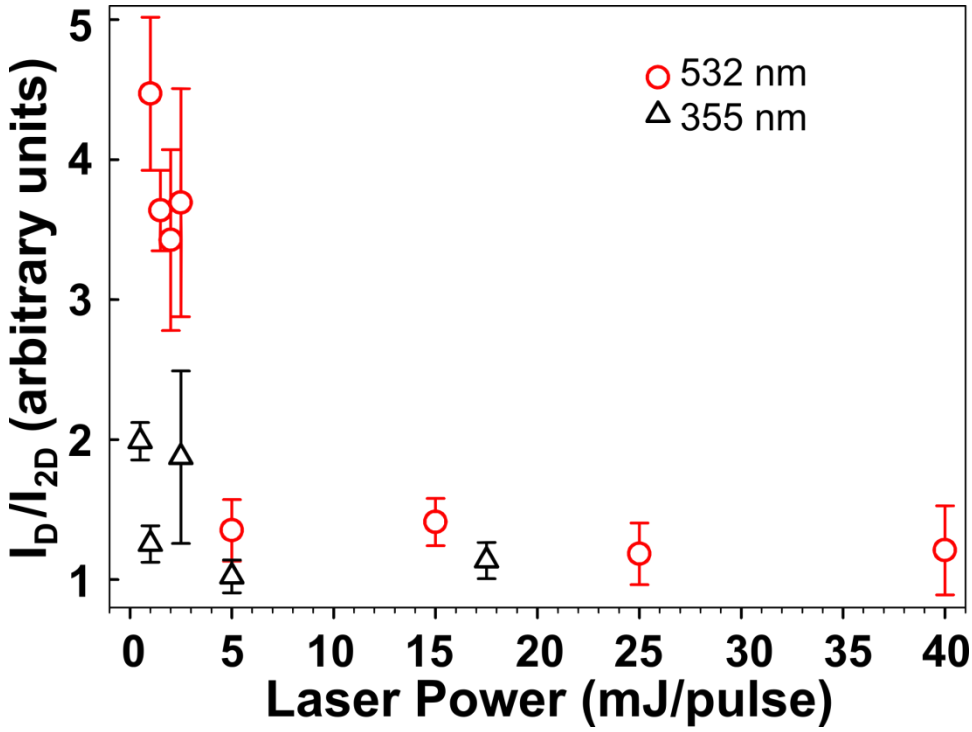

Figure 2.7: The integrated I_D/I_{2D} ratio as a function of 532 and 355 nm laser power.

For the GO reduction utilizing the KrF excimer laser, an array of experiments were performed on a GO sample in which the laser fluence was varied from 60 to 400 mJ/cm^2 along one axis, and the number of laser pulses was varied from 2 to 32 along the other axis. Each of the irradiated areas was then analyzed with Raman spectroscopy and XPS, and the data is presented using three dimensional (3D) plots (Figures 2.8 and 2.9). Figure 2.8 shows reduction performed in high vacuum (~ 10^{-6} Torr) and Figure 2.9 demonstrates reduction performed in a flowing (500 sccm) ultrahigh purity nitrogen. XPS 3D plots (Figures 2.8a and 2.9a) were produced from XPS spectra obtained from a ~ 200 µm area on each of the irradiated spots. The colors in the XPS 3D plots represent different C/O ratios from 2.43 to 40 obtained by taking the ratios of the areas under the C1s and O1s peaks in each spectrum. A higher C/O ratio (red color) means better quality reduction to sp^2 carbon (graphene) features.

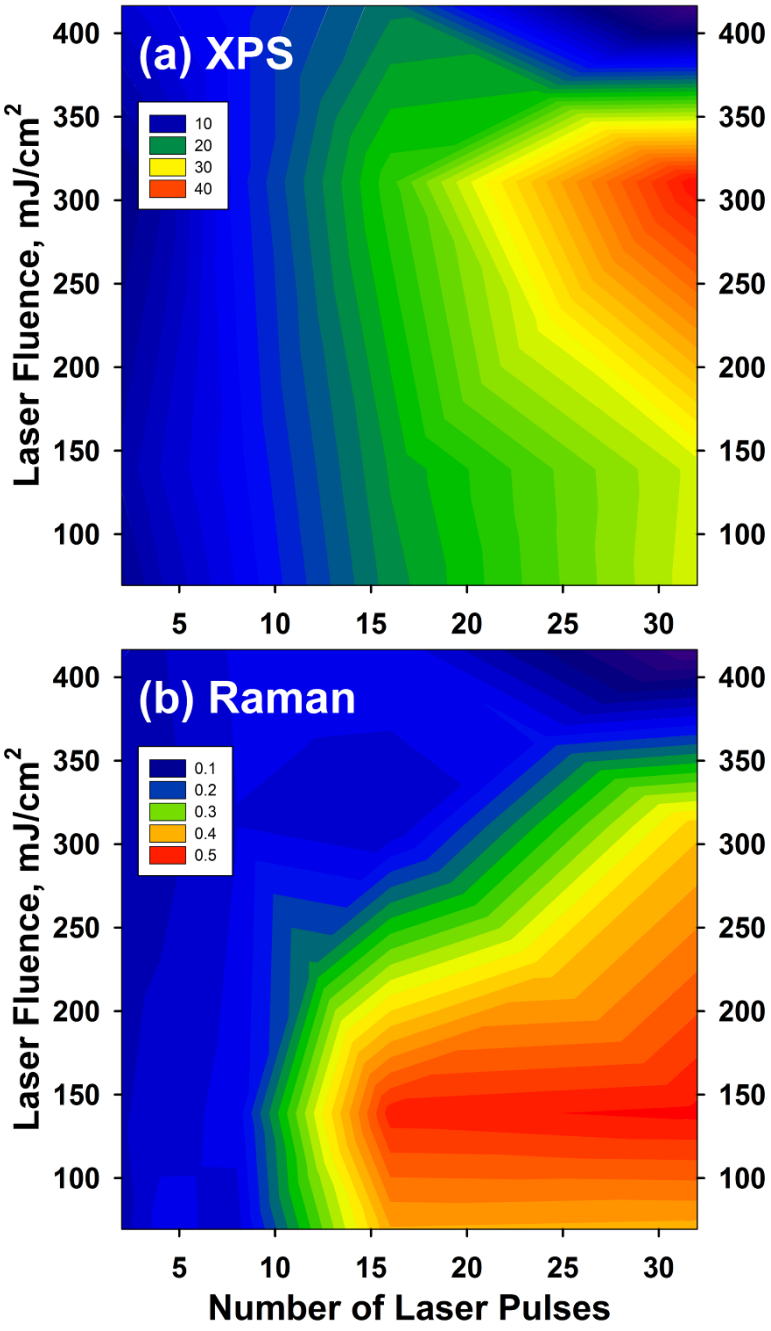

Figure 2.8: 3D plots of the graphite oxide sample after excimer laser reduction in high vacuum as a function of laser fluence and number of laser pulses. (a) Integrated C/O ratios, measured with XPS. (b) G'/G peak intensity ratios, measured with Raman spectroscopy.

Also, Raman 3D plots (Figures 2.8b and 2.9b) were produced by obtaining several Raman spectra from each of the laser reduced areas and then averaging them for each of the laser irradiated spots. The colors represent different G'/G peak intensity ratios from 0.1 to 0.5, with the higher ratio (red color) indicating better quality reduction to graphene. It is important to note that the dark blue regions at high laser fluence and high number of laser pulses in Figures 2.8 and 2.9 are due to the GO films being ablated to the point of not having enough material for analysis. Those regions were assigned a value of zero for both the C/O and G'/G ratios.

By observing all four graphs in Figures 2.8 and 2.9, both Raman and XPS show that the application of ~10-15 pulses is necessary to initiate laser reduction of graphite oxide to multilayer graphene. This is evident by the transition to higher G'/G ratios and higher C/O ratios (from blue to green in all plots). It is also apparent that XPS is less sensitive than micro-Raman spectroscopy with respect to revealing the irradiated areas with the best graphene quality. Interestingly, a high C/O ratio (from XPS analysis) is not the deciding factor when it comes to determine if graphene signatures are exhibited or not. This is very apparent in the high vacuum reduction plots (Figures 2.8a and 2.8b) where according to the XPS (Figure 2.8a), graphene should be formed after ~30 laser pulses and ~ 300 mJ/cm^2. Raman analysis, however, reveals that high quality graphene signatures are already present after 15-20 laser pulses with only ~ 150 mJ/cm^2 (Figure 2.8b).

When comparing XPS and Raman of GO reduction performed in high vacuum (Figure 2.8) with GO reduction performed in nitrogen (Figure 2.9), several clear distinctions emerge. According to Raman analysis, ~ 30 pulses at a fluence of

~ 200-300 mJ/cm^2 are required in nitrogen (Figure 2.9b) to achieve a similar level of graphite oxide reduction when compared with that produced by ~ 15-20 laser pulses at ~ 150 mJ/cm^2 in the high vacuum (Figure 2.8b). The XPS plots of the C/O ratios for both high vacuum (Figure 2.8a) and nitrogen purged samples (Figure 2.9a) reveal that, regardless of the environment, a C/O ratio of ~ 40 is reached after irradiation.

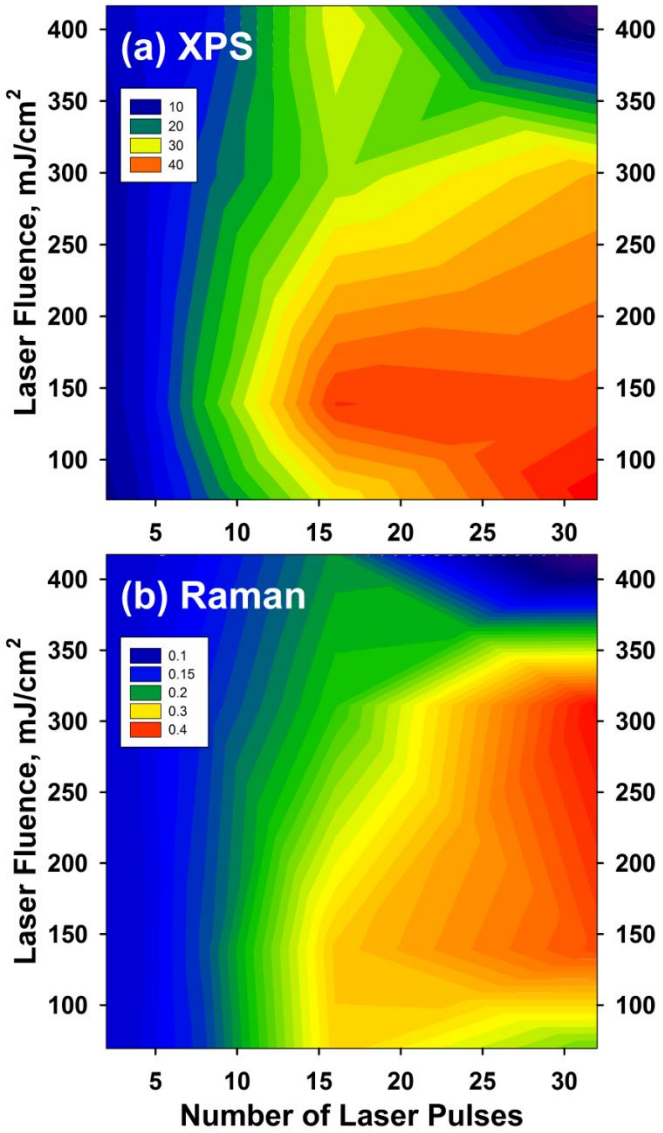

Figure 2.9: 3D plots of the graphite oxide sample after excimer laser reduction in N_2 environment as a function of laser fluence and number of laser pulses. (a) Integrated C/O ratios, measured with XPS. (b) G'/G peak intensity ratios, measured with Raman spectroscopy.

2.4.4 SEM characterization

Scanning electron microscopy (SEM) images were acquired using a Zeiss Ultra60 FE-SEM. The SEM image in Figure 2.10a shows the 10 µm wide × 5 µm deep depression formed by 532 nm CW irradiation of GO. Inspection indicates: i) the depth is self-limiting, ii) the edges outwardly expand, and iii) there is no evidence of melt zones or substantial particle/material build-up near the edges. This feature was mapped with the micro-Raman spectrometer and it was found that the D-band is present mainly at the edges. Conversely, as shown in Figure 2.10b, the G' feature is present mainly in the depression center.

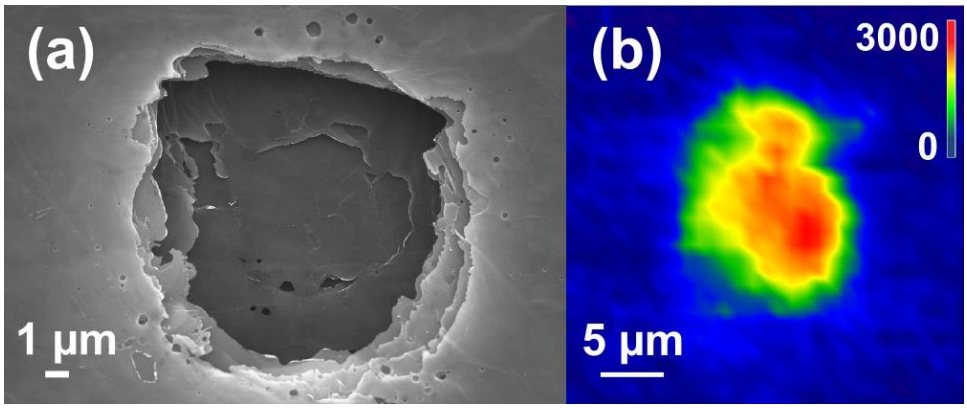

Figure 2.10: (a) SEM image of the 10 µm × 5 µm depression produced by 532 nm CW laser irradiation of graphite oxide. The laser energy was 20 mW. Note the outward expansion of the edges and lack of melt-zones near the edges. (b) Spatially resolved map of the Raman G' band that is characteristic of exfoliated single layer graphene.

Figure 2.11a depicts a SEM image of an unirradiated GO sample, showing that it has a smooth surface morphology. Figures 2.11b-e show several views of the GO film after laser processing. After the laser reduction the film becomes rough with abundant

edges, which have a direct effect on the intensity of the D peak in the Raman spectra. It is clear from the SEM images that the surface area of the laser reduced GO is quite large due to the expanded nature of the graphene layers (Figures 2.11 d,e) with protrusions of reduced graphite oxide as high as ~ 3.2 μm as seen in the cross sectional view in Figure 2.11c. It is interesting to note that the close contact between the laser reduced graphene sheets and the high surface area provide multiple paths for charge transport, and it is likely that the majority of the carriers move through the sheets with little scattering from defects and terminal edges.

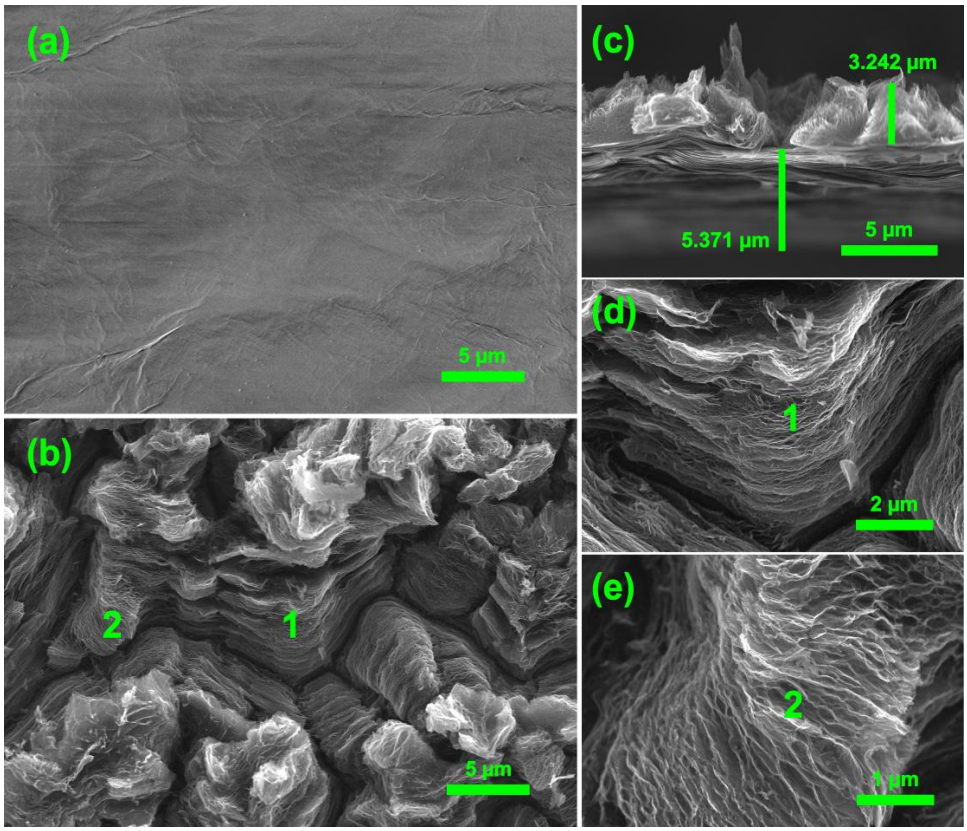

Figure 2.11: Typical SEM images of GO before (a) and after (b-e) excimer laser irradiation in high vacuum with 32 pulses at ~138 mJ/cm^2 laser fluence. (c) The typical cross-sectional view of the excimer laser reduced GO in high vacuum. (d and e) Close-up view of spots 1 and 2 in (b) shows the highly expanded nature of the excimer laser-reduced GO. Note the high surface area and close contact between parts of the reduced GO sheets.

To demonstrate the applicability of the excimer laser reduction approach, a variety of features have been lithographically patterned on GO samples using laser reduction at optimal laser fluence and optimal number of laser pulses (Figure 2.12). The patterning was performed in contact mode using a quartz shadow mask. The smallest patterned features were ~ 1.5-2 μm wide as determined by the mask's pattern dimensions. The inset in Figure 2.12a shows Raman G' peak (~ 2672 cm^{-1}) mapping of an area that includes micropatterned lines. The dark blue color represents the areas of unirradiated graphite oxide, whereas the green-yellow-red areas represent the areas with various graphene qualities (red indicating the highest quality). The non-uniformity in quality can be attributed to the use of contact mode instead of projection mode mask lithography. In contact mode, due to the inherent roughness of the GO film, the shadow mask is in intimate contact with some portions of GO and is slightly elevated from others. Also, the shadow mask prevents the escape of the oxygen rich plasma plume produced during laser irradiation, and since it cannot escape, the ejecta redeposits on the laser irradiated areas (as well as the mask). These factors result in material with non-uniform quality. Projection mode lithography should result in more uniform graphene patterning because there is no mask to trap the plume. It is foreseeable that direct patterning of highly conductive nanofeatures [83-85] will be possible because of the short wavelengths produced by excimer lasers. To evaluate the scalability of this method, institutional logos were patterned as shown in Figure 2.12b.

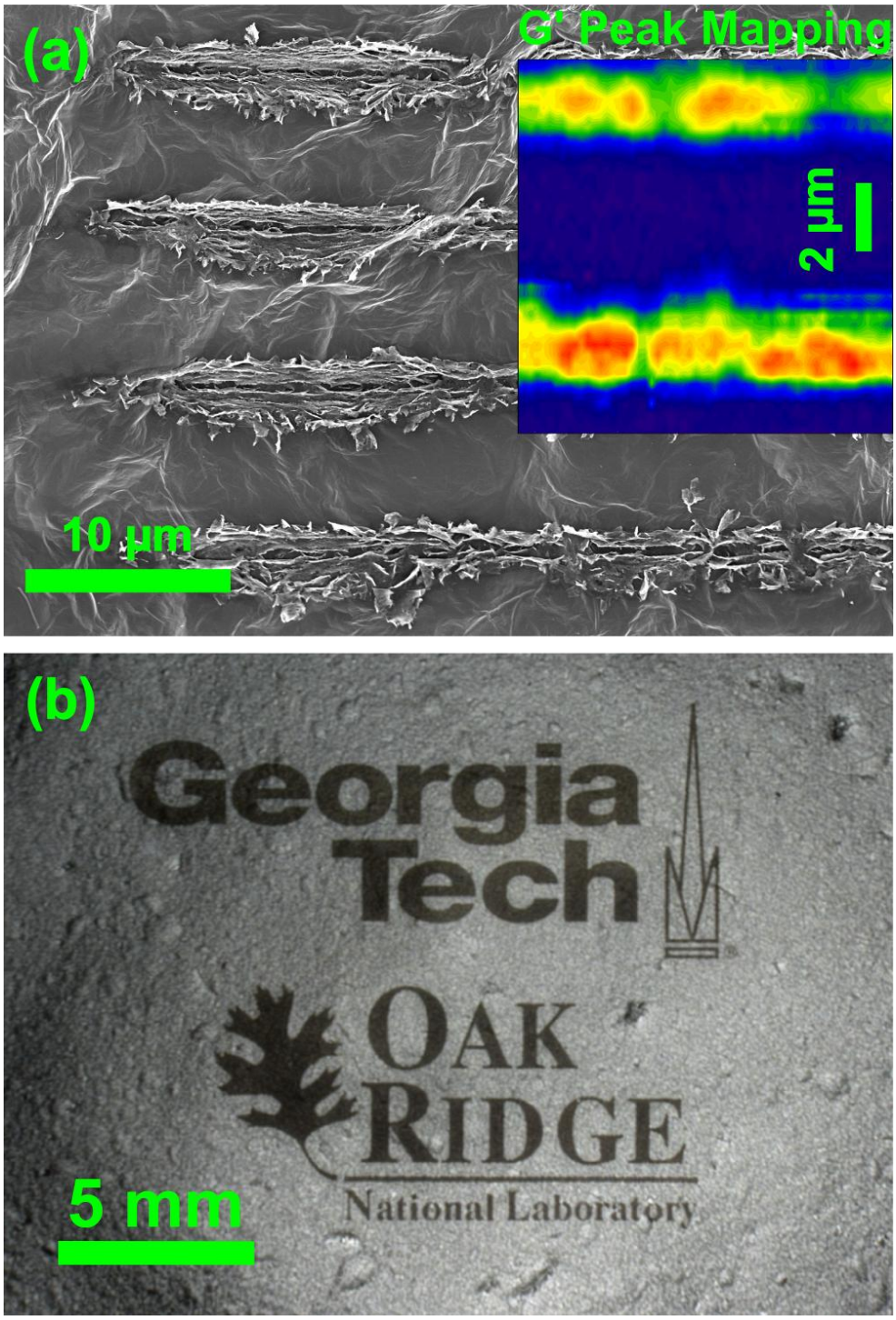

Figure 2.12: (a) Lithographic pattern of microscale parallel lines (~1.5–2 μm wide) produced with a contact mode quartz shadow mask and excimer laser irradiation in high vacuum. The inset is the Raman mapping of the G′ peak at 2672 cm−1 as a function of XY position indicating reduction to graphene in the laser irradiated regions. (b) Logos of Georgia Tech and Oak Ridge National Laboratory, produced via contact mode lithography with excimer laser irradiation of graphite-oxide in high vacuum.

2.4.5 Electrical characterization

Sheet resistance measurements were performed at ambient conditions with a Keithley 2400 source meter instrument, and a conventional 4-point probe station. To gain insight into carrier transport within the excimer laser reduced material, sheet resistance under ambient conditions was evaluated as a function of the number of laser pulses (Figure 2.13).

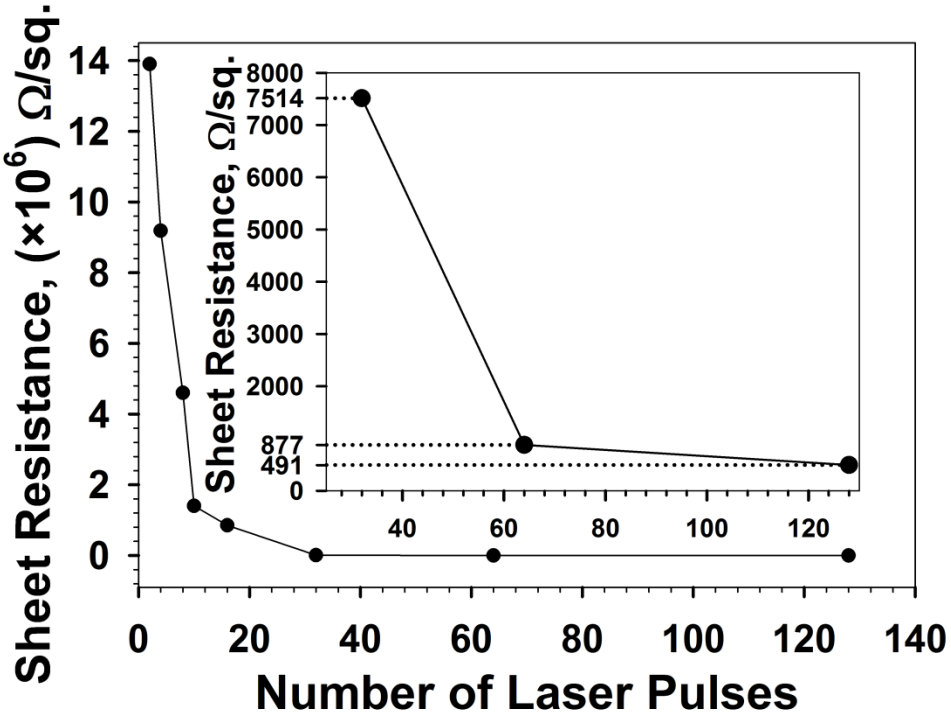

Figure 2.13: Sheet resistance as a function of number of laser pulses, measured from a sample irradiated in rough vacuum (~ 9.8 × 10^{-2} Torr) with 248 nm KrF excimer laser with a fluence of ~ 204 mJ/cm^2. The inset is the magnified view of the last three data points.

To be able to measure sheet resistances on the excimer laser reduced GO these samples required areas irradiated with larger laser beam spot sizes onto which silver paste contacts could be deposited. These KrF-laser irradiation experiments were carried out in low vacuum (~ 9.8 × 10^{-2} Torr) with a fluence of ~ 204 mJ/cm^2. The maximally-reduced

Raman spectra obtained from these samples were comparable to those reduced at high vacuum (G'/G of 0.41 vs. 0.50, respectively). The only notable difference is the larger number of laser pulses required for the reduction process, a result which is consistent and predictable from Figure 2.8b. The Van der Pauw four-point probe method [94] was utilized, and the lowest sheet resistance measured was ~ 491 Ω/sq. For GO samples that were pre-reduced thermally at 150°C for 24 hours to decrease the oxygen content from ~ 29% to ~ 18%, the lowest sheet resistance measured after laser processing was ~ 100 Ω/sq. The sheet resistance of untreated GO was previously reported to be ~ 10^{10} Ω/sq [40], making the present values among the best reported thus far for any laser reduction method. The only other GO reduction approaches that report comparable sheet resistance values are based on the combination of chemical and/or thermal reduction of graphite oxide [48]. It is known that the sheet resistance of GO is related to the C/O ratio [45,47,48,95-97] and overall film quality/defect density. The very low sheet resistance in our reduced GO can be collectively accounted for by the high C/O ratio, high surface area and many overlapping points of contact.

2.4.6 Proposed mechanism of graphite oxide reduction and graphene formation

The physics governing laser desorption of semi-conducting and insulating materials can be dominated by electronic and/or thermal processes. The relative contributions of non-thermal vs. thermal processes are governed by the degree of energy localization. Though electron-lattice temperature equilibration occurs on the picosecond time scale in graphite [98,99], hole-hole localization, exciton self-trapping and

subsequent material ejection can occur. The localization of energy via these pathways can be facilitated by the strain associated with the oxygen in GO [100,101]. It is well known that laser desorption can be initiated by excitation of surface defects and that significant material removal (i.e. ablation) relies upon the production of a critical density of vacancies [102]. These vacancies are mainly created by the localized holes in the top of the valence band and the subsequent hole-hole Coulomb interactions. Depending upon the density of electrons, ions and neutrals emitted, one can create a plasma plume which must expand as it leaves the surface. For our typical background pressures, the expansion is initially free, the plume then expands with shock-wave behavior, and lastly a drag force determines the plume shape evolution and subsequent material re-deposition [103]. Oxidation is minimized using N_2 gas and clustering reactions within the plume form higher mass sp^2 hybridized carbon products. These high mass products can be deposited on the surface and serve as seeds for growth of larger graphene particles and ultimately micro-scale sheets.

Since electron-phonon coupling within a graphite oxide sheet is also strong, rapid local heating causes temperatures to exceed that required for oxidative disruption of the GO lattice [104]. This enhances the production and release of CO and CO_2. Heat dissipation can also occur by heating and vaporizing the interlaminar water creating high internal pressures between the graphene oxide sheets. Efficient material removal would then occur via rapid degassing and quasi-phase explosion of the superheated underlying layers [105].

From XPS and Raman analysis of the pulsed excimer laser reduced GO (Figures 2.8 and 2.9), it is clear that an incubation dose of ~ 10-15 shots at ~ 150 mJ/cm^2

(~ 2×10^{17} photons/cm^2) is necessary before appreciable laser ablation/reduction can take place. We associate this dose dependence with the formation of vacancies and the removal of terminal O atoms. Indeed, this is consistent with the XPS C/O ratio (~ 15-20) shown in Figures 2.8a and 2.9a. This ratio indicates that an oxygen content of ~ 4-7%, and the corresponding number of carbon vacancies, is an optimal value to initiate excimer laser reduction of GO to graphene at 248 nm. The samples reduced in high vacuum, with C/O ratio of as low as ~ 25 (Figure 2.8a, green color), exhibit graphene features in Raman (Figure 2.8b). Though the presence of some residual oxygen functionalities on laser reduced GO is tolerable for preservation of the graphene electronic structure, the best graphene is produced when the reduction is performed in an oxygen-free environment – i.e., vacuum or ultrapure nitrogen. This is evidenced by comparing Raman G'/G peak ratios as a function of environment (see Figures 2.8 and 2.9).

Ejecta formed during laser ablation expand normal to the sample plane in a plume with a shape that is driven by pressure gradients, and therefore is inversely proportional to the beam dimensions. The plume expands initially with a velocity that is determined by the numerous collisions within the very dense collisional Knudsen layer close to the target surface. In vacuum, following the collisions within the Knudsen layer, which result in a fraction of material redeposited on the sample surface, the forward-going component of the plume freely expands. In a background gas, however, this expansion is short-lived - roughly until the pressure within the plume equals that of the surrounding gas. The plume sets in motion a shock wave in the background gas, and a rarefaction wave can lead to further re-deposition of material on the target. Under these conditions,

it is likely that the difference mentioned above regarding graphene quality as a function of environment may be due to redeposition of the ejected oxidized species and possible reoxidation of the laser reduced GO. This plume behavior is similar to the dynamics reported for the laser ablation of graphite in vacuum and inert gases [106]. Although the composition of the plume during excimer laser reduction of GO has not been analyzed during the present experiment, previous reports of the photoreduction approach [107] and during photon irradiation studies of GO [108,109] show that the plume contains oxygen rich sp^3 hybridized carbon fragments as well as species such as H_2O, CO, O_2 and CO_2. Previous work on laser ablation of carbon and graphite also demonstrates the direct removal of nanoscale graphene sheets [110]. Clustering reactions within the plume can also form higher mass sp^2 hybridized carbon products, and under the N_2 purging conditions utilized in our experiments, these carbon-bearing products can be deposited on the surface and serve as seeds for growth of larger graphene particles or sheets. Lastly, though the plume may react with the nitrogen gas, no nitrogen incorporation was observed during the XPS analysis of the present samples.

2.5 Future improvements

There are several enhancements to the method that can be implemented to improve the reduction uniformity of graphite oxide as well as transition this process to the nanoscale.

Irregularities and roughness of the laser reduced GO observed in Figure 2.11 can be attributed to the non-uniform beam profile of the excimer laser, with multiple hot spots (areas of the beam with higher light intensity than other areas). The use of beam

homogenizers can be implemented to produce a laser beam with a uniform light intensity distribution throughout the irradiation zone. These uniformly illuminated areas are sometimes referred to as the top-hat profiles. This can be achieved by passing the laser beam through the random diffusers coupled with microlens arrays. This combination of the optical elements divides incoming laser beam into many microscopic beamlets, which, when imaged onto the sample, produce a uniformly irradiated areas and, thus, a uniformly reduced GO film.

Patterning conductive nanoscale features on an insulating GO is of technological importance. This can be achieved by combining excimer laser sources and the use of appropriate masks with predefined nanoscale features. Contact mode lithography, where the mask is in direct contact with GO, is the easiest approach to accomplish, but might result in a non-uniformly reduced GO due to the inability of the laser generated oxygen-rich plume to escape freely from the surface resulting in its redeposition and reoxidation of the underlying reduced GO substrate. Thus, the use of the projection lithography coupled with the reduction of GO in vacuum or inert gas environments would seem to be a more promising approach for achieving direct nanoscale patterning of the conducting graphitic features on an insulating GO.

2.6 Conclusions

In conclusion, graphene features can be created via irradiation of graphite oxide with low-power, continuous wave or pulsed laser sources. Initial excitation produces an electron-hole plasma within the material and the strain associated with the oxygen-containing groups leads to exciton and hole trapping. This causes material instability, as

well as electron, ion and neutral species ejection. Phonon coupling also leads to efficient heating and material removal. Collectively, these lead to an expanding plasma plume which can nucleate the formation and growth of graphene nanoparticles/sheets in the gas-phase and on the surface. Direct heating of the intrinsic water can also lead to a quasi-phase explosion. Micro-Raman spectroscopy of the CW and the excimer laser microscale irradiated areas reveals the presence of the D-band on edges and unexposed regions, whereas the characteristic graphene G'-band was localized to the areas that were exposed to laser excitation. The G'-band FWHM indicates multilayer graphene, that is most similar to turbostratic graphite. The D and G'-band ratios can be controlled by varying the laser fluence, number of laser pulses and background environments. In the case of 532 nm CW irradiation in N_2 the $I_D/I_{G'}$ ratio is ~0.17.

Excimer laser-induced reduction of graphite oxide using 248 nm photons has been also demonstrated. The quality of the produced graphene was verified with both Raman and XPS spectroscopies as well as sheet resistance measurements. Specifically, Raman analysis of the excimer laser-reduced samples reveals the formation of a prominent G' peak at ~ 2672 cm^{-1} and a high G'/G ratio of ~ 0.5. The XPS analysis reveals the C/O ratio to be as high as ~ 40. The sheet resistance was measured to be ~ 100-500 Ω/sq and these values are among the best reported in the literature for any laser reduction method thus far. The key to complete laser reduction of graphite oxide is pre-treatment with ~ 10-15 pulses at a fluence ~ 100-300 mJ/cm^2 (i.e. a photon flux of up to 2-4 × 10^{17} photons/cm^2) followed by an additional ~ 10-20 shots. The additional laser shots lead to material removal and laser plume production. This laser-based reduction strategy requires the use of an oxygen free environment. The quality of graphene

produced in high vacuum is slightly better than that produced in a N_2 background gas. The use of Raman spectroscopy in conjunction with XPS is essential to verify graphene formation. Scalability of the excimer laser reduction approach was confirmed by patterning institutional logos and microscale features (~ 1.5-2 μm wide parallel lines). Future work will involve further improvements of the pattering process by evaluating the effects of other background gas mixtures on the laser-produced plume composition and dynamics.

CHAPTER III

LIGHT SENSORS BASED ON LASER REDUCED GRAPHITE OXIDE

3.1 Introduction

Due to the limitations in the light conversion efficiency and high manufacturing costs of silicon based photovoltaic devices researchers throughout the world have been investigating the use of organic photovoltaic materials as cheaper and more efficient alternatives. Organic photovoltaic materials based on hybrid architecture are especially appealing, due to potentially higher light conversion efficiencies. Hybrid architectures utilize dissimilar materials or differently doped materials to achieve charge carrier separation. Unfortunately, rapid recombination of charge carriers at the donor-acceptor interface has been a problem for the devices based on the hybrid architectures, resulting in the lowering of their overall efficiencies. In this chapter, laser reduced graphite oxide (rGO) materials with unique surface morphologies and tunable bandgaps are used for photovoltaic applications. The advantage of the laser reduced graphite oxide surfaces is in an elimination of interface losses since hybrid architectures are no longer needed. Excimer laser graphite oxide (GO) reduction is a key step in the fabrication of light sensitive graphene based materials. Uneven oxygen doping distribution and unique surface morphology of the new materials allows conversion of light energy into electric current. This is achieved without the introduction of any additional hybrid materials into the system. Devices produced with this approach are capable of generating photovoltage and photocurrent from the broadband light sources with zero source-drain bias applied.

Since first deposition of single layer graphene on a dielectric substrate [5], graphene has attracted great scientific interest due to its unique physical and electric properties. For the past several years researchers have been working on developing new routes for graphene production; however, there is still a need to produce graphene in large quantities and at low cost. The reduction of graphene oxide can be one of the alternative routes to achieving large quantities of carbon based materials with graphitic properties. Additionally, carbon nanotubes (CNTs), monolayer graphene (G) and reduced graphene oxides (rGO) show great potential for solar cell applications with higher light conversion efficiencies compared to the conventional silicon based solar cell devices. Specifically, hybrid carbon nanomaterials show great promise for the fabrication of solar cells and light sensing devices. Incorporation of nanoparticles on the surface of carbon based materials has been considered as a general strategy towards hybrid carbon based systems. Recently, several reports demonstrated the synthesis and incorporation methods of metallic and semiconducting nanoparticles on a variety of carbon surfaces.

In this work, a simple and reproducible method for the fabrication of large-scale freestanding laser reduced graphite oxide films and their use for the self-powered broadband light sensing applications is demonstrated. Photocurrent and photovoltage generation is evaluated as a function of oxygen content of the underlying graphite oxide substrate. Additionally, no hybrid material incorporation on laser rGO surface is needed to construct a photosensitive device.

3.2 Experimental details

3.2.1 Sample preparation

Graphite oxide (GO) solution is prepared using the modified Hummers method [37,38] by oxidizing graphite powder (325 mesh) for 7 days followed by purification through dilution with nanopure water and centrifugation cycles rather than filtration. The purification procedure is repeated until the solution reached pH 7. Freestanding graphite oxide films are produced by filtering the concentrated graphite oxide solution with a high pressure (170 psi head pressure) filtration funnel (Pall Corporation) through the 47 mm diameter Whatman nylon filter membrane with 200 nm pores. The filtered graphite oxide on the nylon membrane is dried for 24hrs at 150°C in an oven to produce freestanding graphite oxide films with 18.1% oxygen content (4.47 C/O ratio). To produce graphite oxide films with 34.1% (1.90 C/O ratio), the freshly filtered graphite oxide paper is dried in a desiccator (Drierite drying agent) at room temperature for 72hrs. For convenience these samples will be named GO18 and GO34 respectively. The oxygen content has been determined with the X-ray photoelectron spectroscopic (XPS) analysis.

The GO laser reduction has been performed with a Lambda Physik LPX-300 KrF excimer laser with an excitation wavelength of 248 nm. Excimer laser reduced graphite oxide films have been produced by irradiating GO18 with 32 laser pulses under ultrahigh purity N_2 purging and GO34 with 64 laser pulses under $\sim 1 \times 10^{-2}$ Torr vacuum. Laser fluence has been set to ~ 140 mJ/cm^2 and the repetition rate to 1Hz for both samples. Additional information about the laser reduction of GO can be found in chapter 2 of this Thesis.

3.2.2 Experimental setup

A schematic diagram of the experimental setup is presented in Figure 3.1. For the light sensing experiments, laser reduced GO samples have been mounted on an insulating alumina ceramic substrate. Four thin wires served as electrical probes and were attached to the sample via conductive silver paste. The alumina substrate is then attached to the 50W cartridge heater, capable of heating the sample up to several hundred degrees centigrade. The entire assembly is placed in a vacuum chamber and evacuated to a base pressure ~ 5×10^{-9} Torr. For the light sensing experiments, GO samples are exposed to the light illumination, produced by the CW laser diodes, through a quartz vacuum viewport. Peak excitation wavelengths of 405, 532, 635 and 808 nm have been used, in order to investigate sensor responses to the range of the visible light spectrum. Laser diode light, initially unfocused and with a power of 100-150 mW, is passed through a series of collimating lenses, intensity attenuator and the final focusing lens before irradiating the sample. The power of the collimated laser light is attenuated to ~ 20 mW and the irradiated spotsize on the sample is ~ 1 mm. A mechanically controlled shutter is placed in front of the quartz viewport in order to evaluate the sensor on-off responses. It is important to note that the laser diode has to be warmed up for several minutes prior to performing experiments and an adequate cooling has to be provided for it as well to minimize laser power fluctuations. The photo-generated current and voltage are measured with a Keithey 6485 picoammeter and a Keithley 2182A nanovoltmeter, respectively. Sheet resistance measurements are performed with a Keithley 2400 source meter. Sample temperature is monitored with an Omega Dpi16 temperature monitor. All of the instruments have been computer interfaced and controlled with LabView software.

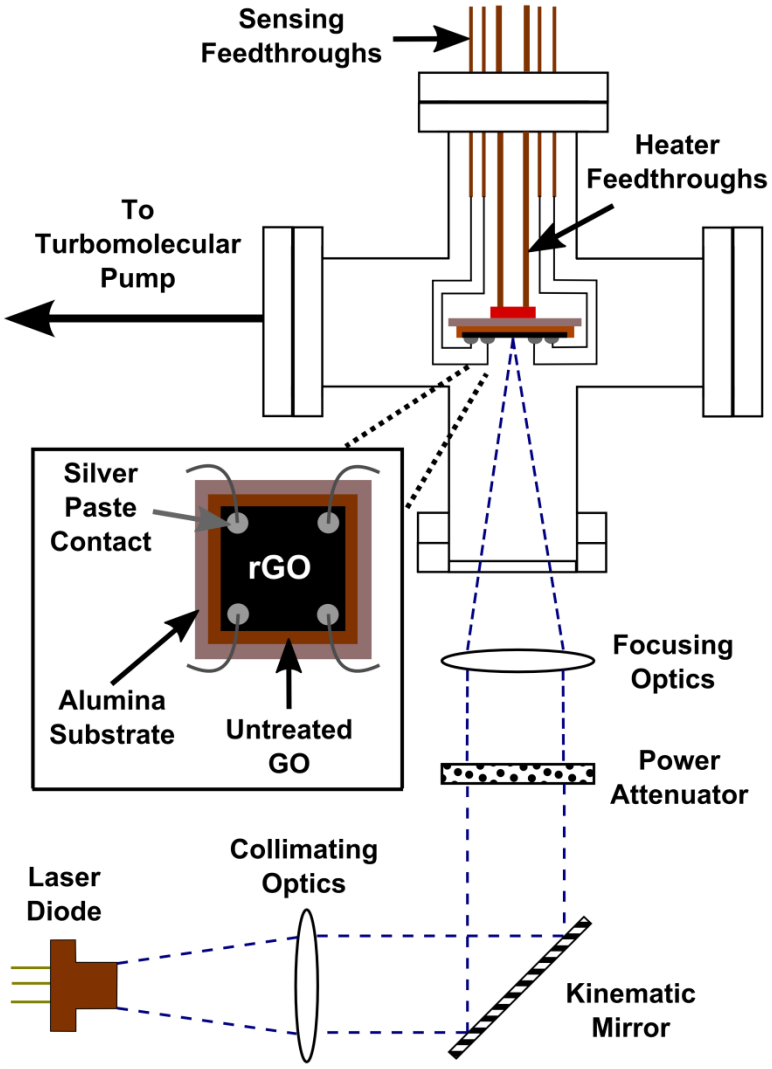

Figure 3.1: Schematic diagram of the photosensing experimental setup.

3.3 Results

3.3.1 Raman characterization: low and high oxygen content graphite oxide

Two distinctly different samples are produced via laser irradiation of low and high oxygen content graphite oxide films. The Raman spectra of the untreated low (GO18) and high (GO34) oxygen content graphite oxide are shown in Figure 3.2. Spectra of both samples exhibit peaks corresponding to defects at ~ 1351 cm^{-1} and ~ 1354 cm^{-1} for GO18 and GO34 respectively. The intensity of the defect band (D-band) for the low oxygen content GO is slightly higher compared to high oxygen content GO, indicating that the partial thermal reduction procedure used to produce GO18 sample introduces additional defects into the structure of GO. The peaks due to the in-plane vibrations of sp^2 bonded carbon atoms (G-band) are present at ~ 1590cm^{-1} and at ~ 1601 cm^{-1} for GO18 and GO34 samples respectively. The weak and broad shape of the G' centered around 2665cm^{-1} is sensitive to the chemical doping [111] such as presence of oxygen and also indicates the existence of disorder [112]. It is observed that G', D+G and 2G bands are more pronounced in the GO34 sample, compared to GO18.

Raman spectra of the laser reduced high oxygen content (rGO34) and low oxygen content (rGO18) graphite oxide samples are shown in Figure 3.3. Peak positions of the D band (~ 1348 cm^{-1}) and G band (~ 1580 cm^{-1}) are identical for both rGO18 and rGO34. The G' peak position for rGO18 is at ~ 2684 cm^{-1} and at ~ 2682 cm^{-1} for rGO34. The appearance of the prominent G' bands in both samples suggests that the existence of disorder in the laser reduced GO is dramatically reduced [112]. These similarities in peak positions indicate production of laser reduced graphitic material with comparable qualities. It is noticeable though, that the D band for rGO18 is smaller in intensity

compared to the D band of rGO34, indicating fewer defects in rGO18. This can also mean that rGO34 has more edge scattering, which is substantiated by the SEM images in Figure 3.6. Also, the underlying unreduced GO can contribute to the D band formation, with the contribution from unreduced GO34 being more pronounced compared to GO18.

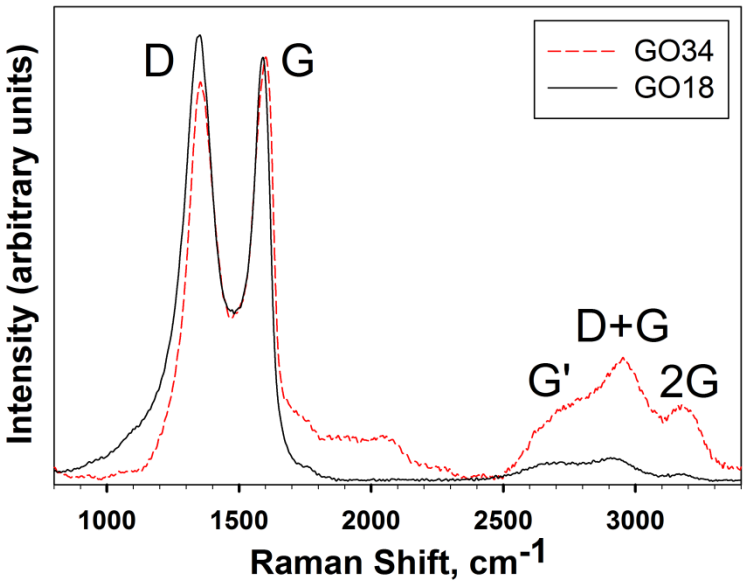

Figure 3.2: Raman spectra of the untreated high oxygen content GO (GO34) and low oxygen content GO (GO18) (the spectra were normalized to the G peak).

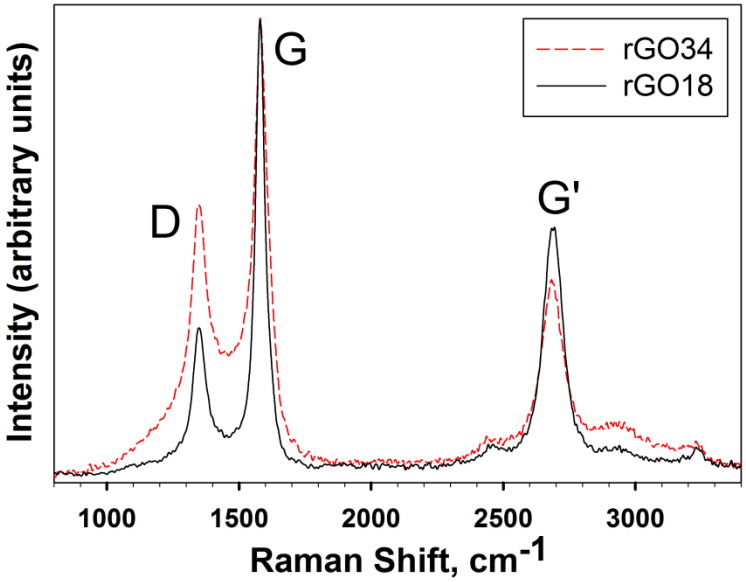

Figure 3.3: Raman spectra of the laser reduced high oxygen content GO (rGO34) and laser reduced low oxygen content GO (rGO18) (the spectra were normalized to the G peak).

3.3.2 XPS characterization: low and high oxygen content graphite oxide

XPS analysis (Figures 3.4 and 3.5) is used for further confirmation of graphite oxide reduction and for evaluation of functional group presence. Figure 3.4 shows spectra for the untreated GO18 (Figure 3.4 a,c) and laser reduced rGO18 samples (Figures 3.4 b,d), whereas Figure 3.5 shows spectra for the untreated GO34 (Figure 3.5 a,c) and laser reduced rGO34 film (Figure 3.5 b,d).

A significant amount of oxygen is observed in both untreated GO18 (~ 18.1%) and GO34 (~ 34.1%) materials. The initial carbon to oxygen (C/O) ratio is ~ 4.47 for GO18 and ~ 1.90 for GO34 respectively. The spectrum of the excimer laser reduced rGO18 (Figure 3.4b) confirms that the amount of oxygen is decreased to ~ 4.71%, and the C/O ratio is increased to ~ 20.04. Figure 3.5b confirms the decrease in oxygen content for GO34 to ~ 14.5% and the C/O ratio increase to ~ 5.5.

The high resolution analysis of the C1s peak for the GO18 before the reduction (Figure 3.4c) reveals the presence of peaks associated with sp^2 (~ 284.6 eV) and sp^3 (~ 285.9 eV) hybridized carbon. The peak attributed to the oxygen containing functionalities in the form of carboxyl groups is present at ~ 288.3 eV. The π-π^* shakeup peak is present at ~ 291.5 eV. The laser reduced rGO18 spectrum (Figure 3.4d) has a dominant sp^2 peak (~ 284.7 eV) as well as minor peaks associated with sp^3 hybridized carbon (~ 285.2 eV), carbonyl groups (~ 287.3 eV) and π-π^* shakeup (~ 291.2 eV). The C1s peak analysis of the untreated GO34 sample (Figure 3.5c) demonstrates the presence of peaks corresponding to sp^2 (~ 285.1 eV) and sp^3 (~ 285.8 eV) hybridized carbon as well as the carbonyl (~ 287.6 eV) and carboxyl (~ 289.1 eV) groups. Because the sp^2 carbon network is highly disrupted, the π-π^* shakeup peak is not observed. The laser

reduced rGO34 sample (Figure 3.5d) mostly has the peaks attributed to sp^2 (~ 284.8 eV) and sp^3 (~ 285.7 eV) hybridized carbon as well as carboxyl groups (~ 288.6 eV) and π-π* shakeup peak at ~ 292.3 eV.

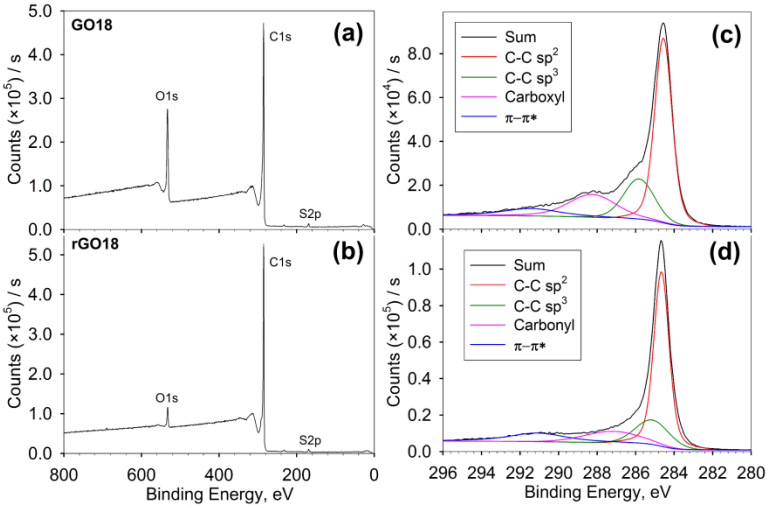

Figure 3.4: (a) XPS survey analysis of the untreated low oxygen graphite oxide GO18 and (b) the excimer laser reduced low oxygen graphite oxide rGO18. (c) High resolution spectra of the C1s peak of the untreated GO18 and (d) the excimer laser reduced graphite oxide rGO18.

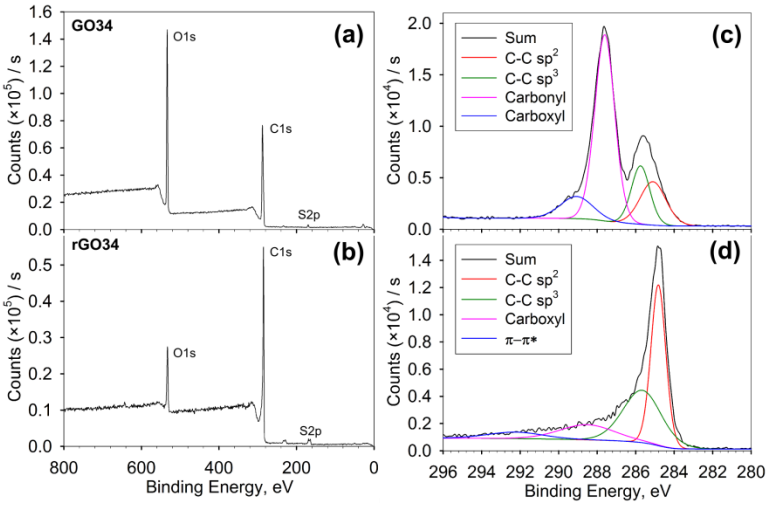

Figure 3.5: (a) XPS survey analysis of the untreated high oxygen content graphite oxide GO34 and (b) the excimer laser reduced high oxygen content graphite oxide rGO18. (c) High resolution spectra of the C1s peak of the untreated GO34 and (d) the excimer laser reduced graphite oxide rGO34.

3.3.3 SEM characterization: low and high oxygen content graphite oxide

Scanning electron microscopy (SEM) is used to evaluate the surface morphology of laser reduced low (rGO18) and high (rGO34) oxygen content GO. Figures 3.6a and 3.6b show SEM images of rGO18 and Figures 3.6c and 3.6d illustrates the SEM images of rGO34. The bottom row of figures is a magnified view of the figures on the top row. By comparing these images it is clear that rGO34 has much rougher surface with flakes of reduced graphene oxide being more expanded, compared to rGO18. The surface of both samples is divided into eroded valleys and more intact expanded segments or hills. This surface morphology can play a significant role in the way charge carriers are created and the ways they migrate on the surface of laser reduced GO. Conductive atomic force microscopy (cAFM) has been also performed (not shown here) and it is determined that the eroded valleys are less conductive then the more intact segments.

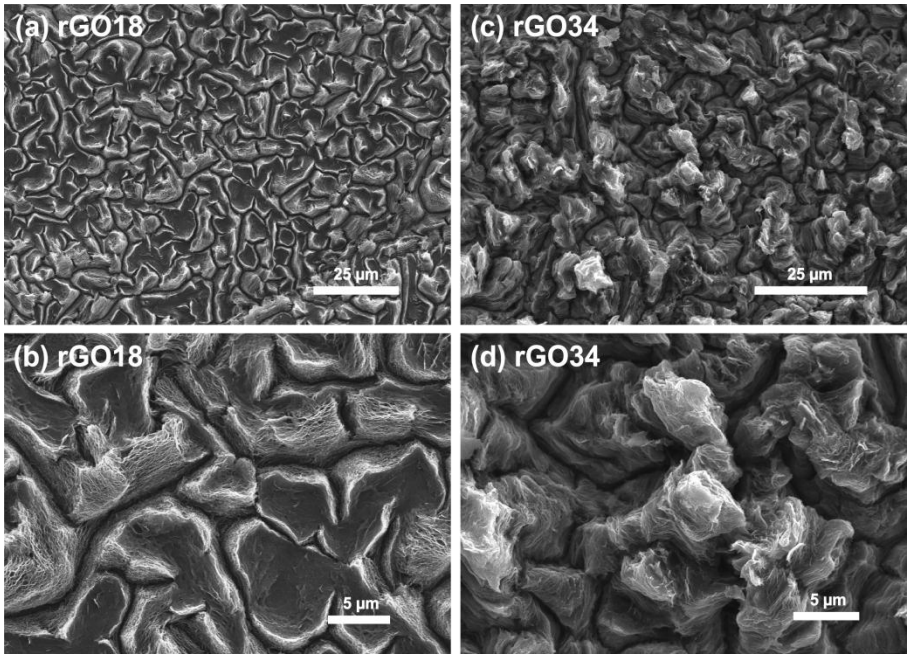

Figure 3.6: (a) Scanning electron microscopy (SEM) image of laser reduced low oxygen content graphite oxide (rGO18). (b) Magnified view of rGO18 in (a). (c) SEM image of laser reduced high oxygen content graphite oxide (rGO34). (d) Magnified view of rGO34 in (c).

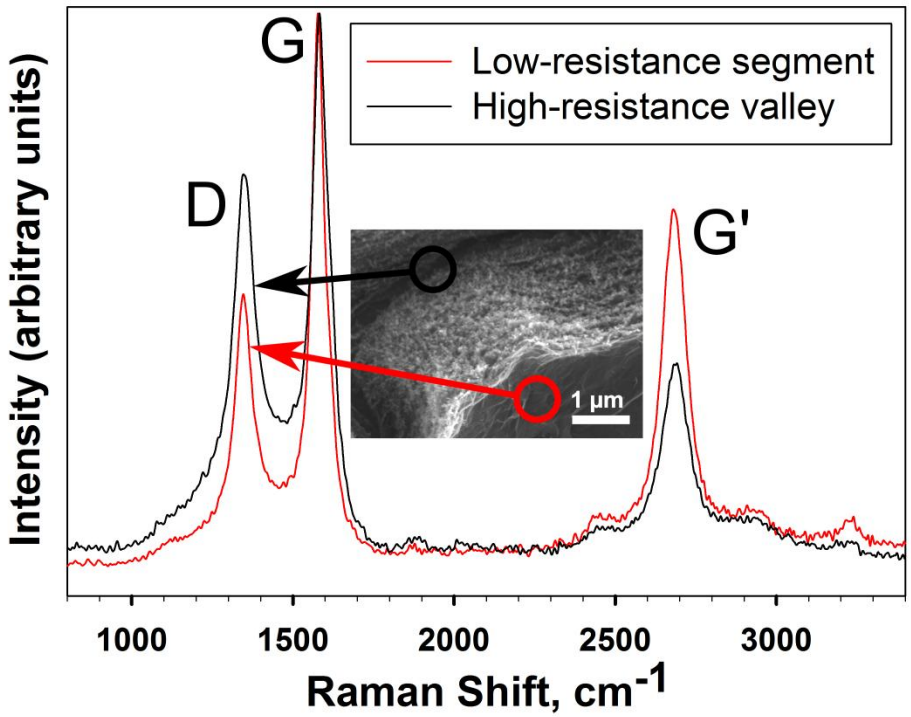

Figure 3.7: Raman spectra of low-resistance segment (red) and high-resistance valley (black) on the excimer laser reduced low oxygen content graphite oxide (rGO18). Raman analysis spots, depicted by the circles, are not scaled with respect to the SEM image.

The higher defect density of the valleys, contributing to their higher resistance, is also confirmed with Raman spectroscopic analysis of rGO18 shown in Figure 3.7 (black curve). Red curve in Figure 3.7 is obtained from a segment that exhibits lower defect density and has more pronounced graphitic properties, indicated by the higher intensity of the G' peak. Defects are also less prevalent in these regions, evident by lower intensity of the D band. The uneven distribution of defects as well as variations in the extent of reduction of the valleys and segments results in a material that is riddled with bandgap inhomogeneities and p-n junctions. These factors are major contributors for the charge carrier generation and separation upon exposure of the laser reduced GO to light. In the next subsection 3.3.4 light sensing properties of the laser reduced graphite oxide materials (rGO18 and rGO34) will be explored in more detail.

3.3.4 Light sensing

Laser reduced graphite oxide samples rGO18 and rGO34 are individually evaluated for their light sensing characteristics, specifically their ability to generate photocurrent and photovoltage upon exposure to light without any additional source-drain bias being applied to the system. Photo-sensing experiments are performed with 405, 635, 532 and 808 nm light source wavelengths.

The dynamic photoresponse curves of the rGO18 and rGO34 sample are shown in Figure 3.8 and 3.9 respectively. Each curve is shown for three cycles of the laser being turned on and off to demonstrate the reproducibility of the data. Each ON and OFF cycle is ~ 210s long. Calibration of photoresponse of the rGO18 device is based on the photocurrent signal for each light source wavelength in order to observe the difference in photovoltage (V_{ph}) generation with no external source-drain voltage (V_{sd}) applied across the device. The laser diodes used for the experiments ranged in their output power between 100 mW to 150 mW. In order to generate the same photocurrent response for the different laser diodes, the collimated laser beam is passed through the light intensity attenuating filter and is then focused on the device surface. The final spot size is ~ 1 mm in diameter and the power is ~ 20 mW. Figure 3.8b demonstrates that the the lowest V_{ph} is generated with 405 nm wavelength, whereas the highest V_{ph} is observed for 808 nm and 635 nm light sources. The photoresponsivity of the device, defined by the ratio of generated photocurrent to dark current I_{sd}(light)/I_{sd}(dark), is determined to be ~ 223, which is a significant improvement compared to results in recent reports [113,114]. The light generated photocurrent of the rGO18 sample is due to the unique morphology of the reduced graphite oxide surfaces after excimer laser reduction. SEM Figures 3.6a and 3.6b

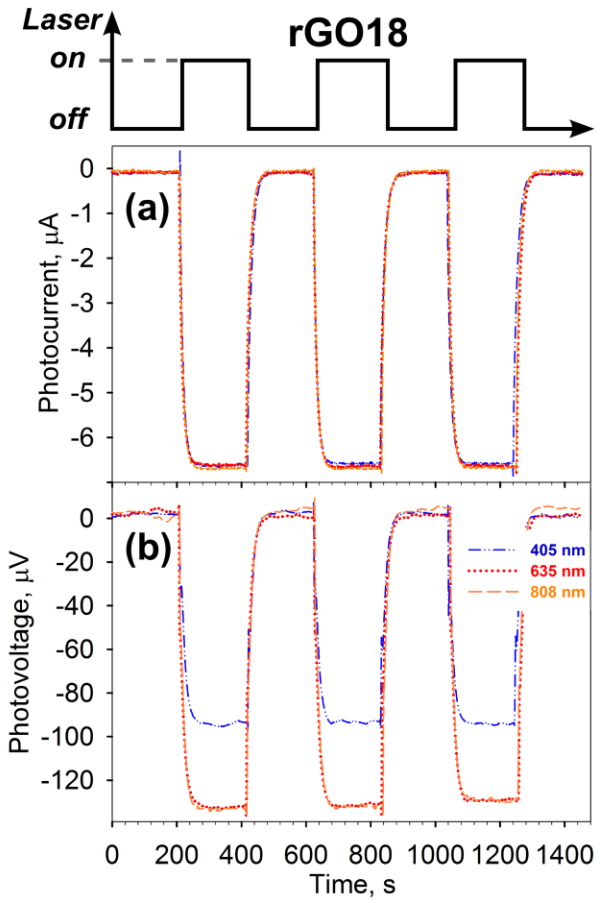

Figure 3.8: Time resolved (a) photocurrent and (b) photovoltage generation with illumination switching between "on" and "off" for the rGO18 photodetector.

in conjunction with the cAFM data (not shown) show that the rGO18 surface consists of extensive low-resistance (more photosensitive) segments with an average area of ~ 10-20 μm^2 separated by high-resistance (less photosensitive) valleys between them with width of ~ 0.2 μm. Photon generated electron-hole pairs in GO18/rGO18 normally would recombine on a time scale of tens of picoseconds, depending on the quality of the rGO18 film [115,116]. The asymmetric shape of the segments and valleys forms uneven internal electric fields (E-fields) which are responsible for the separation of the photo-generated carriers. Under such conditions, the current passing through the sample at low fields is controlled by high resistance segments. As the photo-generated voltage rises, the

injection of the space charge begins to determine the current in the high-resistance segments. At the appropriate level of injection, the resistance of these segments becomes commensurate with that of the low-resistance segments and the asymmetrical nature of the internal E-fields throughout the device surface generates photocurrent across the whole sample.

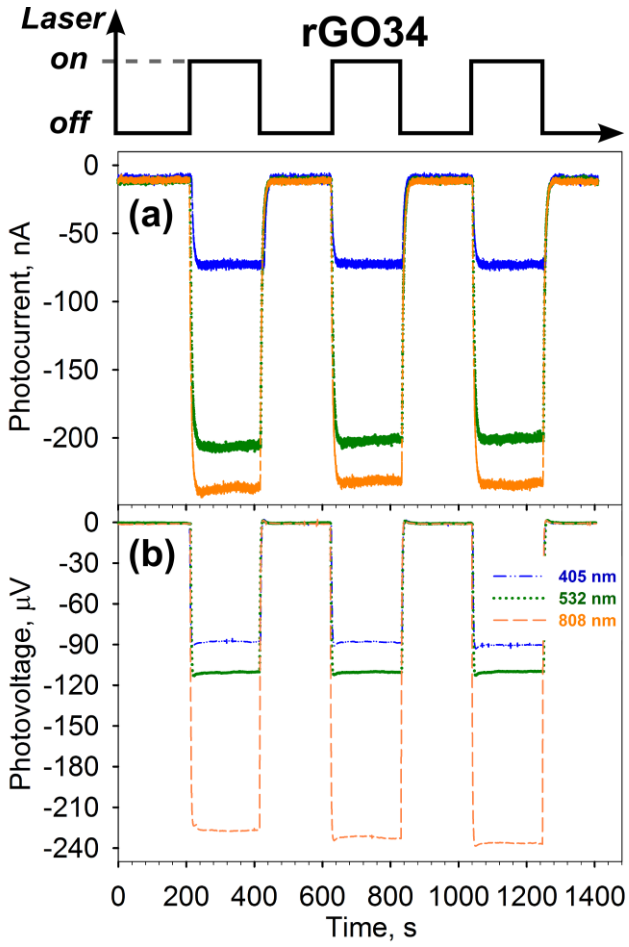

Figure 3.9: Time resolved (a) photocurrent and (b) photovoltage generation with illumination switching between "on" and "off" for the rGO34 photodetector

As previously mentioned, surface morphology of excimer laser reduced GO plays an important role in photovoltage generation. It is also observed that the oxygen content of the underlying GO substrate has a dramatic impact on photovoltage and photocurrent

generation as well. Figure 3.9 shows the levels of photoresponse in rGO34 sample under 405, 532 and 808 nm wavelength illuminations. Figure 3.9a demonstrates that upon illumination of rGO34 the same level of photocurrent as in rGO18 samples is not attainable, but Figure 3.9b demonstrates that the photovoltage generated with 808 nm light is 1.6 times higher and V_{ph} under 405nm illumination is comparable to the levels generated in rGO18 under the same illumination conditions. Overall, when comparing rGO18 and rGO34 and their ability to generate photocurrent, it is clear that rGO18 has a much higher efficiency in converting light into electrical current.

3.4 Conclusions

In summary, in this chapter it is demostrated that large scale laser reduced graphite oxide can be used for converting light energy into electric power. This occurs over a very broad spectral range. An added advantage of this approach is that no additional hybrid material incorporation is necessary for achieving photoresponse. Excimer laser reduction of graphite oxide is a key process step in fabrication of the light sensitive material. The role of the underlying GO substrate has been investigated and it is established that the oxygen content of the untreated GO can play a significant role in determining the photoresponsivity of the laser reduced GO device. Specifically, light sensors based on the graphite oxide with low oxygen content (rGO18) are more efficient in generating photocurrent then the devices based on the high oxygen content (rGO34) graphite oxide. Additionally, due to the laser reduced graphite oxide's unique combination of the surface morphology and chemical properties, it is feasible to explore its use for other promising applications in catalysis, sensors, and optoelectronic devices.

CHAPTER IV

ION BEAM GRAPHITE OXIDE REDUCTION: NANOCONE AND NANOPORE FORMATION

4.1 Introduction

As mentioned in previous chapters, graphite oxide (GO) is considered to be a promising candidate for the production of graphene. In this chapter a novel method is presented for the reduction of GO, based on 3 keV argon ion beam irradiation. The produced material has a carbon to oxygen (C/O) ratio of as high as ~ 215 as verified with the x-ray photoelectron spectroscopic analysis, compared to C/O ratio of ~ 2.37 in the non-irradiated GO. The C1s peak analysis of the irradiated material reveals the predominance of sp^2 hybridized carbon bonds. Raman spectroscopic analysis is employed to determine whether graphene production occurs. The ion beam irradiation effects on the surface morphology are investigated with the scanning electron microscopy. At shallow ion beam incident angles (30°-45°) formation of nanocones/nanoneedles is observed, whereas at steeper angles (60°-90°) nanopores are exclusively produced

Due to the ease of GO preparation and its facile dispersability in water, GO is thought to be a promising candidate for the graphene production [42,43]. GO is insulating, as a result of the presence of the oxygen containing functionalities and has a corresponding wide bandgap [40]. Therefore GO needs to be reduced in order for it to exhibit graphene characteristics. This implies the removal of the oxygen containing functionalities. As mentioned in previous chapters, over the past several years various approaches have been developed for the reduction of GO (e.g. chemical [42-46], thermal

[47-50], photo [51-53] and laser reduction [54-60] approaches). The main challenge with the reduction methods is removal of the oxygen functionalities while preserving the graphene lattice. The main characterization technique for the determination of the defects and disorder in graphene is Raman spectroscopy. The observation of the G' peak generally signifies the formation of graphitic material. The high resolution analysis of the G' peak and its curve fitting can be correlated with the stacking order and number of graphene layers [117].

Argon ion beam irradiation is a standard surface science technique that is generally used for sputtering/cleaning the samples. More recently Ar ion irradiation has been used to produce nanostructures from several materials, specifically metal oxides [118], polymers [119,120] and carbon films [121]. Some of the more commonly used applications for these nanostructures include field emission applications. In the past several years the carbon cones were demonstated to be excellent low turn-on and low threshold field electron emitters.

In this chapter a method for the reduction of GO is presented that produces essentially oxygen free sp^2 hybridized material. This is verified with X-ray photoelectron spectroscopy (XPS). Additionally, formation of nanostructures is observed, and the morphology is dependent on the Ar ion beam incident angle. At shallow angles (30-45°) the formation of nanoneedles/nanocones is observed, whereas at steeper angles (60°-90°) nanopores are exclusively produced. The possible mechanisms of GO reduction as well as the origin of the morphological changes are discussed in section 4.4.

4.2 Experimental details

4.2.1 Sample preparation

The sample fabrication procedure used for the Ar ion reduction experiments are identical to the ones used for the GO laser reduction experiments described in Chapter 2. Briefly, GO (~ 29% oxygen content) was synthesized using the modified Hummers' method [37,38]. Thin (~ 10 μm) films were produced via high pressure filtration of the concentrated GO solution through a nylon membrane (200 nm pore size) and dried in a desiccator. The GO film was left attached to the nylon filter membrane for easier sample handling and mounting.

4.2.2 Experimental setup

Ar ion beam irradiation and X-ray spectroscopic analysis are performed in a commercial Thermo Scientific K-Alpha XPS system equipped with the monochromatic X-ray beam, Ar sputtering gun and an electron flood gun - all of which are positioned ~ 58° of the normal with respect to the sample (Figure 4.1). The ion gun energy can be varied between 200-3000 eV. Additionally, the ion beam spot size can be adjusted between 100-2000 μm in diameter. The Ar ion current can be varied from ~ 14-18 μA. By varying ion beam spot size and ion current, the desired ion flux (ions/cm^2) can be achieved. The vacuum chamber pressure during the irradiation was ~ 1×10^{-7} Torr.

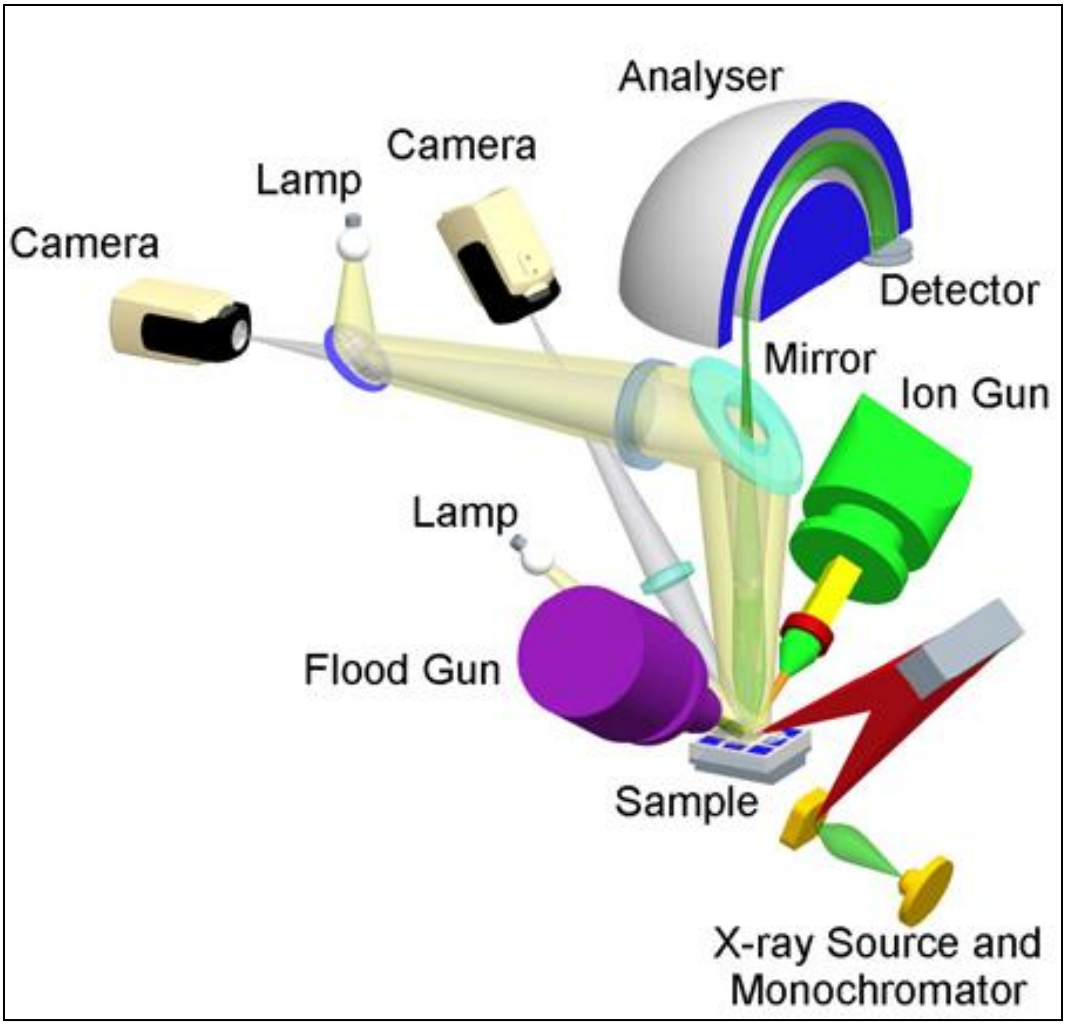

Figure 4.1: Experimental setup for the Thermo Scientific K-Alpha XPS system [122].

4.2.3 Irradiation parameters

Reduction of GO has been performed with Ar ion beam energies as low as 200 eV and as high as 3000 eV. Best results, in terms of decreasing the oxygen content of the untreated GO, are obtained when the reduction is performed with the Ar ion beam energy of 3 keV and ~ 17 μA current over the area of ~ 1.26×10^{-3} cm^2 (which corresponds to ion flux of ~ 8.45×10^{16} ions cm^{-2} s^{-1}). Effects of the irradiation time have been investigated as well. The experimental system is not equipped with the capability of

tilting the samples; therefore the angle dependence on the GO reduction has been probed by mounting GO samples on the precision machined aluminum stubs to achieve 30, 45, 60 and 90 degree angles with respect to the ion beam. It is important to note that the low energy flood gun must be operational during the argon ion sputtering experiments in order to neutralize the positive charge buildup on the sample. Positive charge buildup occurs due to the injection of the Ar^+ ions and simultaneous ejection of electrons under high energy Ar ion bombardment. Because of the flood gun operation, the net charge on the sample during the Ar ion irradiation should remain neutral.

4.3 Results

4.3.1 Raman characterization

Micro-Raman spectroscopy has proven itself as a reliable tool for elucidating structures of carbon materials. To determine whether Ar ion irradiation induces any chemical modifications, the untreated GO and the Ar ion irradiated samples were analyzed with a Bruker Senterra micro-Raman spectrometer with 532 nm laser excitation and 0.2 mW power through a 100× objective. Raman spectroscopic analysis of the untreated and Ar ion reduced GO is presented in Figure 4.2. Untreated GO has prominent D (~ 1353 cm^{-1}) and G (~ 1605 cm^{-1}) peaks as well as G' (~ 2694 cm^{-1}), D+G (~ 2920 cm^{-1}) and 2G (3168 cm^{-1}) peaks [117]. The Ar ion reduced GO also has D and G peaks, though their position and peak shape is different, with D peak shifted to ~ 1365 cm^{-1} and G peak position shifted to ~ 1584 cm^{-1}. The remaining peaks (G', D+G and 2G) are merged into one broad peak centered at ~ 2900 cm^{-1}. This figure clearly demonstrates that the Ar ion beam irradiation induces significant changes to the structure

of graphite oxide. The overall D peak intensity is decreased, though the peak is broadened. The G peak position shifts closer to the value that is commonly reported for graphite (~ 1582 cm^{-1}) [123]. The absence of a prominent G' peak in the Raman spectrum of the Ar ion reduced GO can signify that there is no well-ordered 3D graphitic structure, though it does not imply that the material is not sp^2 hybridized. The Ar ion reduced GO also does not belong to class of amorphous carbon materials, which can be readily identified by presence of a single broad G peak in a Raman spectrum. It is worth noting that Raman spectroscopic analysis is not surface sensitive, but rather probes a volume that is several micrometers (~ 1-3 µm) deep.

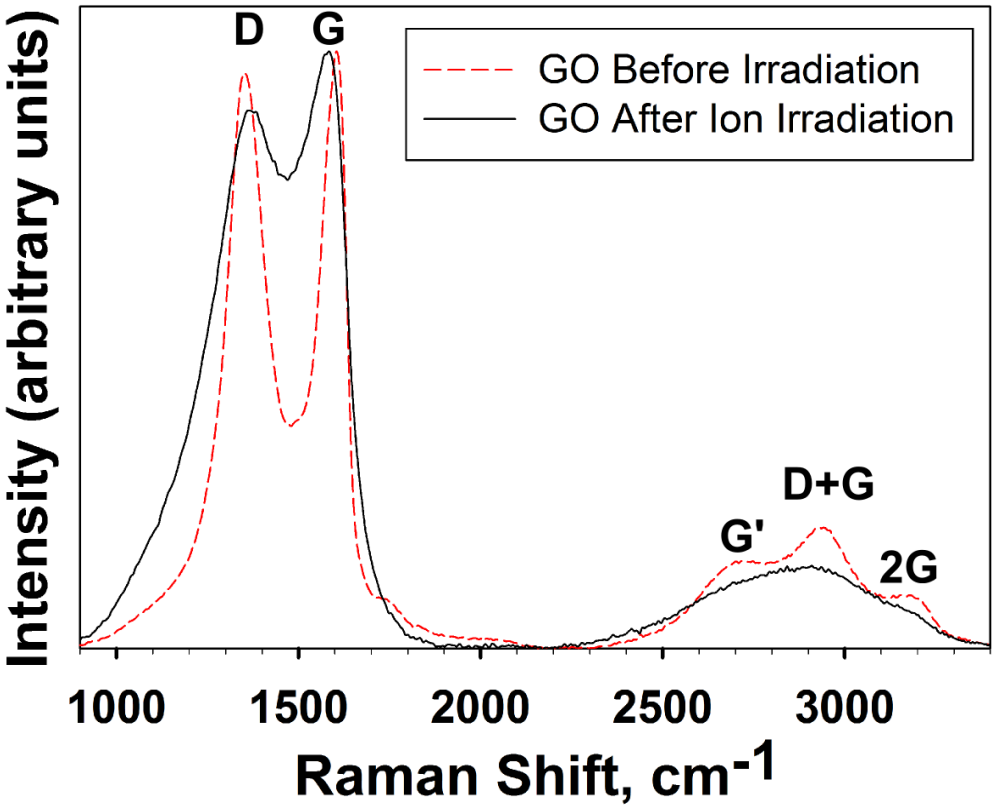

Figure 4.2: Raman spectroscopic analysis of the untreated and Ar ion irradiated GO (the spectra were normalized to G peak).

4.3.2 XPS characterization

X-ray spectroscopic analysis (XPS) has been performed with a Thermo Scientific K-Alpha XPS system. XPS allows elucidation of the elemental composition as well as the chemical bonding of the elements within the top (< 10 nm) portion of the sample. The bulk is not sampled due to the short escape depth of the photoelectrons. When XPS analysis is combined with Raman investigation of the Ar ion reduced GO sample, clearer chemical information emerges.

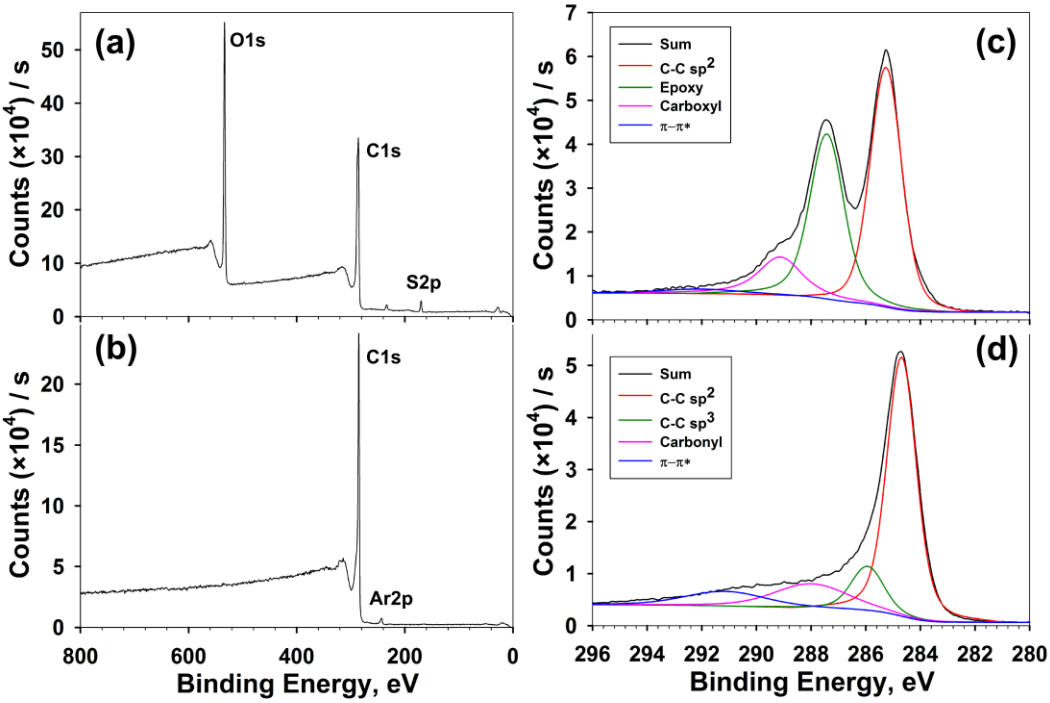

Figure 4.3: (a) XPS survey spectrum of the untreated GO (b) XPS survey spectrum of the 3 keV Ar ion irradiated GO (c) XPS C1s spectrum of the untreated GO (d) XPS C1s spectrum of the 3 keV Ar ion irradiated GO.

The almost complete removal of oxygen functionalities in the Ar ion reduced GO is evident from Figures 4.3a and 4.3b, which correspond to the untreated GO and reduced GO irradiated with 3 keV Ar ions for 240s, respectively. XPS analysis confirms that the oxygen content is reduced from the initial ~ 29% (~ 2.43 C/O ratio) to ~ 0.46%

(~ 215 C/O ratio) and the predominance of carbon with sp^2 character is observed after 240 s irradiation (Figures 4.3c and 4.3d). Peak fitting of the untreated and reduced GO spectra was performed with the Thermo Scientific K-Alpha XPS software. Untreated GO has the expected peaks corresponding to sp^2 hybridized carbon (~ 285.2 eV), carbonyl (~ 287.4 eV) and carboxyl (~ 289.12 eV) functionalities as well as a broad π-π* shakeup peak at ~ 292 eV. Ar ion reduced GO has a dominant peak corresponding to sp^2 carbon (~ 284.7 eV), as well as peaks corresponding to sp^3 carbon (~ 285.9 eV) and carbonyl (~ 287.98 eV) functionalities. The π-π* shakeup peak is also observed at ~ 291.2 eV. The primary difference is in the diminishing of the peak intensities corresponding to the oxygen containing functionalities. Continuous Ar ion irradiation for at least 240 s is essential for achieving the highest possible C/O ratio.

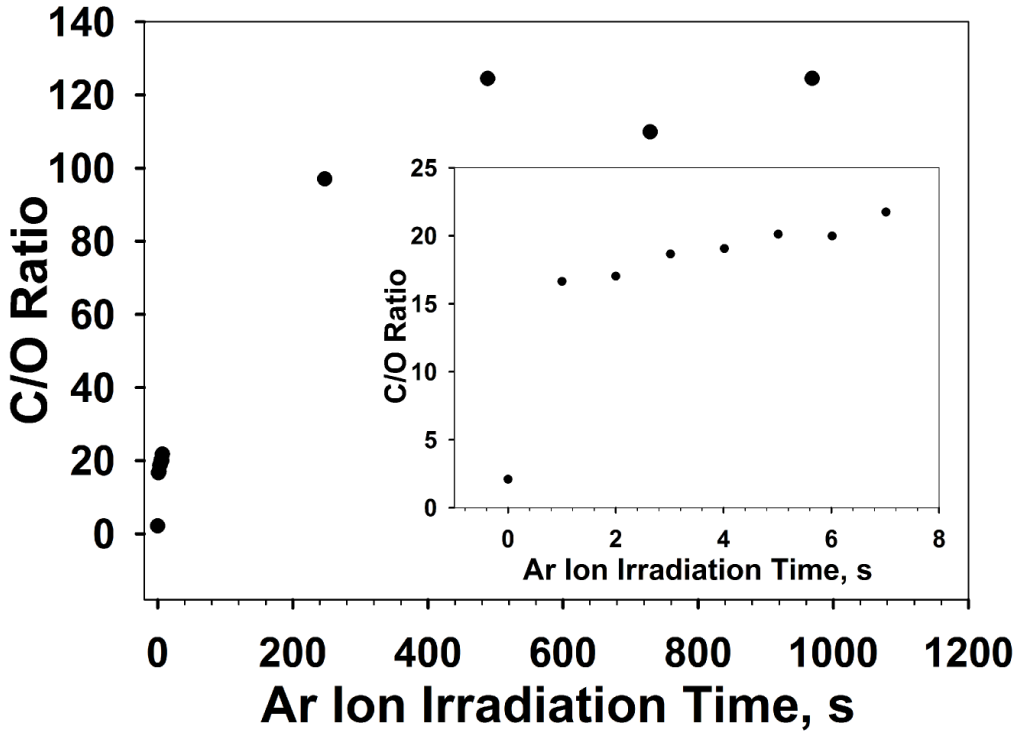

Figure 4.4: C/O ratio as a function of Ar ion irradiation time.

When reduction is performed in steps, the highest C/O ratio that could be obtained is 97 for the same 240 s total irradiation time (Figure 4.4). The electron flood gun is operational at all times. The time between each irradiation step is used to perform the XPS analysis of the freshly irradiated area. This lower C/O ratio can possibly be attributed to the neutralization with the electron flood gun of the accumulated positive charge due to Ar^+ ion irradiation and, thus, decrease in efficiency of oxygen functionality removal. It is also observed, that the initial reduction occurs very rapidly: after only 1 s of ion irradiation, the oxygen content is decreased from ~ 29% to ~ 5.67% as shown in Figure 4.4 inset.

4.3.3 SEM characterization

Scanning electron microscopy (SEM) imaging has been performed on the Zeiss Ultra60 FE-SEM. Accelerating voltage has been set at 15 keV and the working distance has been fixed at 4 mm. All samples have been grounded to prevent charge buildup on the sample surfaces resulting in image quality deterioration. Figure 4.5a depicts the untreated GO film image. Due to the method of GO film formation (GO solution high pressure filtration), individual graphene oxide flakes directly overlap each other in random orientation, producing a smooth surface. Figures 4.5b and 4.5c represent two different GO samples after the 240 second 3 keV Ar ion irradiation at 30° and 45° angles with respect to the Ar ion gun. Formation of the conical structures is observed, with some of the sharper conical structures having additional extratips with a diameter of ~ 20-30 nm. These extratips can be also referred to as nanowhiskers or nanowires. The overall nanocone density produced with the 240 s 3 keV Ar ion irradiation at 30° angle

with respect to the ion beam is ~ 1.2×10^9 nanocones/mm^2 (~ 1.2×10^{11} nanocones/cm^2) as determined from the SEM image 4.5b. When all of the parameters are kept the same but the angle of irradiation of the newly prepared GO films is increased to 60° and 90° with respect to the ion beam (Figures 4.5c and 4.5d), nanoconical structures are not observed. Instead, GO surfaces are dominated by interconnected nanopores. The diameter of the nanopores for both 60° and 90° irradiation angles varies between ~ 50-100 nm, and the width of the walls separating one pore from another is ~ 20-30 nm. The density of nanopores produced at 60° irradiation angle (Figure 4.5d), is ~ 1.2×10^8 nanopores/mm^2 (~ 1.2×10^{10} nanopores/cm^2).

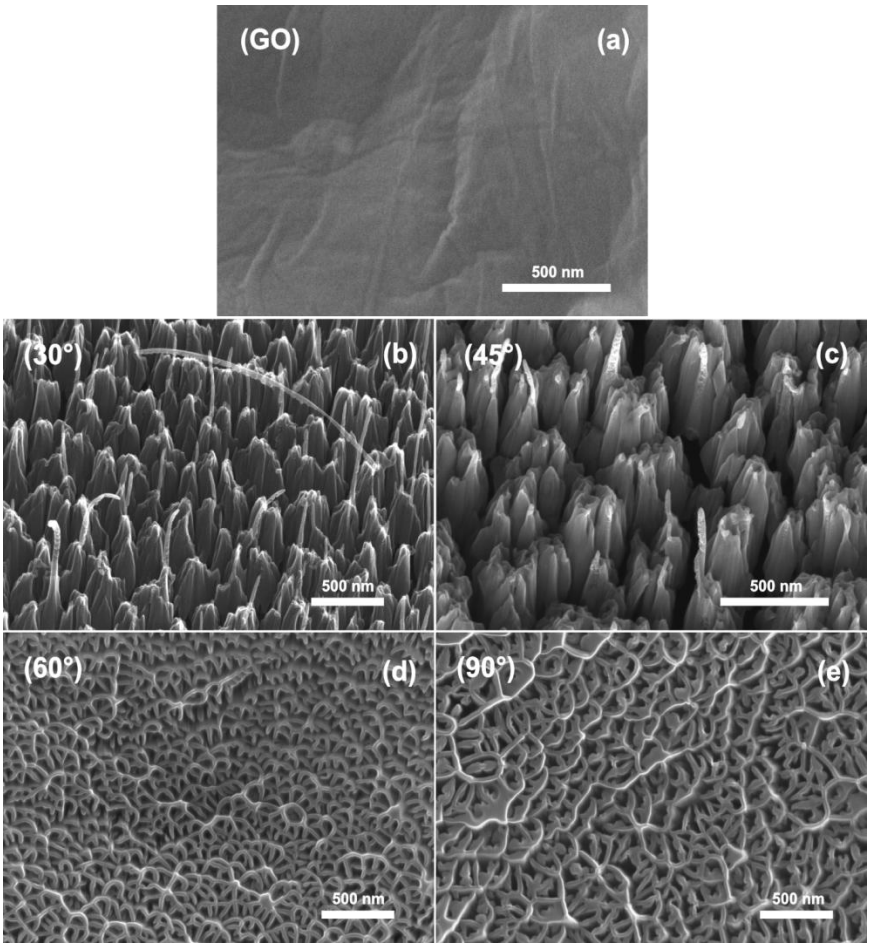

Figure 4.5: (a) SEM image of the untreated graphite oxide (GO). (b-e) SEM images of the Ar ion irradiated GO at 30°, 45°, 60° and 90°.

4.3.4 Electrical characterization

Besides chemical (Raman and XPS) and morphological (SEM) characterization of the Ar ion reduced GO films, it is also desirable to elucidate electrical properties of these materials. By using the 4-point probe measurement approach [94], sheet resistance of the 3 keV Ar ion irradiated GO film is determined to be ~2500 Ω/sq. For comparison, the sheet resistance of the untreated GO has been previously reported to be ~ 4×10^{10} Ω/sq [40]. Thus, Ar ion irradiation of GO results in material that is significantly more conductive than the untreated GO film. Additionally, to further characterize its electrical behavior, IV curve has been obtained at room temperature in vacuum and is demonstrated in Figure 4.6. It is clear from Figure 4.6 that the material exhibits ohmic behavior, which simply means that this material obeys Ohm's law ($\frac{V}{I} = R$). Effects of temperature on the IV characteristics of the Ar ion reduced GO are beyond the scope of this study.

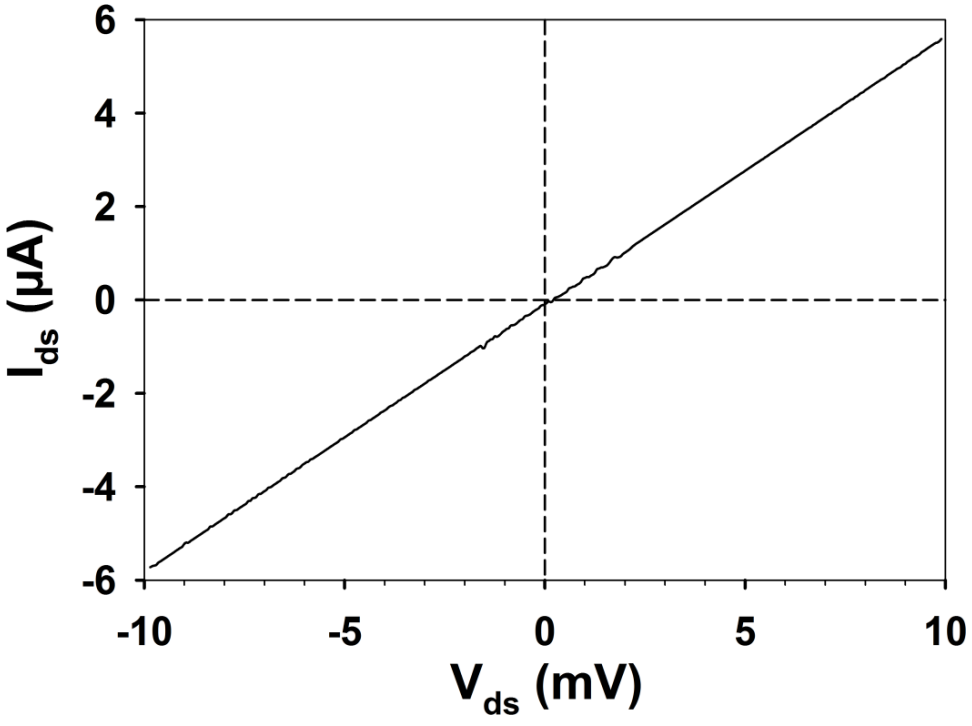

Figure 4.6: IV curve of 3 keV Ar ion irradiated GO.

4.4 Proposed mechanisms

4.4.1 Graphite oxide reduction

It has been shown in the XPS characterization section 4.3.2, that upon 3 keV Ar ion irradiation of GO predominantly sp^2 hybridized carbon material is formed. The process is highly efficient and takes as little as 240s of irradiation time to achieve almost 100% removal of oxygen functionalities. Though the mechanism of oxygen removal from GO under ion irradiation would involve examination of the sputtered products with quadrupole and time-of-flight mass spectrometric techniques as well as careful measurement of the sputtering yields, some mechanistic information can be gleaned from the GO laser reduction work described in Chapter 2 as well as previously published works on ion irradiation of surfaces.

Argon ion reduction of GO is a complex process that cannot be explained by a single mechanism, but rather a combination of several pathways. Due to the high ion flux during the continuous 240s 3 keV Ar ion irradiation of GO (8.45×10^{16} ions cm^{-2} s^{-1}), the resulting temperature increase would initiate the reduction process on the surface of GO, rapidly decreasing its oxygen content. Continuation of the irradiation also results in the formation of defects and vacancies, primarily via the localization of holes in the top of the valence band of GO. The subsequent repulsive hole-hole Coulomb interactions result in material ejection. Strain associated with the oxygen functionalities can also lead to an enhancement in energy localization and, thus, a more efficient GO reduction [100,101]. In addition to the thermal reduction and hole localization pathways induced by high Ar ion fluxes, direct breaking of the carbon-oxygen bonds (specifically the epoxy and hydroxy functionalities) via a process known as chemical sputtering plays a significant

role as well. Additionally, the sufficiently high energy 3 keV Ar ions create a cascade of secondary electrons and ionic species, which participate in the stimulated desorption processes resulting in an enhancement in the removal of oxygen functionalities, and sp^2 hybridized carbon bond formation.

Previously published work on the ion irradiation of materials sometimes attribute the rapid reduction in oxygen content in the samples to oxygen's preferential sputtering as well. This phenomenon is known to occur in oxygen containing polymers [124,125] and metal oxide compounds, though degree of contribution of preferential sputtering versus other models is not clear [118]. Graphitization of sp^3 hybridized carbon structures and polymeric materials has been known to occur when ion beam irradiation with a sufficiently high ion beam density is used [120]. It has been suggested that the polymers containing phenyl groups (benzene ring components) are easier to graphitize with ion irradiation [126]. This can contribute to the predominantly sp^2 hybridized carbon bond formation in Ar ion reduced GO as well.

4.4.2 Surface modification: nanocone and nanopore formation

For the ion energy below 10 keV the morphological changes of the surface can be initiated by the defects and grain boundaries [127] and are dominated by the competing processes of material removal and diffusion, resulting in the formation of uniquely different features depending on the angle of ion irradiation. Positively charged Ar ion beam and its high flux can also play a deciding factor in determining which areas of GO are sputtered and which ones remain intact or sputtered at a lower rate. If charge is

localized on the sample and if its buildup is sufficiently high, these regions can efficiently deflect the incoming Ar ion beam, thus creating an anisotropic sputtering effect.

The mechanism that would account for the growth of the long extratips (~ 20.5 nm diameter) on the nanocones (Figure 4.7) can be attributed to the surface movement of carbon atoms along the sidewalls of the growing nanocones [128,129]. That motion has been previously suggested to be mediated by thermal diffusion or the ion beam generated electric fields [121]. Figure 4.7 inset also reveals that the nanocones with the sharp tips, specifically ~ 26.8°, seem to be most suitable for the extratip growth.

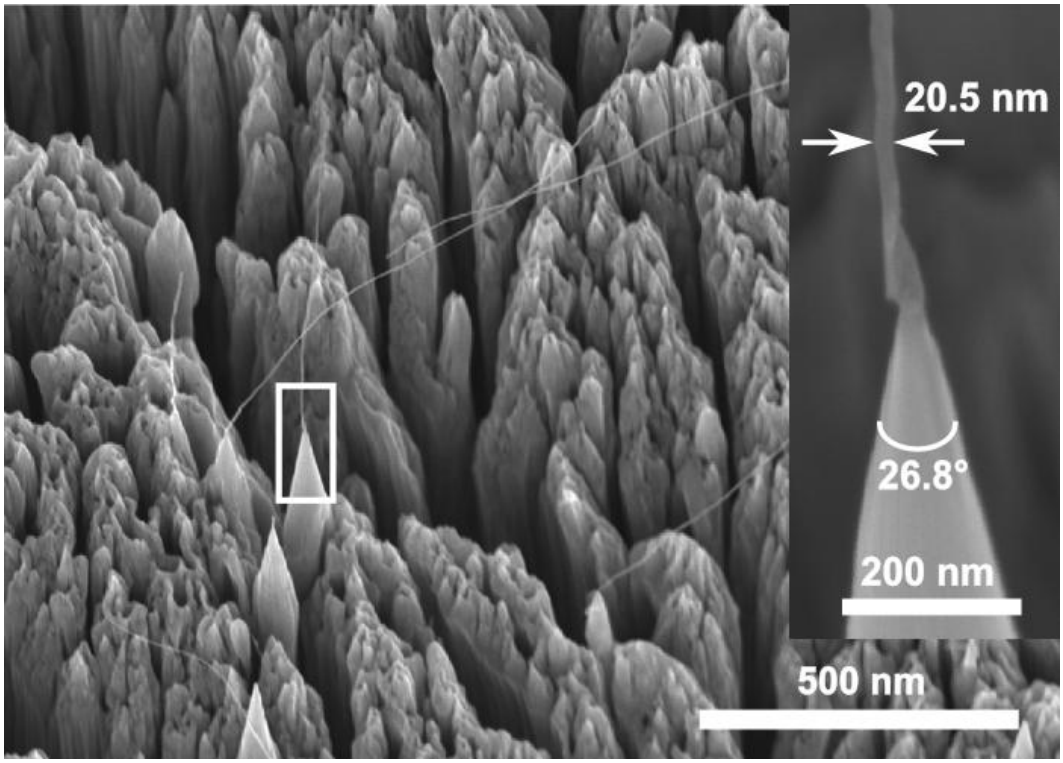

Figure 4.7: SEM image of Ar ion irradiated GO resulting in the formation of long extratips (inset is a higher magnification view of one of the nanocones with an extratip).

4.5 Applications and future outlook

Patterning of nanoconical structures on GO can be readily achieved by using a sacrificial masking layer (Figures 4.8a and 4.8b) and irradiating GO at shallow angles (e.g. 30° or 45° angles). A 2000 mesh copper grid is brought in contact with untreated GO and a 1 mm × 1 mm area is irradiated with a 300 μm diameter spot size ion beam with a 300 μm step size at 45° angle with respect to the Ar ion beam. Formation of ~70 nm diameter nanoneedles (Figure 4.8b) is observed in the exposed areas and no nanoneedle formation is present in the masked areas. These structures can possibly be used as field emitters. Also, the porous structures observed in figures 4.5d and 4.5e can serve as excellent substrates for laser desorption mass spectrometry.

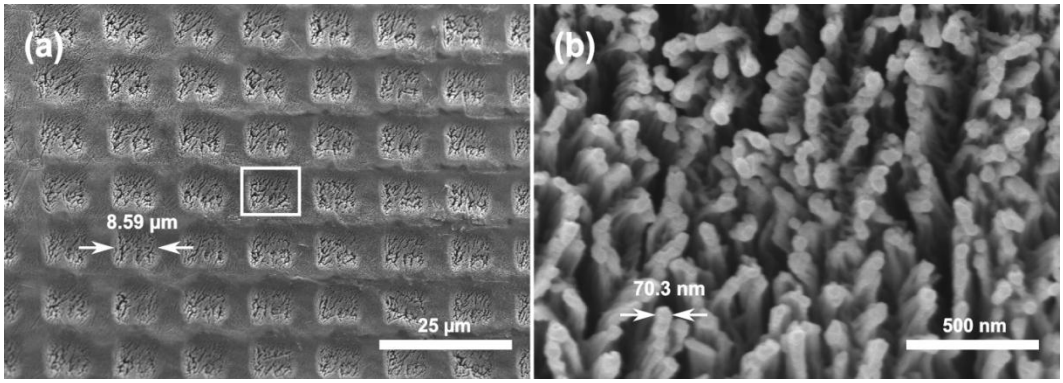

Figure 4.8: (a) Rectangular patterns of nanocones produced by Ar ion irradiation of GO through a copper shadow mask. (b) Higher magnification view of one of the highlighted irradiated areas in (a).

4.6 Conclusions

In conclusion, Ar ion beam irradiation of graphite oxide results in nearly complete reduction of GO. This leads to the production of sp^2 hybridized carbon material with extremely high C/O ratio of ~ 215. The reduced material exhibits a low sheet resistance value of ~ 2500 Ω/sq and the IV curve confirms that the material exhibits ohmic behavior. The Ar ion GO reduction method has the advantage of forming unique surface morphologies which can be precisely controlled by varying the angle of irradiation and the ion beam flux. At shallow angles (30°-45°) nanoneedles and nanocones are exclusively formed with exceptionally high nanocone density of ~ 1.2×10^9 nanocones/mm^2 (~ 1.2×10^{11} nanocones/cm^2). These nanocones can be also decorated with long extratips with a diameter of ~ 20 nm. At steeper angles of irradiation (60°-90°) only nanopores are produced with pore diameters of ~50-100 nm and a density of ~ 1.2×10^8 nanopores/mm^2 (~ 1.2×10^{10} nanopores/cm^2). Controlled microscale patterning of interchanging regions of untreated GO and nanoneedle regions using the shadow masking approach has been demonstrated as well.

CHAPTER V

MULTILAYER EPITAXIAL GRAPHENE GROWTH ON CARBON FACE SILICON CARBIDE IN ULTRA-HIGH VACUUM

5.1 Introduction

Chapter 1 introduced the reader to various ways of making graphene, with epitaxial graphene growth on SiC being one of the well-established approaches. Though now it is possible to grow virtually defect free graphene films on SiC with tunable number of layers and large domain sizes [15,130-133], the mechanisms by which graphene growth occurs are not yet well understood. Graphene has been reported to grow on various SiC polytypes, with most experiments performed on hexagonal polytypes 4H [134-136] and 6H [137-139]. Additionally, through experimentation, it has been determined that graphene grows differently depending on the hexagonal SiC crystal polarity. The SiC(0001) crystal orientation is generally referred to as silicon face (Si-face), whereas the SiC($000\bar{1}$) is referred to as carbon face (C-face). Due to the reasons currently not yet well understood, under the same growth parameters the rate of graphene formation on C-face is greater than on the Si-face [136,140].

All of the experiments in this chapter are performed on C-face SiC. Growth parameters during graphene epitaxy on silicon carbide can greatly affect its final chemical composition [141]. Though the detailed mechanisms governing the growth of epitaxial graphene on C-face SiC are not well understood, the commonly accepted mechanism for graphene formation is thought to be the sublimation of silicon, which creates a carbon rich layer on the SiC surface. The carbon rich layer rearranges to form

graphene. The study described in this chapter examines the growth process by monitoring the production and release of subliming species as a function of temperature and heating duration on the carbon terminated surface of pristine SiC samples under ultrahigh vacuum (UHV) conditions. Specifically, *in-situ* quadrupole mass spectrometry (QMS) is used to investigate the nature of the chemical species produced and desorbed during the heating of SiC up to ~ 1800 °C. The resulting films are analyzed with X-ray photoelectron spectroscopy (XPS) to determine their elemental composition and the distribution of functional groups. Depth profiling using XPS and Ar ion beam sputtering is also employed in this study. The XPS depth profiling specifically monitored the distribution of carbon and silicon species in the thick multilayer graphene film. This technique also allows graphene growth rate determination, given the known growth time. Section 5.3.3 presents a preliminary kinetic model based on the Arrhenius equation in conjunction with mass spectrometric data. This model allows the determination of the energy of silicon sublimation and transport. Additionally, by maintaining the SiC temperature at ~ 1700°C and monitoring the intensity of subliming silicon species as a function of time, changes in the rate of Si sublimation are monitored. After the initial expected decrease in the Si sublimation rate, a sudden increase in Si sublimation is observed. Detailed observations and explanations of this phenomenon are presented in section 5.3.2.

5.2 Experimental setup

Experiments are performed in an ulta-high vacuum (UHV) chamber with a base pressure of ~ 1.2×10^{-10} Torr (Figure 5.1). The pressure in the chamber is monitored with a Granville-Phillips ion gauge, positioned in a 90° angle elbow fitting. The chamber is equipped with an Extrel quadrupole mass spectrometer (1-100 amu mass range), precision leak valve, two glass viewports and a Raytek 1MH optical pyrometer calibrated for 1 μm wavelength with an analysis spot size diameter of ~ 1 mm. The sample is positioned directly in the line of sight of the QMS, ~ 7 cm away from the ionizer.

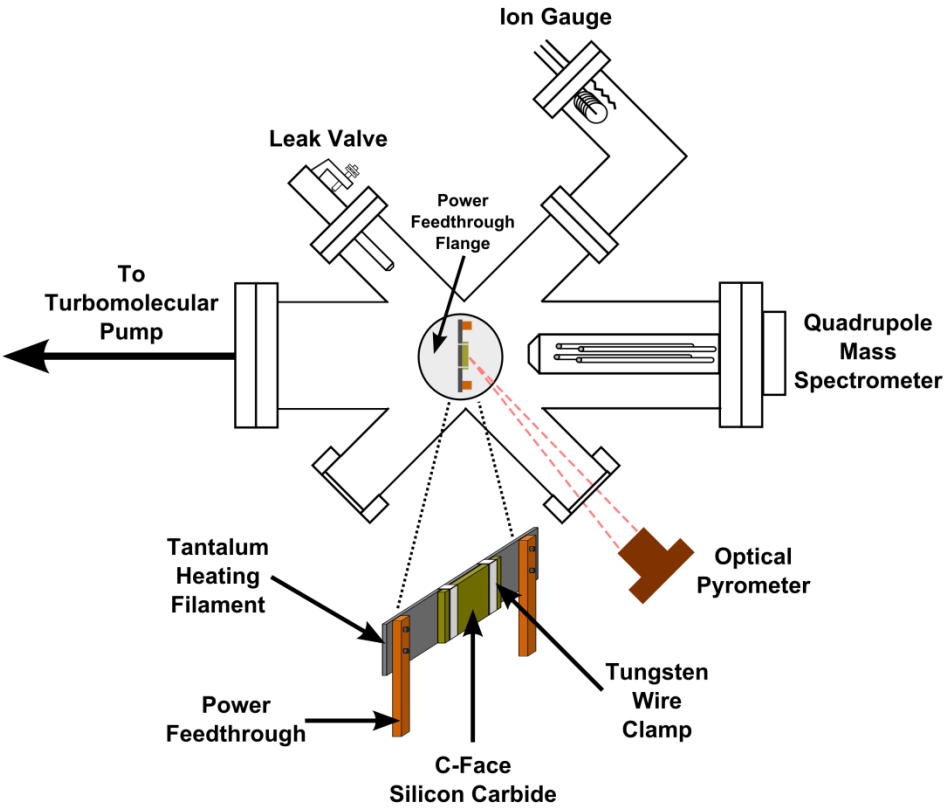

Figure 5.1: Schematic diagram of the experimental setup.

The 3 mm × 4 mm 4H-SiC sample is mounted directly on the 50.8 μm (0.002 inch) thick 3 mm × 20 mm tantalum foil which serves as a filament heater. A 25.4 μm (0.001 inch) diameter tungsten wire is wrapped repeatedly around the edges of the SiC sample and the tantalum heater, bringing them in rigid contact with each other. The center portion of the SiC sample remains unobstructed for temperature measurements with an optical pyrometer. The heater-sample assembly is then attached to the high current copper power feedthroughs (mounted on a CF flange) either directly or via additional molybdenum clamps. This allows for heat dissipation and prevents excessive heating of the copper feedthroughs. Stainless steel screws are used to connect the heater-sample assembly to the power feedthroughs and to the molybdenum clamps. This mounting configuration is found to be most optimal for achieving uniform sample heating. Prior to placing the entire structure in the vacuum chamber, the sample-heater-feedthrough assembly is sonicated in hexane for 30 min and then dried with a heat gun at temperatures reaching ~ 400 °C to burn off any remaining carbon on the surface of the sample.

After placing the sample assembly in the UHV chamber, the chamber is pumped down and then baked for 72-96 hours at ~ 120-150 °C to remove any adsorbed molecular species on the chamber walls. The optical viewports are baked at lower temperature to prevent their damage. The QMS ionizing filament is kept on and the SiC sample is kept at 1000 °C during the chamber baking in order to desorb already present contaminants and also to prevent adsorption of contaminants from the chamber walls. The heating of the sample is achieved by resistively heating the tantalum heating filament with a Mastech HY3050E high current power supply. Modifications to the power supply were

made according to the manufacturer's recommendations in order to be able to pass current through a low resistance heating filament.

It is important to mention that before this sample mounting strategy was finalized, other configurations were explored as well. Special attention was given to ensuring accurate temperature measurements. Initially, a combination of the high temperature type C (tungsten-rhenium) thermocouple and an optical pyrometer was used. During the course of experiments it was determined that high temperature thermocouple measurements were unreliable, due to the rapid deterioration of the thermocouple wire. This deterioration was facilitated by the high temperature (> 1400 °C) chemical reaction between the SiC substrate and tungsten in the thermocouple due to the formation of tungsten carbide and tungsten silicide. At lower temperatures, the pyrometric and thermocouple temperature measurements were in agreement. As previously mentioned, the optical pyrometer was well calibrated by the manufacturer up to the 3000 °C.

5.3 Results

5.3.1 Subliming species analysis

Determination of the desorbing species during the high temperature growth of graphene on C-face SiC in UHV is important in order to better explain the mechanism of graphene formation under these conditions. Though it is generally assumed that silicon is the primary component of the subliming species, a careful mass spectrometric measurement has not been previously performed. In this study, a SiC sample has been prepared according to the procedure outlined in the previous section 1.2. For all of the mass spectrometric measurements described in this chapter, only positively charged

species (cations), produced via 70 eV electron-impact ionization of the desorbing neutrals, are analyzed. During the experiment, the sample is first heated to ~ 1250 °C and the background spectrum in the 1-75 amu mass range is obtained. The sample is then rapidly heated to ~ 1800 °C with a ramp rate of ~ 600 °C/s. As soon as the temperature is reached, another mass spectrum in the 1-75 amu mass range is obtained. The background spectrum is subtracted from the spectrum obtained at 1800 °C and the final result is shown in Figures 5.2. Figures 5.3 and 5.4 are magnified regions of Figure 5.2. In these figures, some of the peaks appear to have a non-uniform structure. This is due to spectrum subtraction and the imperfections of the QMS's electronics.

From these figures it is clear that a multitude of species is sublimed from the C-face SiC surface. As expected, the signal from $^{28}Si^{+}$ is dominant. Identity of silicon is confirmed by also observing its ionized isotopes ($^{29}Si^{+}$ and $^{30}Si^{+}$) in the appropriate ratios. Various SiC and carbon fragments are observed as well.

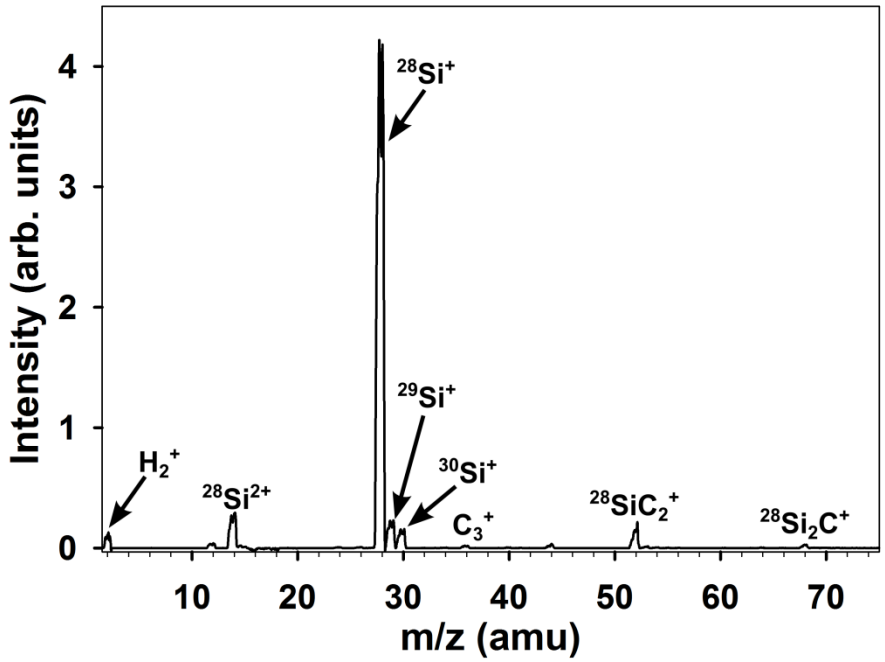

Figure 5.2: Mass spectrum obtained for C-face SiC heated to 1800 °C (1-75 amu range)

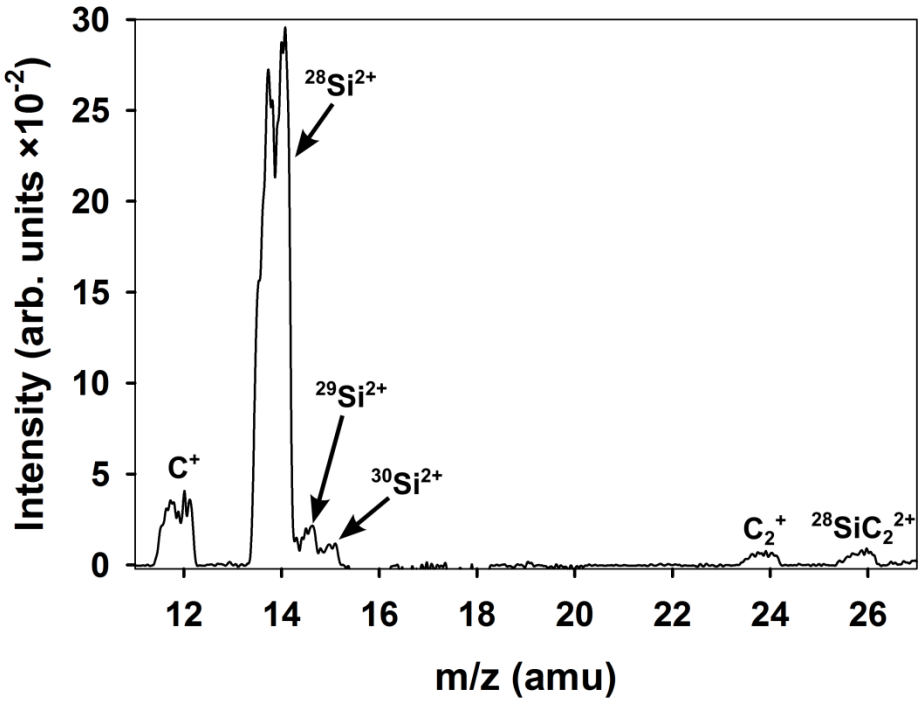

Figure 5.3: Mass spectrum obtained for C-face SiC heated to 1800 °C (10-27 amu range)

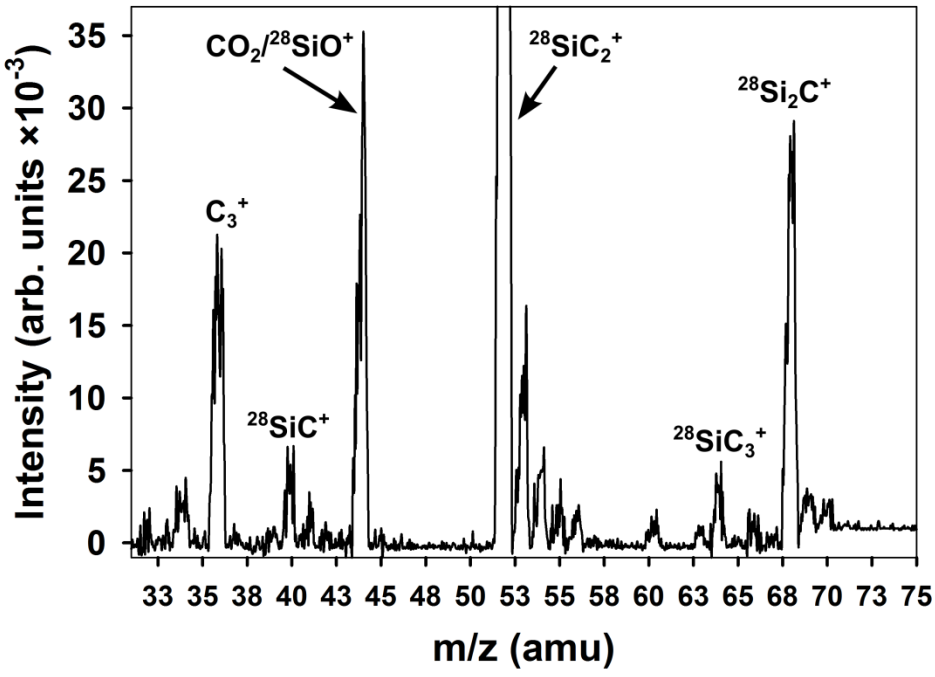

Figure 5.4: Mass spectrum obtained for C-face SiC heated to 1800 °C (31-75 amu range)

5.3.2 Subliming species analysis as a function of time

High quality epitaxial graphene growth on SiC does not occur instantaneously; rather it takes a period of time that greatly depends on the substrate temperature, heating rates and the desired number of graphene layers. Thus, it is advantageous to know the evolution of subliming species as a function of heating time. For these experiments, the SiC substrate has been prepared according to the previously described procedure in Section 5.2. During the experiment, the sample is rapidly heated to ~1700 °C with a ramp rate of ~ 600 °C/s and, once the desired temperature is reached, it is maintained at that level. Also, the QMS begins continuously recording spectra, with a rate of one full spectrum (1-75 amu) obtained in 86.68s. The total runtime of the experiment is 4000s. The monitored masses are: m/z = 2 (H_2^+), 12 (C^+), 14 ($^{28}Si^{2+}$), 18 (H_2O^+), 28 ($^{28}Si^+$), 29 ($^{29}Si^+$), 30 ($^{30}Si^+$) and 44 ($CO_2/^{28}SiO^+$) and their evolution is shown in Figures 5.5c and 5.6c. In addition to monitoring the specified masses, the heater resistance and power values are also recorded as a function of time and are presented in Figures 5.5 a,b and 5.6 a,b.

From Figure 5.5c it is clear that masses corresponding to silicon are undergoing unexpected evolution as the heating time progresses. Specifically, the intensity of masses 14, 28, 29 and 30 amu steadily declines after the initial ~ 1500 seconds. The intensities of these masses then begins to grow again. At time ~ 2250s, the intensities of the masses either exceed or approach the initial values. These observations suggest that major transformative changes occur within the SiC crystal after ~1500s heating at 1700 °C. The nature of these changes is not yet understood and it will be challenging to understand them solely from the QMS studies. X-ray diffraction techniques would be more

appropriate for elucidating the structural changes within crystal as a function of heating time.

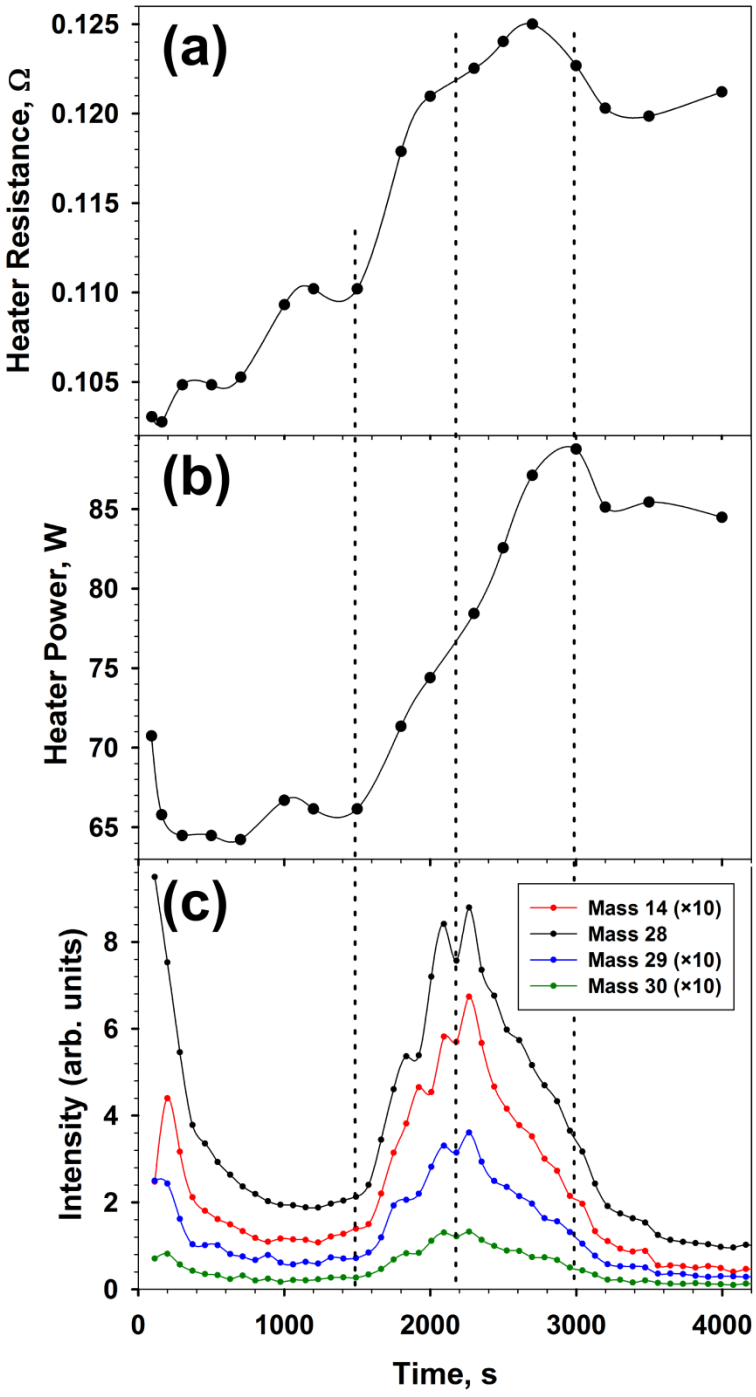

Figure 5.5: Desorption of atomic Si from C-face SiC maintained at 1700 °C (a) Heater resistance vs. heating time. (b) Heater power vs. heating time. (c) Evolution of Si associated masses (14, 28, 29, 30 amu) vs. heating time.

When analyzing data in Figure 5.5c, it is important to monitor the behavior of the heater to rule out the increase in silicon emission due to the increase in heating power. By observing the curves in Figures 5.5 a,b corresponding to heater resistance and heater power as a function of heating time, it becomes clear that the increase in rates of silicon sublimation is independent from heater behavior. Rather the observed heater behavior is a direct result of increased silicon emission.

At ~ 1500s, an increase in silicon sublimation is observed. This most likely accomplishes two things: 1) increase in sample cooling due to rapid loss of thermal energy through silicon sublimation, and also 2) initiation of an additional chemical reaction between the SiC substrate and tantalum heater, that decreases heater efficiency. Both of these events cause a decrease of sample's temperature. As a result, the power supplied to the heater has to increase to maintain a constant value of ~1700 °C. As the continuation of increased silicon emission progresses, reaching midpoint at ~ 2250s, power supplied to the heater is still continuing to rise for another ~ 750s, beyond the maximum point of silicon emission. After the emission midpoint at ~ 2250s, the rate of silicon emission begins to decline, but the heater power is still continually rising. If the increase in heating power is responsible for an increased silicon emission, the intensity of silicon masses should continue to rise. But just the opposite occurs. At the point of maximum heater power at ~ 3000s, the silicon emission is almost at its lowest point. Thus, an increase in silicon emission is independent of the heater behavior. This suggests that real transformations within the SiC crystal,buried interface or graphitic overlayer are causing this event to occur.

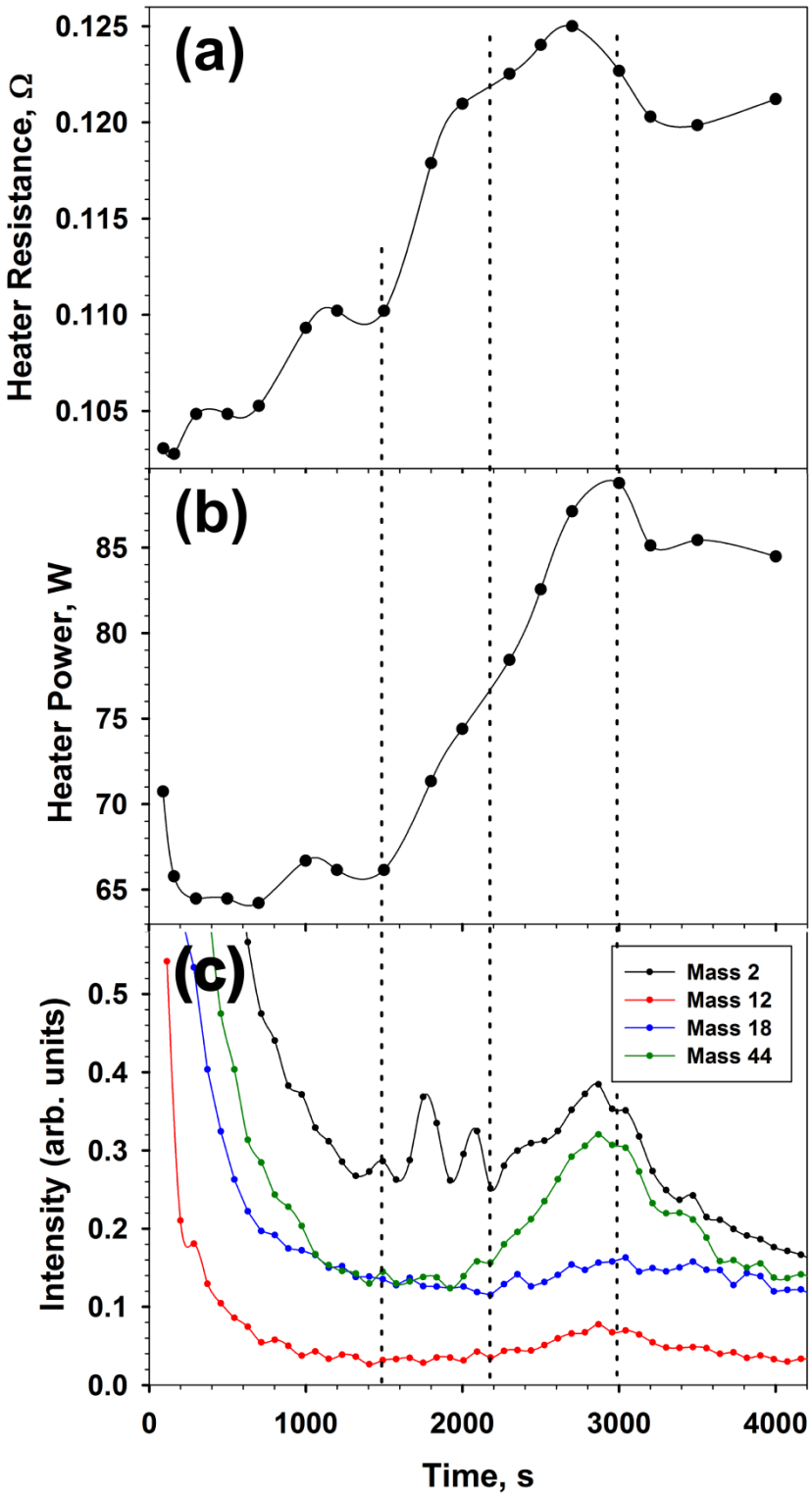

Figure 5.6: Desorption of atomic Si from C-face SiC maintained at 1700 °C (a) Heater resistance vs. heating time. (b) Heater power vs. heating time. (c) Evolution of non-Si associated masses (2, 12, 18, 44 amu) vs. heating time.

The possibility of chemical reaction occurring between the tantalum heater and SiC substrate can be gleaned from an unusual increase in heater resistance during the increased silicon emission timeframe (Figure 5.5a). Though the chemical reaction is definitely possible, it is not the cause for the observed silicon emission increase. This is concluded by applying the same logic as with the heater power analysis in the previous paragraph. Before the initiation of the rapid silicon emission, the resistance of the heating filament is continually rising due to the chemical reaction between tantalum and SiC. This rise in resistance is linear due to steady supply of silicon atoms. At the onset of excessive silicon emission at ~1500s, the linear increase of resistance is no longer true for the duration of the emission process. The reaction rate between the tantalum heater and silicon increases, due to increased supply of the latter. At the conclusion of the emission process at ~ 3500s, the heater resistance behavior becomes linear once again (Figure 5.5a), due to a more steady supply of silicon and the power of the filament stabilizes as well (Figure 5.5b).

During the above mentioned increase in silicon emission process, the other monitored masses m/z = 2 (H_2^+), 12 (C^+), 18 (H_2O^+), and 44 ($CO_2/^{28}SiO^+$) behave differently compared to silicon species (Figure 5.6c). These masses most likely represent increased emission from the chamber background due to the increased heater power output (Figure 5.6b) and subsequent heating. This is corroborated by the observation that the maxima for these species coincides with the maximum of the heater power output at ~ 2850-3000s heating time.

The main question that is left to be addressed is: why does the SiC crystal abruptly increase the output of silicon for a period of time during the extended heating

process? This phenomenon is contrary to the expectation, that when graphene layers are formed it would be harder for silicon to escape, thus resulting in a progressive decrease in silicon sublimation. Unfortunately, without performing additional experiments that focus specifically on the SiC bulk structure during the high temperature heating, it is challenging to address this question fully. It is likely that the SiC crystal itself has nothing to do with the increase in silicon sublimation. Rather, as the growth of graphene layers continues, large quantities of Si atoms are being trapped in the interlayer gaps and pores. As growth of graphene progresses the stresses and compressive strain associated with this process increase, resulting in a spontaneous rearrangement of graphene layers (i.e. twisting, buckling, etc.) to acquire a lower energy state. This opens up new paths for the trapped silicon to escape through, thus resulting in an observed increase in silicon sublimation.

5.3.3 Determination of silicon energy of sublimation from C-face SiC in ultra-high vacuum

In order to understand the mechanism of graphene formation in detail, it is crucial to understand the energies associated with this process; specifically the energy required for the silicon atoms to sublime from the surface of SiC and, when multilayers of graphene are formed, the energy required for passing through the graphene layers as well. In principle these two energies should be easily determined and differentiated from one another. In practice, separating these two values becomes challenging and only a combined energy can be derived. This combined energy will be referred to as the energy

of sublimation. This complication arises as a result of the detection limit of the QMS and the fast rate of graphene growth on C-face SiC at high temperatures.

For the experiment, the SiC sample is prepared according to the procedure in Section 5.2. During the experiment, the sample is first heated to ~ 1250 °C and the mass spectrum in the 1-75 amu range is obtained as a background. The sample is then rapidly heated to ~ 1800 °C and held at that temperature for 5 minutes to accumulate layers of graphene. After 5 minutes, the mass spectrum is acquired. The temperature is then decreased to 1700 °C and the mass spectrum is acquired again. The same procedure is repeated for 1600 °C and for 1500 °C. No discernible silicon sublimation is observed below 1500 °C with the QMS used for the experiment. The background spectrum is subtracted from the spectra obtained at the above mentioned temperatures and the area under the mass 14 ($^{28}Si^{2+}$) is plotted as a function of acquisition temperature (Figure 5.7).

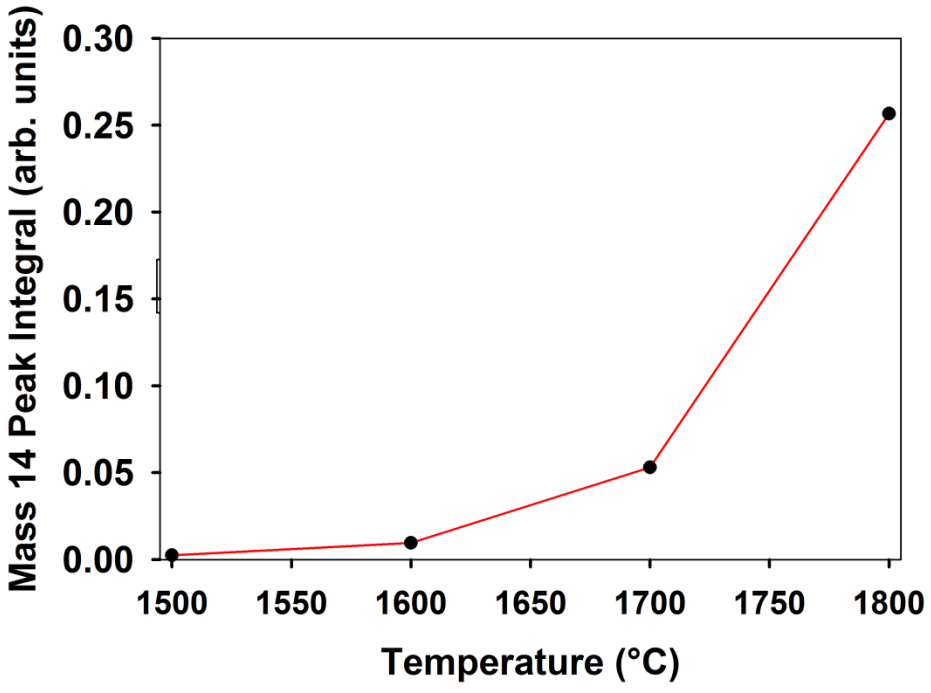

Figure 5.7: Mass 14 ($^{28}Si^{2+}$) evolution as a function of temperature.

Mass 14 ($^{28}Si^{2+}$) is chosen over mass 28 ($^{28}Si^{+}$), because in these experiments, considering the chamber background species, mass 14 uniquely belongs to silicon, whereas mass 28 can contain contributions from CO and N_2. These contributions can skew the measured values.

The energy of silicon sublimation is calculated from the linear Arrhenius equation $Ln(K) = \frac{-E_a}{k_b} \times \frac{1}{T} + Ln(A)$, where $Ln(K)$ (natural logarithm of the area under the mass 14 peak) is a function of inverse of the temperature $\frac{1}{T}$ (units of Kelvin) with a slope $\frac{-E_a}{k_b}$ and intercept $Ln(A)$. E_a is the energy of sublimation (in units of eV) and k_b is the Boltzmann constant expressed in units of eV K^{-1} ($k_b = 8.62 \times 10^{-5}$ eV K^{-1}). Graphically, this is represented in Figure 5.8. The energy of sublimation E_a is, thus, determined to be ~ 5.5 eV, which is in close agreement with the reported values in the literature [142].

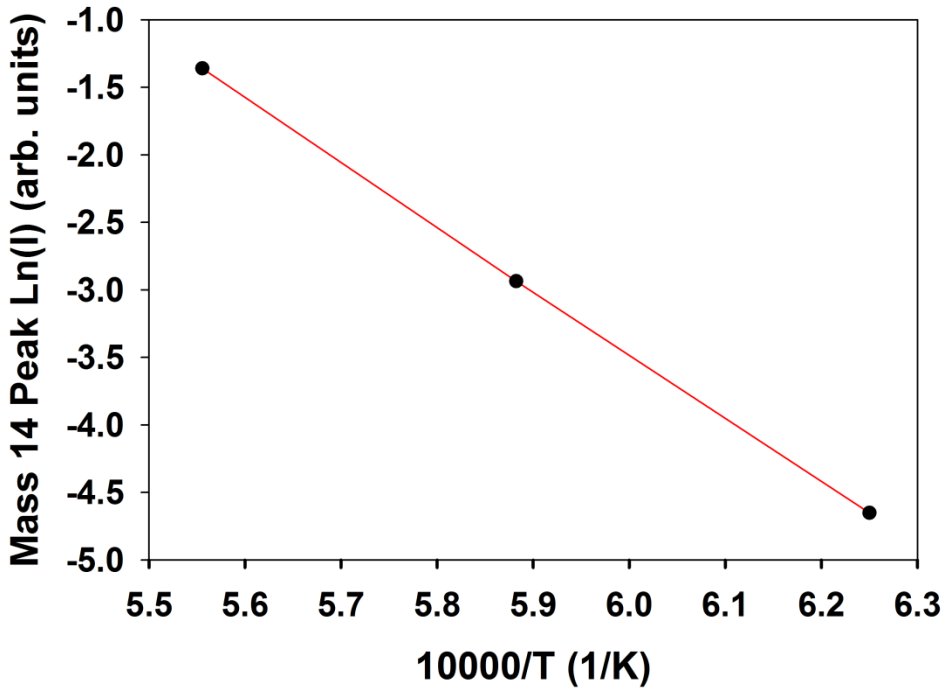

Figure 5.8: Natural logarithm of Mass 14 ($^{28}Si^{2+}$) vs. inverse of temperature.

5.3.4 X-ray photoelectron spectroscopic depth profiling

Samples used for the experiments in previous sections, as a consequence of prolonged heating at high temperatures, graphitize very readily. This is confirmed with the XPS analysis of newly graphitized sample prepared by heating SiC at ~ 1700 °C for 11900 seconds (198.3 minutes) in UHV. The XPS spectra are shown in Figures 5.9 and 5.10.

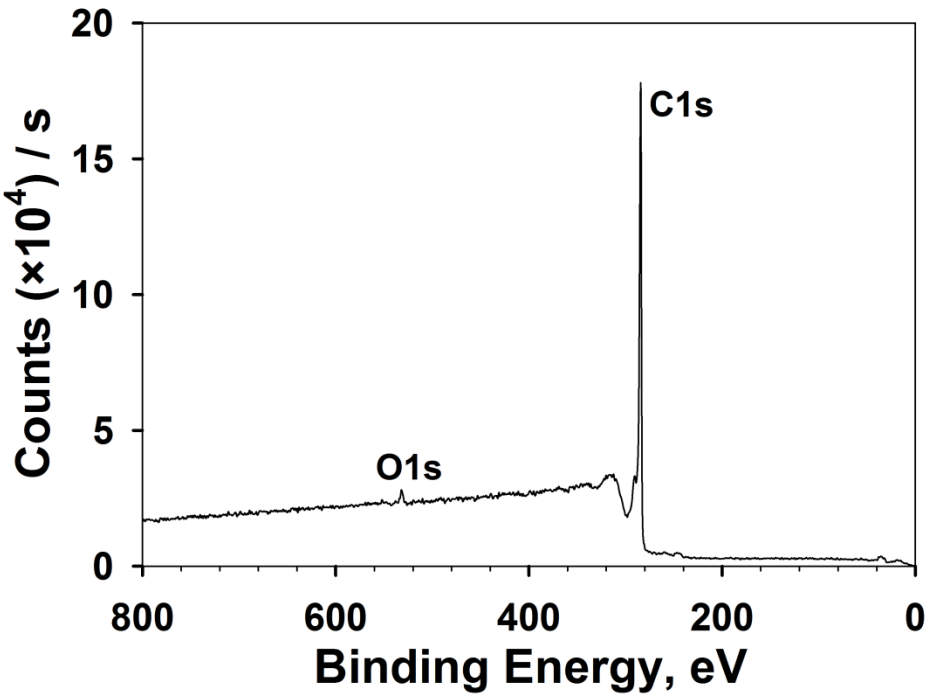

Figure 5.9: Survey XPS analysis of the C-face SiC after being heated at 1700 °C for 11900s in UHV

Figure 5.9 illustrates the elemental composition of the film's surface, with atomic percent of carbon being 98.8 % and oxygen 1.2 %. The observed oxygen can be attributed to surface contamination due to transport of the sample from the growth chamber to the XPS chamber. Figure 5.10 illustrates in detail the C1s peak. It is clear that the surface is graphite as evidenced by the dominant sp^2 hybridized carbon peak at

~ 284.6 eV. The peak corresponding to sp^3 hybridized carbon is observed at ~ 285.1 eV. Due to the oxygen contamination on the surface, peaks corresponding to epoxy or hydroxyl functionalities are observed at ~ 287.6 eV. Lastly, the peak due to π-π* shake-up, observed at ~ 291.4 eV, further confirms the graphitized nature of the film.

Figure 5.11, depicts the Raman spectroscopic analysis of another UHV graphitized SiC sample. This serves as an additional confirmation that the produced material is graphite. In fact, it can also be referred to as multilayer randomly oriented graphene or turbostratic graphite. This is confirmed by the presence of a prominent G' peak at ~ 2691 cm^{-1} that can be fit with a single Lorentzian with a full width at half maximum of ~ 72 cm^{-1}. The graphitized material is clearly defective as evident from the presence of the D peak at ~ 1345 cm^{-1}. SEM analysis (Figure 5.12) confirms the porous nature of the grown film, which contributes to the observed intensity of the defect peak (D-band) in the Raman spectrum in Figure 5.11.

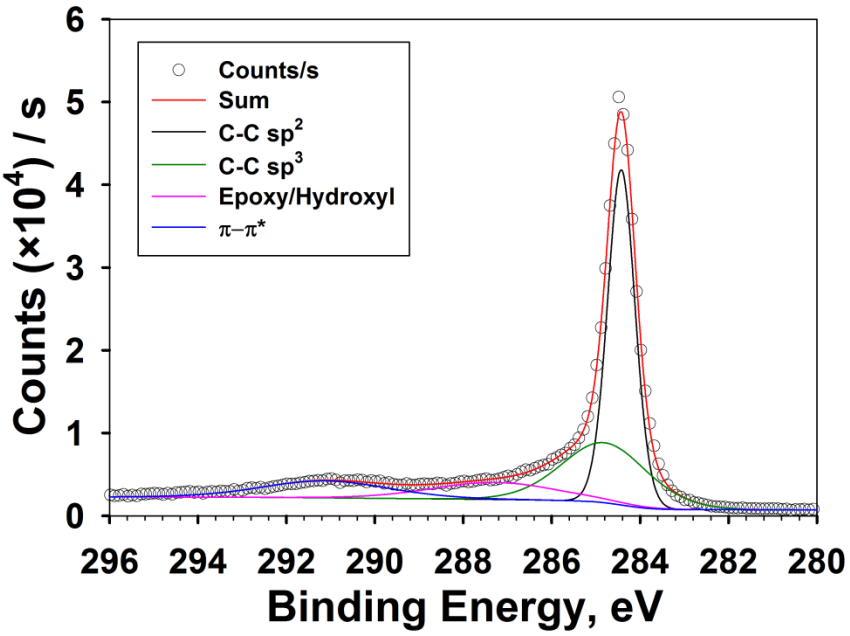

Figure 5.10: C1s peak XPS analysis of the C-face SiC after being heated at 1700 °C for 11900s in UHV.

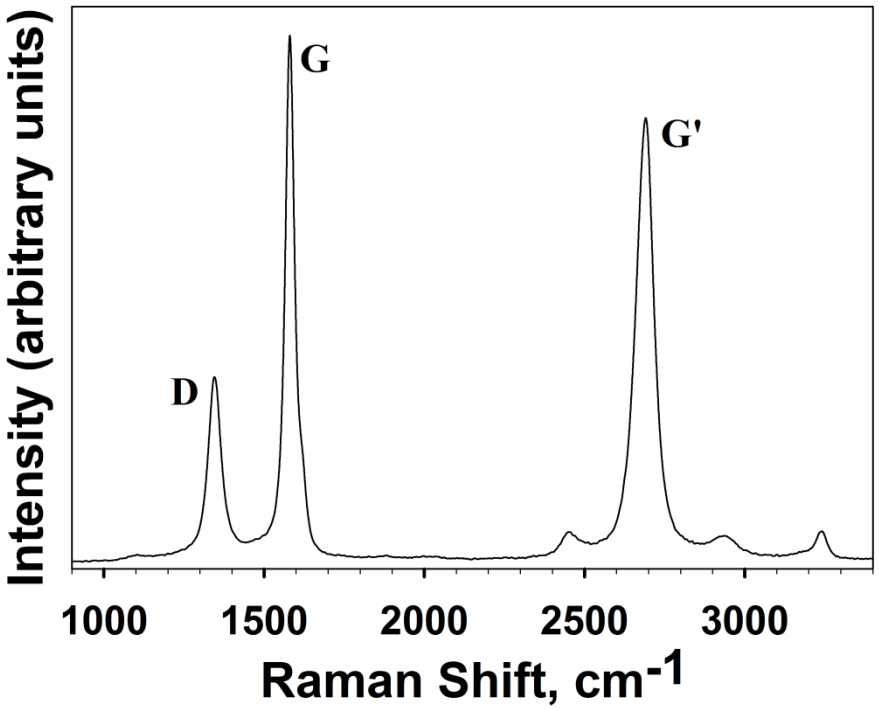

Figure 5.11: Raman spectroscopic analysis of SiC, graphitized at ~ 1700 °C for ~ 7500s in the ultra-high vacuum.

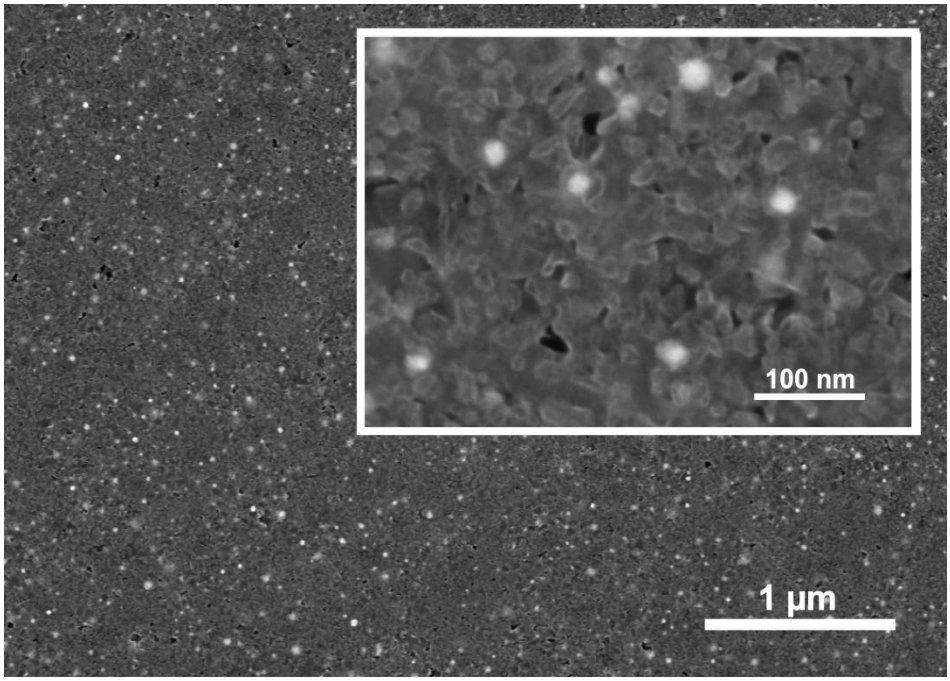

Figure 5.12: SEM analysis of SiC, graphitized at ~ 1700 °C for ~ 7500s in UHV. The inset is a magnified view of the film.

Because of the ease of SiC graphitization at high temperatures in UHV, it is useful to determine the graphitization rate at the conditions used in this chapter's experiments. X-ray photoelectron spectroscopic (XPS) depth profiling is performed with the same system described in Chapter 4. The sample is etched with an Ar ion beam at a rate of ~ 10.69 nm/s and the atomic percentages of carbon and silicon species are plotted as a function of etch depth in Figure 5.13. It is determined that after 198.3 minutes of growth time at ~ 1700 °C, C-face SiC builds up ~ 35.515 µm of multilayer graphene, which at this thickness should be more appropriately termed graphite. This value is determined from the point of intersection of two curves corresponding to carbon and silicon species in Figure 5.13. This means that the rate of graphitization is ~ 2.98 nm/s. With a reported graphene thickness value of ~ 0.335 nm [143], the growth rate then equals ~ 8.89 layers per second for C-face SiC at 1700 °C in UHV.

The chemical evolution of carbon and silicon peaks during the Ar ion depth profiling is demonstrated in Figure 5.14. Transition from graphite to SiC as a function of the etch depth is clearly observed in Figure 5.14a. Transition from the dispersed silicon in graphite to SiC is presented in Figure 5.14b.

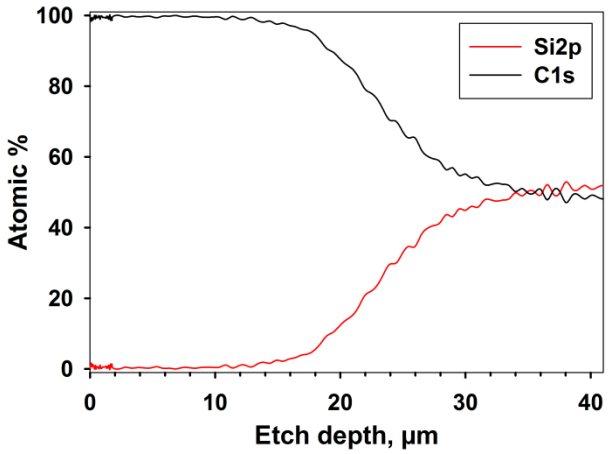

Figure 5.13: C-face SiC XPS depth profiling after 11900s heating at 1700 °C in UHV.

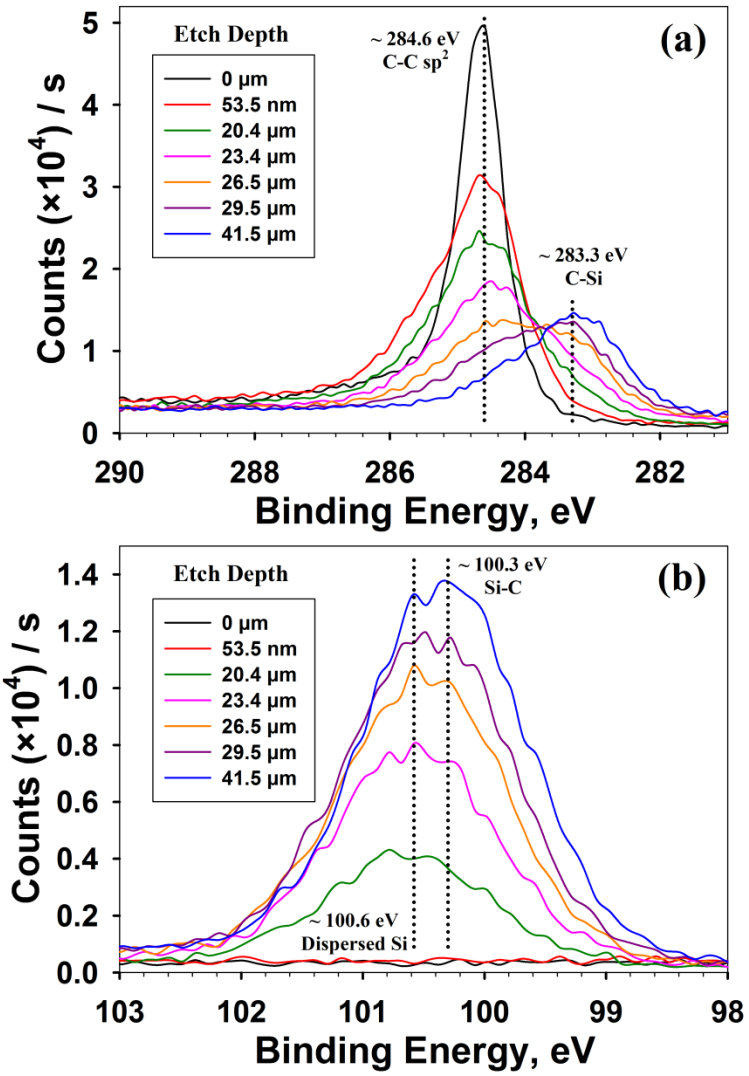

Figure 5.14: Evolution of (a) C1s and (b) Si2p peaks during the XPS depth profiling of the graphitized SiC sample, prepared by being heated at 1700 °C in UHV for 11900s.

Figure 5.13 also reveals that silicon and carbon are not distributed evenly throughout the graphite layer. The first ~ 12.376 µm of the graphite film contains ~ 99 % carbon. The thickness of this layer corresponds to ~ 34.85 % of the total thickness of the graphite film. The remaining ~ 65.15 % of the film is composed of the mixture of silicon and carbon species with an increasing percentage of each. It is important to note that, due to the inhomogeneity in the Ar ion beam etched graphite layer, there can be variability in

the measured relative percentages of silicon and carbon distribution. An alternative depth profiling approach with an added capability of determining the exact nature of silicon and carbon containing species in the graphite film would utilize time-of-flight secondary ion mass spectrometry (ToF-SIMS). Figure 5.15 demonstrates the SEM images and the corresponding Raman spectra of the of the Ar ion beam etched SiC graphitized at 1700 °C in UHV for 11900s. Due to the gaussian profile of the ion beam, the area in Figure 5.15f is the recipient of the majority of the Ar ion flux. Figure 5.13 was, in fact, produced by collecting C1s and Si2p spectra from this region during the depth profiling procedure. Other regions of the etched SiC (Figure 5.15b and 5.15d) can serve as representations of what the surface of graphitized SiC would look like at different stages of etching, due to a decreased ion flux and, therefore, a slower etch rate at those areas.

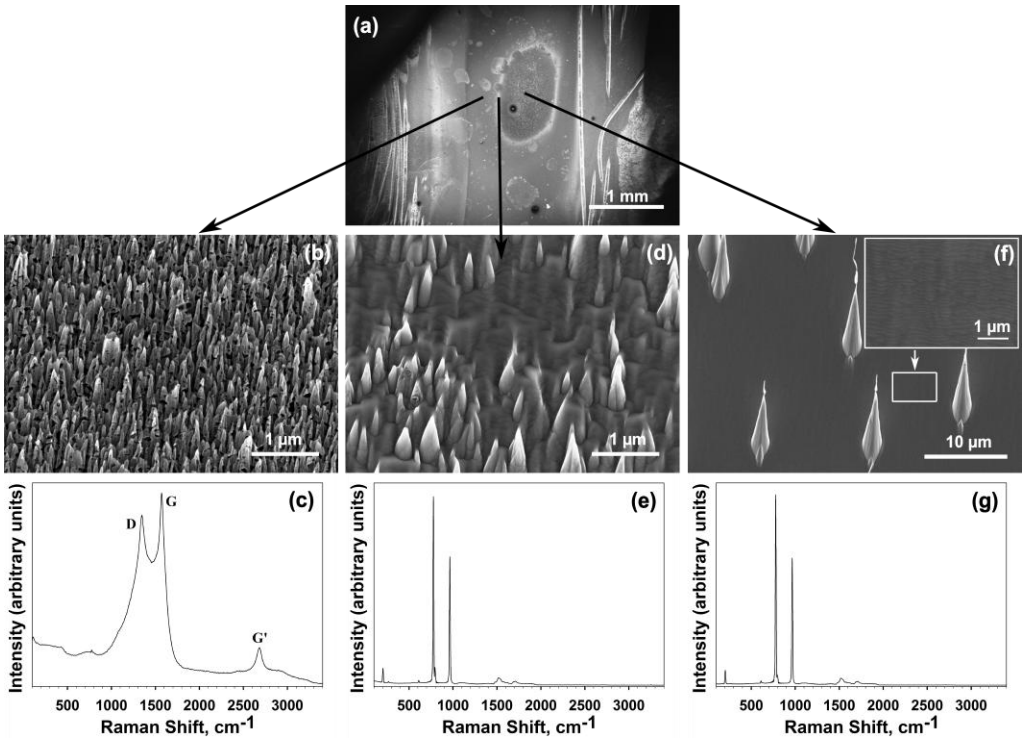

Figure 5.15: SEM and Raman analysis of the Ar ion beam etched graphitized SiC film grown at 1700 °C in UHV for 11900s. (a) Depiction of the etched graphitized SiC with three distinct areas. (b,c) (d,e) (f,g) SEM images and the corresponding Raman spectra of the etched regions in (a).

The corresponding Raman spectroscopic analysis of these regions indicates the transition from the fully graphitized SiC (Figure 5.11), to partially etched defective graphitic layer (Figure 5.15c), to finally pure 4H-SiC substrate (Figure 5.15e and 5.15g).

5.4 Conclusions

In summary, the study described in this chapter utilizes quadrupole mass spectrometry (QMS) for investigating the nature of the subliming species from the carbon face of silicon carbide (C-face SiC) heated to high temperatures in an ultra-high vacuum (UHV) chamber. It is determined that the dominant subliming species at 1800 °C is $^{28}Si^{+}$. Other fragments belonging to carbon and SiC are also observed. It is also determined that at 1700 °C, after the initial decline in silicon sublimation rate due to the buildup of graphene layers, either the underlying SiC crystal or graphene layers undergo a transformation (probably reconstruction and/or formation of grain boundaries) that results in a renewed increased rate of silicon sublimation. The origin of this transformation is not known, but it is most likely related to the release of stresses associated with rapid growth of graphene layers. The rate of graphene growth is also identified based on the X-ray photoelectron spectroscopic depth profiling analysis of the C-face SiC sample heated at 1700 °C for 198.3 minutes. It is determined to be ~ 2.98 nm/s or ~ 8.89 layers per second. The silicon sublimation energy is also determined, by performing mass spectrometric analysis of the subliming silicon as a function of temperature. The silicon energy of sublimation is calculated to be ~ 5.5 eV, which is in close agreement with the value reported in the literature.

CHAPTER VI

CONCLUDING REMARKS AND FUTURE OUTLOOK

Graphene holds a lot of promise as a technologically relevant material. Novel applications that use it directly or as part of hybrid structures are reported with an encouraging frequency. This interest is fueling other areas of research in two dimensional materials, prompting researchers to take a closer look at many already well known materials that are known to have layered structures similar to graphite. Though scientists have already developed procedures for producing graphene, there are limitations to each one, specifically in regards to scalability, quality, and cost of production. Therefore, there is still a need for developing novel methodologies for producing graphene and graphene like materials that would overcome the limitations of current approaches.

Graphite oxide is thought to be a promising candidate for graphene-like material production. Chapters 2 and 4 of this Thesis introduced methods for producing graphitic materials via graphite oxide reduction with laser and 3 keV Ar ion beam irradiation, respectively. The final products were extensively characterized with spectroscopic (Raman and X-ray photoelectron spectroscopies), microscopic (scanning electron microscopy) and electrical characterization techniques. In both reduction approaches nearly 100% removal of oxygen containing functionalities is achieved. In the case of laser reduction approach, formation of randomly oriented multilayer graphene (sometimes referred to as turbostratic graphite) is demonstrated. Both reduction approaches produce sp^2 hybridized carbon materials that have low sheet resistance values between ~ 100-2500 Ω/sq. In addition, 3 keV Ar ion beam approach creates unique

surface morphology (nanocones and nanopores) during the graphite oxide reduction procedure, depending on the angle of irradiation.

Incorporation of graphene and graphene-like materials into devices can lead to their faster commercialization. One such device, specifically broadband light sensor, based on the laser reduced graphite oxide-unreduced graphite oxide system is described in chapter 3. It is determined that the efficiency of light conversion to electrical current increases when low oxygen (~ 18%) content graphite oxide is used as a starting material. Future research would focus on further investigation of the physics governing the charge carrier dynamics upon exposure of that material to light. Improvements of this device can be made by producing hybrid structures with other materials.

Another promising substrate for graphene growth is silicon carbide (SiC). Chapter 1 introduced the reader to this method. Though this approach has been known for some time now, the detailed understanding of the mechanisms governing graphene growth are not completely understood. Therefore, Chapter 5 was dedicated to the investigation of these mechanisms with the aid of the quadrupole mass spectrometry (QMS) and X-ray photoelectron spectroscopy (XPS). During high temperature graphitization of SiC in ultra-high vacuum (UHV) environment the release of the subliming species was monitored as a function of temperature and time. It was determined that silicon was the dominant subliming specie, though other atomic and molecular species were observed as well (carbon clusters and silicon carbide fragments). When the subliming species were monitored as a function of time, an unexpected phenomenon was observed to occur when SiC was heated continuously at 1700 °C. After the initial prolonged expected steady decline in the amount of subliming silicon, the rate

of silicon sublimation suddenly rapidly increases almost to the initial values. This behavior is thought to be a result of surface transformation to achieve lower energy state. In the process of the surface transformation new pathways for silicon escape open up, resulting in an observed increase of silicon sublimation. By monitoring the amounts of the subliming silicon as a function of temperature, the energy of silicon sublimation was determined to be ~ 5.5 eV. Also, Ar ion beam depth profiling, coupled with XPS analysis, revealed that thick layer of graphite can be readily grown on SiC in UHV at high temperatures and the distribution of carbon and silicon is non-uniform throughout that film.

The work presented in this Thesis has wider reaching applications then that related to just graphene research. Carbon and oxygen are some of the most abundant chemical elements in space. It is therefore expected that graphite oxide is also very common. The processes described in chapters 2 and 4 have direct relevance to the processing of graphite oxide in space with intense photon and ion radiation. This radiation induced modification of graphite oxide can trigger chemical reactions with other simple organic molecules leading to the formation of larger biologically relevant complex organic compounds. This investigation is something that should be done in the future as well.

REFERENCES

[1] L. J. Cote, F. Kim, J. Huang, "Langmuir−Blodgett Assembly of Graphite Oxide Single Layers," *Journal of the American Chemical Society*, 2008, vol. 131, no. 3, pp. 1043-1049.

[2] S. Bae, H. Kim, Y. Lee, X. Xu, J.-S. Park, Y. Zheng, et al., "Roll-to-roll production of 30-inch graphene films for transparent electrodes," *Nat Nano*, 2010, vol. 5, no. 8, pp. 574-578.

[3] P. R. Wallace, "The Band Theory of Graphite," *Physical Review*, 1947, vol. 71, no. 9, pp. 622-634.

[4] H. P. Boehm, A. Clauss, U. Hofmann, G. O. Fischer, "Dunnste Kohlenstoff-Folien," *Zeitschrift Fur Naturforschung Part B-Chemie Biochemie Biophysik Biologie Und Verwandten Gebiete*, 1962, vol. B 17, no. 3, pp. 150-153.

[5] K. S. Novoselov, A. K. Geim, S. V. Morozov, D. Jiang, Y. Zhang, S. V. Dubonos, et al., "Electric field effect in atomically thin carbon films," *Science*, 2004, vol. 306, no. 5696, pp. 666-669.

[6] D. V. Kosynkin, A. L. Higginbotham, A. Sinitskii, J. R. Lomeda, A. Dimiev, B. K. Price, et al., "Longitudinal unzipping of carbon nanotubes to form graphene nanoribbons," *Nature*, 2009, vol. 458, no. 7240, pp. 872-876.

[7] D. Xia, Q. Z. Xue, J. Xie, H. J. Chen, C. Lv, F. Besenbacher, et al., "Fabrication of Carbon Nanoscrolls from Monolayer Graphene," *Small*, 2010, vol. 6, no. 18, pp. 2010-2019.

[8] L. Y. Chu, Q. Z. Xue, T. Zhang, C. C. Ling, "Fabrication of Carbon Nanoscrolls from Mono layer Graphene Controlled by P-Doped Silicon Nanowires: A MD Simulation Study," *J Phys Chem C*, 2011, vol. 115, no. 31, pp. 15217-15224.

[9] A. Chuvilin, U. Kaiser, E. Bichoutskaia, N. A. Besley, A. N. Khlobystov, "Direct transformation of graphene to fullerene," *Nat Chem*, 2010, vol. 2, no. 6, pp. 450-453.

[10] C. Lee, X. D. Wei, J. W. Kysar, J. Hone, "Measurement of the elastic properties and intrinsic strength of monolayer graphene," *Science*, 2008, vol. 321, no. 5887, pp. 385-388.

[11] A. A. Balandin, S. Ghosh, W. Bao, I. Calizo, D. Teweldebrhan, F. Miao, et al., "Superior Thermal Conductivity of Single-Layer Graphene," *Nano Letters*, 2008, vol. 8, no. 3, pp. 902-907.

[12] T. R. Anthony, W. F. Banholzer, J. F. Fleischer, L. Wei, P. K. Kuo, R. L. Thomas, et al., "Thermal diffusivity of isotopically enriched ^{12}C diamond," *Physical Review B*, 1990, vol. 42, no. 2, pp. 1104-1111.

[13] X. S. Wu, Y. K. Hu, M. Ruan, N. K. Madiomanana, J. Hankinson, M. Sprinkle, et al., "Half integer quantum Hall effect in high mobility single layer epitaxial graphene," *Appl Phys Lett*, 2009, vol. 95, no. 22, pp. 223108.

[14] A. J. Van Bommel, J. E. Crombeen, A. Van Tooren, "LEED and Auger electron observations of the SiC(0001) surface," *Surface Science*, 1975, vol. 48, no. 2, pp. 463-472.

[15] C. Berger, Z. Song, T. Li, X. Li, A. Y. Ogbazghi, R. Feng, et al., "Ultrathin Epitaxial Graphite: 2D Electron Gas Properties and a Route toward Graphene-based Nanoelectronics," *The Journal of Physical Chemistry B*, 2004, vol. 108, no. 52, pp. 19912-19916.

[16] X. S. Li, W. W. Cai, J. H. An, S. Kim, J. Nah, D. X. Yang, et al., "Large-Area Synthesis of High-Quality and Uniform Graphene Films on Copper Foils," *Science*, 2009, vol. 324, no. 5932, pp. 1312-1314.

[17] A. Reina, X. T. Jia, J. Ho, D. Nezich, H. B. Son, V. Bulovic, et al., "Large Area, Few-Layer Graphene Films on Arbitrary Substrates by Chemical Vapor Deposition," *Nano Letters*, 2009, vol. 9, no. 1, pp. 30-35.

[18] G. D. Ruan, Z. Z. Sun, Z. W. Peng, J. M. Tour, "Growth of Graphene from Food, Insects, and Waste," *ACS Nano*, 2011, vol. 5, no. 9, pp. 7601-7607.

[19] Z. Z. Sun, Z. Yan, J. Yao, E. Beitler, Y. Zhu, J. M. Tour, "Growth of graphene from solid carbon sources," *Nature*, 2010, vol. 468, no. 7323, pp. 549-552.

[20] G.-X. Ni, Y. Zheng, S. Bae, C. Y. Tan, O. Kahya, J. Wu, et al., "Graphene–Ferroelectric Hybrid Structure for Flexible Transparent Electrodes," *ACS Nano*, 2012, vol. 6, no. 5, pp. 3935-3942.

[21] J. B. Wu, H. A. Becerril, Z. N. Bao, Z. F. Liu, Y. S. Chen, P. Peumans, "Organic solar cells with solution-processed graphene transparent electrodes," *Appl Phys Lett*, 2008, vol. 92, no. 26, pp. 263302.

[22] S. Vadukumpully, J. Paul, N. Mahanta, S. Valiyaveettil, "Flexible conductive graphene/poly(vinyl chloride) composite thin films with high mechanical strength and thermal stability," *Carbon*, 2011, vol. 49, no. 1, pp. 198-205.

[23] U. Khan, K. Young, A. O'Neill, J. N. Coleman, "High strength composite fibres from polyester filled with nanotubes and graphene," *Journal of Materials Chemistry*, 2012, vol. 22, no. 25, pp. 12907-12914.

[24] S. Stankovich, D. A. Dikin, G. H. B. Dommett, K. M. Kohlhaas, E. J. Zimney, E. A. Stach, et al., "Graphene-based composite materials," *Nature*, 2006, vol. 442, no. 7100, pp. 282-286.

[25] L. Huang, Y. Huang, J. J. Liang, X. J. Wan, Y. S. Chen, "Graphene-based conducting inks for direct inkjet printing of flexible conductive patterns and their applications in electric circuits and chemical sensors," *Nano Res*, 2011, vol. 4, no. 7, pp. 675-684.

[26] D. Prasai, J. C. Tuberquia, R. R. Harl, G. K. Jennings, K. I. Bolotin, "Graphene: Corrosion-Inhibiting Coating," *ACS Nano*, 2012, vol. 6, no. 2, pp. 1102-1108.

[27] N. T. Kirkland, T. Schiller, N. Medhekar, N. Birbilis, "Exploring graphene as a corrosion protection barrier," *Corrosion Science*, 2012, vol. 56, no. 0, pp. 1-4.

[28] S. Chen, L. Brown, M. Levendorf, W. Cai, S.-Y. Ju, J. Edgeworth, et al., "Oxidation Resistance of Graphene-Coated Cu and Cu/Ni Alloy," *ACS Nano*, 2011, vol. 5, no. 2, pp. 1321-1327.

[29] X. Miao, S. Tongay, M. K. Petterson, K. Berke, A. G. Rinzler, B. R. Appleton, et al., "High Efficiency Graphene Solar Cells by Chemical Doping," *Nano Letters*, 2012, vol. 12, no. 6, pp. 2745-2750.

[30] H. Gilgueng, J. C. Acosta, E. Vela, S. Haliyo, S. Regnier. Graphene as thin film infrared optoelectronic sensor. Optomechatronic Technologies, 2009 ISOT 2009 International Symposium on; p. 169-174.

[31] L. King Wai Chiu, X. Ning, C. K. M. Fung, C. Hongzhi, C. Liangliang, Y. RuiGuo, et al. Uncooled infrared sensing using graphene. Nanotechnology Materials and Devices Conference (NMDC), 2011 IEEE; p. 98-101.

[32] R. K. Paul, S. Badhulika, N. M. Saucedo, A. Mulchandani, "Graphene Nanomesh As Highly Sensitive Chemiresistor Gas Sensor," *Analytical Chemistry*, 2012, vol. 84, no. 19, pp. 8171-8178.

[33] S. Rumyantsev, G. Liu, M. S. Shur, R. A. Potyrailo, A. A. Balandin, "Selective Gas Sensing with a Single Pristine Graphene Transistor," *Nano Letters*, 2012, vol. 12, no. 5, pp. 2294-2298.

[34] T. Kuila, S. Bose, P. Khanra, A. K. Mishra, N. H. Kim, J. H. Lee, "Recent advances in graphene-based biosensors," *Biosensors and Bioelectronics*, 2011, vol. 26, no. 12, pp. 4637-4648.

[35] Y. Huang, X. Dong, Y. Liu, L.-J. Li, P. Chen, "Graphene-based biosensors for detection of bacteria and their metabolic activities," *Journal of Materials Chemistry*, 2011, vol. 21, no. 33, pp. 12358-12362.

[36] Y. Shao, J. Wang, H. Wu, J. Liu, I. A. Aksay, Y. Lin, "Graphene Based Electrochemical Sensors and Biosensors: A Review," *Electroanalysis*, 2010, vol. 22, no. 10, pp. 1027-1036.

[37] B. C. Brodie, " On the atomic weight of graphite," *Philosophical Transactions of the Royal Society of London*, 1859, vol. 149, no. 249-259.

[38] W. S. Hummers, R. E. Offeman, "Preparation of graphitic oxide," *Journal of the American Chemical Society*, 1958, vol. 80, no. 6, pp. 1339-1339.

[39] J. A. Yan, L. D. Xian, M. Y. Chou, "Structural and Electronic Properties of Oxidized Graphene," *Physical Review Letters*, 2009, vol. 103, no. 8, pp. 086802.

[40] S. Gilje, S. Han, M. Wang, K. L. Wang, R. B. Kaner, "A chemical route to graphene for device applications," *Nano Letters*, 2007, vol. 7, no. 11, pp. 3394-3398.

[41] J.-H. Chen, C. Jang, S. Xiao, M. Ishigami, M. S. Fuhrer, "Intrinsic and extrinsic performance limits of graphene devices on SiO2," *Nat Nano*, 2008, vol. 3, no. 4, pp. 206-209.

[42] S. Stankovich, R. D. Piner, X. Chen, N. Wu, S. T. Nguyen, R. S. Ruoff, "Stable aqueous dispersions of graphitic nanoplatelets via the reduction of exfoliated graphite oxide in the presence of poly(sodium 4-styrenesulfonate)," *Journal of Materials Chemistry*, 2006, vol. 16, no. 2, pp. 155-158.

[43] D. C. Marcano, D. V. Kosynkin, J. M. Berlin, A. Sinitskii, Z. Sun, A. Slesarev, et al., "Improved Synthesis of Graphene Oxide," *ACS Nano*, 2010, vol. 4, no. 8, pp. 4806-4814.

[44] I. Y. Jeon, Y. R. Shin, G. J. Sohn, H. J. Choi, S. Y. Bae, J. Mahmood, et al., "Edge-carboxylated graphene nanosheets via ball milling," *Proc Natl Acad Sci U S A*, 2012, vol. 109, no. 15, pp. 5588-5593.

[45] H.-J. Shin, K. K. Kim, A. Benayad, S.-M. Yoon, H. K. Park, I.-S. Jung, et al., "Efficient Reduction of Graphite Oxide by Sodium Borohydride and Its Effect on Electrical Conductance," *Advanced Functional Materials*, 2009, vol. 19, no. 12, pp. 1987-1992.

[46] S. Pei, J. Zhao, J. Du, W. Ren, H.-M. Cheng, "Direct reduction of graphene oxide films into highly conductive and flexible graphene films by hydrohalic acids," *Carbon*, 2010, vol. 48, no. 15, pp. 4466-4474.

[47] H. A. Becerril, J. Mao, Z. Liu, R. M. Stoltenberg, Z. Bao, Y. Chen, "Evaluation of solution-processed reduced graphene oxide films as transparent conductors," *ACS Nano*, 2008, vol. 2, no. 3, pp. 463-470.

[48] T. Ghosh, C. Biswas, J. Oh, G. Arabale, T. Hwang, N. D. Luong, et al., "Solution-Processed Graphite Membrane from Reassembled Graphene Oxide," *Chemistry of Materials*, 2012, vol. 24, no. 3, pp. 594-599.

[49] H. C. Schniepp, J.-L. Li, M. J. McAllister, H. Sai, M. Herrera-Alonso, D. H. Adamson, et al., "Functionalized Single Graphene Sheets Derived from Splitting Graphite Oxide," *The Journal of Physical Chemistry B*, 2006, vol. 110, no. 17, pp. 8535-8539.

[50] Z. Q. Wei, D. B. Wang, S. Kim, S. Y. Kim, Y. K. Hu, M. K. Yakes, et al., "Nanoscale Tunable Reduction of Graphene Oxide for Graphene Electronics," *Science*, 2010, vol. 328, no. 5984, pp. 1373-1376.

[51] L. J. Cote, R. Cruz-Silva, J. X. Huang, "Flash Reduction and Patterning of Graphite Oxide and Its Polymer Composite," *Journal of the American Chemical Society*, 2009, vol. 131, no. 31, pp. 11027-11032.

[52] V. Eswaraiah, S. S. J. Aravind, S. Ramaprabhu, "Top down method for synthesis of highly conducting graphene by exfoliation of graphite oxide using focused solar radiation," *Journal of Materials Chemistry*, 2011, vol. 21, no. 19, pp. 6800-6803.

[53] Y. M. Shul'ga, V. N. Vasilets, S. A. Baskakov, V. E. Muradyan, E. A. Skryleva, Y. N. Parkhomenko, "Photoreduction of Graphite Oxide Nanosheets with Vacuum Ultraviolet Radiation," *High Energy Chem*, 2012, vol. 46, no. 2, pp. 117-121.

[54] V. Abdelsayed, S. Moussa, H. M. Hassan, H. S. Aluri, M. M. Collinson, M. S. El-Shall, "Photothermal Deoxygenation of Graphite Oxide with Laser Excitation in Solution and Graphene-Aided Increase in Water Temperature," *J Phys Chem Lett*, 2010, vol. 1, no. 19, pp. 2804-2809.

[55] W. Gao, N. Singh, L. Song, Z. Liu, A. L. M. Reddy, L. J. Ci, et al., "Direct laser writing of micro-supercapacitors on hydrated graphite oxide films," *Nat Nanotechnol*, 2011, vol. 6, no. 8, pp. 496-500.

[56] L. Huang, Y. Liu, L. C. Ji, Y. Q. Xie, T. Wang, W. Z. Shi, "Pulsed laser assisted reduction of graphene oxide," *Carbon*, 2011, vol. 49, no. 7, pp. 2431-2436.

[57] D. A. Sokolov, K. R. Shepperd, T. M. Orlando, "Formation of Graphene Features from Direct Laser-Induced Reduction of Graphite Oxide," *J Phys Chem Lett*, 2010, vol. 1, no. 18, pp. 2633-2636.

[58] Y. L. Zhang, L. Guo, S. Wei, Y. Y. He, H. Xia, Q. D. Chen, et al., "Direct imprinting of microcircuits on graphene oxides film by femtosecond laser reduction," *Nano Today*, 2010, vol. 5, no. 1, pp. 15-20.

[59] Y. Zhou, Q. L. Bao, B. Varghese, L. A. L. Tang, C. K. Tan, C. H. Sow, et al., "Microstructuring of Graphene Oxide Nanosheets Using Direct Laser Writing," *Adv Mater*, 2010, vol. 22, no. 1, pp. 67-71.

[60] D. A. Sokolov, C. M. Rouleau, D. B. Geohegan, T. M. Orlando, "Excimer laser reduction and patterning of graphite oxide," *Carbon*, 2013, vol. 53, no. 0, pp. 81-89.

[61] K. R. Shepperd. Low-energy electron induced processes in hydrocarbon films adsorbed on silicon surfaces. Doctoral thesis. Georgia Institute of Technology, Atlanta, GA. 2009.

[62] L. Chen, Z. Xu, J. Li, C. Min, L. Liu, X. Song, et al., "Reduction and disorder in graphene oxide induced by electron-beam irradiation," *Materials Letters*, 2011, vol. 65, no. 8, pp. 1229-1230.

[63] Q. Wang, J. Li, Y. Song, X. Wang, "Facile Synthesis of High-Quality Plasma-Reduced Graphene Oxide with Ultrahigh 4,4′-Dichlorobiphenyl Adsorption Capacity," *Chemistry – An Asian Journal*, 2013, vol. 8, no. 1, pp. 225-231.

[64] S. W. Lee, C. Mattevi, M. Chhowalla, R. M. Sankaran, "Plasma-Assisted Reduction of Graphene Oxide at Low Temperature and Atmospheric Pressure for Flexible Conductor Applications," *The Journal of Physical Chemistry Letters*, 2012, vol. 3, no. 6, pp. 772-777.

[65] J. W. Suk, R. D. Piner, J. An, R. S. Ruoff, "Mechanical Properties of Monolayer Graphene Oxide," *ACS Nano*, 2010, vol. 4, no. 11, pp. 6557-6564.

[66] H. Bai, K. Sheng, P. Zhang, C. Li, G. Shi, "Graphene oxide/conducting polymer composite hydrogels," *Journal of Materials Chemistry*, 2011, vol. 21, no. 46, pp. 18653-18658.

[67] H. Feng, Y. Li, J. Li, "Strong reduced graphene oxide-polymer composites: hydrogels and wires," *RSC Advances*, 2012, vol. 2, no. 17, pp. 6988-6993.

[68] W. Gao, N. Singh, L. Song, Z. Liu, A. L. M. Reddy, L. Ci, et al., "Direct laser writing of micro-supercapacitors on hydrated graphite oxide films," *Nat Nano*, 2011, vol. 6, no. 8, pp. 496-500.

[69] M. F. El-Kady, V. Strong, S. Dubin, R. B. Kaner, "Laser Scribing of High-Performance and Flexible Graphene-Based Electrochemical Capacitors," *Science*, 2012, vol. 335, no. 6074, pp. 1326-1330.

[70] J. Liu, Y. Xue, L. Dai, "Sulfated Graphene Oxide as a Hole-Extraction Layer in High-Performance Polymer Solar Cells," *The Journal of Physical Chemistry Letters*, 2012, vol. 3, no. 14, pp. 1928-1933.

[71] J.-M. Yun, J.-S. Yeo, J. Kim, H.-G. Jeong, D.-Y. Kim, Y.-J. Noh, et al., "Solution-Processable Reduced Graphene Oxide as a Novel Alternative to PEDOT:PSS Hole Transport Layers for Highly Efficient and Stable Polymer Solar Cells," *Adv Mater*, 2011, vol. 23, no. 42, pp. 4923-4928.

[72] S. H. Choi, H. M. Ju, S. H. Huh, C. K. Song, S. H. Park, B. M. Kim, "A Catalytic Graphene Oxide Film for a Dye-sensitized Solar Cell," *J Korean Phys Soc*, 2010, vol. 57, no. 6, pp. 1653-1656.

[73] S. Gurunathan, J. W. Han, A. A. Dayem, V. Eppakayala, J. H. Kim, "Oxidative stress-mediated antibacterial activity of graphene oxide and reduced graphene oxide in Pseudomonas aeruginosa," *Int J Nanomed*, 2012, vol. 7, no. 5901-5914.

[74] S. B. Liu, M. Hu, T. H. Zeng, R. Wu, R. R. Jiang, J. Wei, et al., "Lateral Dimension-Dependent Antibacterial Activity of Graphene Oxide Sheets," *Langmuir*, 2012, vol. 28, no. 33, pp. 12364-12372.

[75] X. M. Sun, Z. Liu, K. Welsher, J. T. Robinson, A. Goodwin, S. Zaric, et al., "Nano-Graphene Oxide for Cellular Imaging and Drug Delivery," *Nano Res*, 2008, vol. 1, no. 3, pp. 203-212.

[76] X. Yang, Y. Wang, X. Huang, Y. Ma, Y. Huang, R. Yang, et al., "Multi-functionalized graphene oxide based anticancer drug-carrier with dual-targeting function and pH-sensitivity," *Journal of Materials Chemistry*, 2011, vol. 21, no. 10, pp. 3448-3454.

[77] Y. Zhang, B. Chen, L. Zhang, J. Huang, F. Chen, Z. Yang, et al., "Controlled assembly of Fe3O4 magnetic nanoparticles on graphene oxide," *Nanoscale*, 2011, vol. 3, no. 4, pp. 1446-1450.

[78] J. Shen, Y. Hu, M. Shi, N. Li, H. Ma, M. Ye, "One Step Synthesis of Graphene Oxide−Magnetic Nanoparticle Composite," *The Journal of Physical Chemistry C*, 2010, vol. 114, no. 3, pp. 1498-1503.

[79] G. Zhu, Y. Liu, Z. Xu, T. Jiang, C. Zhang, X. Li, et al., "Flexible Magnetic Nanoparticles–Reduced Graphene Oxide Composite Membranes Formed by Self-Assembly in Solution," *ChemPhysChem*, 2010, vol. 11, no. 11, pp. 2432-2437.

[80] A. Y. Romanchuk, A. S. Slesarev, S. N. Kalmykov, D. V. Kosynkin, J. M. Tour, "Graphene oxide for effective radionuclide removal," *Physical Chemistry Chemical Physics*, 2013, vol. 15, no. 7, pp. 2321-2327.

[81] V. Chandra, J. Park, Y. Chun, J. W. Lee, I.-C. Hwang, K. S. Kim, "Water-Dispersible Magnetite-Reduced Graphene Oxide Composites for Arsenic Removal," *ACS Nano*, 2010, vol. 4, no. 7, pp. 3979-3986.

[82] G. Sheng, Y. Li, X. Yang, X. Ren, S. Yang, J. Hu, et al., "Efficient removal of arsenate by versatile magnetic graphene oxide composites," *RSC Advances*, 2012, vol. 2, no. 32, pp. 12400-12407.

[83] S. R. J. Brueck. There are No Fundamental Limits to Optical Lithography. In: Guenther AH, ed. International Trends in Applied Optics: SPIE Press 2002, p. 85-86.

[84] Q. F. Xia, S. Y. Chou, "Applications of excimer laser in nanofabrication," *Appl Phys A-Mater Sci Process*, 2010, vol. 98, no. 1, pp. 9-59.

[85] L. Li, M. Hong, M. Schmidt, M. Zhong, A. Malshe, B. Huis in'tVeld, et al., "Laser nano-manufacturing – State of the art and challenges," *CIRP Annals - Manufacturing Technology*, 2011, vol. 60, no. 2, pp. 735-755.

[86] M. J. Fernández-Merino, J. I. Paredes, S. Villar-Rodil, L. Guardia, P. Solís-Fernández, D. Salinas-Torres, et al., "Investigating the influence of surfactants on the stabilization of aqueous reduced graphene oxide dispersions and the characteristics of their composite films," *Carbon*, 2012, vol. 50, no. 9, pp. 3184-3194.

[87] A. C. Ferrari, J. C. Meyer, V. Scardaci, C. Casiraghi, M. Lazzeri, F. Mauri, et al., "Raman spectrum of graphene and graphene layers," *Physical Review Letters*, 2006, vol. 97, no. 18, pp. 187401.

[88] D. Graf, F. Molitor, K. Ensslin, C. Stampfer, A. Jungen, C. Hierold, et al., "Spatially resolved raman spectroscopy of single- and few-layer graphene," *Nano Letters*, 2007, vol. 7, no. 2, pp. 238-242.

[89] L. M. Malard, M. A. Pimenta, G. Dresselhaus, M. S. Dresselhaus, "Raman spectroscopy in graphene," *Physics Reports*, 2009, vol. 473, no. 5–6, pp. 51-87.

[90] D. R. Lenski, M. S. Fuhrer, "Raman and optical characterization of multilayer turbostratic graphene grown via chemical vapor deposition," *J Appl Phys*, 2011, vol. 110, no. 1, pp. 013720-013724.

[91] L. G. Cancado, K. Takai, T. Enoki, M. Endo, Y. A. Kim, H. Mizusaki, et al., "General equation for the determination of the crystallite size L-a of nanographite by Raman spectroscopy," *Appl Phys Lett*, 2006, vol. 88, no. 16, pp. 163106-163109.

[92] A. C. Ferrari, "Raman spectroscopy of graphene and graphite: Disorder, electron-phonon coupling, doping and nonadiabatic effects," *Solid State Communications*, 2007, vol. 143, no. 1-2, pp. 47-57.

[93] M. Lenner, A. Kaplan, R. E. Palmer, "Nanoscopic Coulomb explosion in ultrafast graphite ablation," *Appl Phys Lett*, 2007, vol. 90, no. 15, pp. 3.

[94] L. J. Van der Pauw, "A method of measuring specific resistivity and Hall effect of discs of arbitrary shape," *Philips Res Repts*, 1958, vol. 13, no. 1, pp. 1-9.

[95] G. Eda, G. Fanchini, M. Chhowalla, "Large-area ultrathin films of reduced graphene oxide as a transparent and flexible electronic material," *Nat Nano*, 2008, vol. 3, no. 5, pp. 270-274.

[96] S. Park, J. An, R. D. Piner, I. Jung, D. Yang, A. Velamakanni, et al., "Aqueous Suspension and Characterization of Chemically Modified Graphene Sheets," *Chemistry of Materials*, 2008, vol. 20, no. 21, pp. 6592-6594.

[97] T. S. Sreeprasad, A. K. Samal, T. Pradeep, "Tellurium Nanowire-Induced Room Temperature Conversion of Graphite Oxide to Leaf-like Graphenic Structures," *The Journal of Physical Chemistry C*, 2009, vol. 113, no. 5, pp. 1727-1737.

[98] F. Carbone, P. Baum, P. Rudolf, A. H. Zewail, "Structural preablation dynamics of graphite observed by ultrafast electron crystallography," *Physical Review Letters*, 2008, vol. 100, no. 3, pp. 035501.

[99] M. Lenner, A. Kaplan, C. Huchon, R. E. Palmer, "Ultrafast laser ablation of graphite," *Physical Review B*, 2009, vol. 79, no. 18, pp. 184105.

[100] H. Zhang, Y. Miyamoto, "Graphene production by laser shot on graphene oxide: An ab initio prediction (vol 85, 033402, 2012)," *Physical Review B*, 2012, vol. 85, no. 8, pp. 089901(E).

[101] H. Zhang, Y. Miyamoto, "Graphene production by laser shot on graphene oxide: An ab initio prediction," *Physical Review B*, 2012, vol. 85, no. 3, pp. 033402-033406.

[102] N. Itoh, A. M. Stoneham, "Materials modification by electronic excitation," *Radiation Effects and Defects in Solids*, 2001, vol. 155, no. 1-4, pp. 277-290.

[103] B. Angleraud, J. Aubreton, A. Catherinot, "Expansion of the ablation plume created by ultraviolet laser irradiation of various target materials," *European Physical Journal-Applied Physics*, 1999, vol. 5, no. 3, pp. 303-310.

[104] I. Jung, D. A. Field, N. J. Clark, Y. W. Zhu, D. X. Yang, R. D. Piner, et al., "Reduction Kinetics of Graphene Oxide Determined by Electrical Transport Measurements and Temperature Programmed Desorption," *J Phys Chem C*, 2009, vol. 113, no. 43, pp. 18480-18486.

[105] Z. Y. Chen, A. Vertes, "Early plume expansion in atmospheric pressure midinfrared laser ablation of water-rich targets," *Physical Review E*, 2008, vol. 77, no. 3, pp. 036316.

[106] A. A. Puretzky, D. B. Geohegan, R. E. Haufler, R. L. Hettich, X. Y. Zheng, R. N. Compton. Laser-Ablation of Graphite in Different Buffer Gases. In: Miller JC, Geohegan DB, eds. Laser Ablation: Mechanisms and Applications - II. Woodbury: Aip Press 1994, p. 365-374.

[107] Y. M. Shulga, V. M. Martynenko, V. E. Muradyan, S. A. Baskakov, V. A. Smirnov, G. L. Gutsev, "Gaseous products of thermo- and photo-reduction of graphite oxide," *Chem Phys Lett*, 2010, vol. 498, no. 4-6, pp. 287-291.

[108] X. Kong, Y. Huang, Y. Chen, "Difference in formation of carbon cluster cations by laser ablation of graphene and graphene oxide," *Journal of Mass Spectrometry*, 2012, vol. 47, no. 4, pp. 523-528.

[109] X. L. Kong, S. Q. Li, S. Zhang, Y. Huang, Y. S. Cheng, "Large Carbon Cluster Anions Generated by Laser Ablation of Graphene," *J Am Soc Mass Spectrom*, 2011, vol. 22, no. 11, pp. 2033-2041.

[110] M. Lenner, A. Kaplan, C. Huchon, R. E. Palmer, "Ultrafast laser ablation of graphite," *Physical Review B*, 2009, vol. 79, no. 18, pp. 184105- 184116.

[111] A. Das, S. Pisana, B. Chakraborty, S. Piscanec, S. K. Saha, U. V. Waghmare, et al., "Monitoring dopants by Raman scattering in an electrochemically top-gated graphene transistor," *Nat Nanotechnol*, 2008, vol. 3, no. 4, pp. 210-215.

[112] G. Eda, M. Chhowalla, "Chemically Derived Graphene Oxide: Towards Large-Area Thin-Film Electronics and Optoelectronics," *Adv Mater*, 2010, vol. 22, no. 22, pp. 2392-2415.

[113] F. Xia, T. Mueller, Y.-m. Lin, A. Valdes-Garcia, P. Avouris, "Ultrafast graphene photodetector," *Nat Nano*, 2009, vol. 4, no. 12, pp. 839-843.

[114] Y. Lin, K. Zhang, W. Chen, Y. Liu, Z. Geng, J. Zeng, et al., "Dramatically Enhanced Photoresponse of Reduced Graphene Oxide with Linker-Free Anchored CdSe Nanoparticles," *ACS Nano*, 2010, vol. 4, no. 6, pp. 3033-3038.

[115] F. T. Vasko, V. Ryzhii, "Voltage and temperature dependencies of conductivity in gated graphene," *Physical Review B*, 2007, vol. 76, no. 23, pp. 233404.

[116] F. Rana, P. A. George, J. H. Strait, J. Dawlaty, S. Shivaraman, M. Chandrashekhar, et al., "Carrier recombination and generation rates for intravalley and intervalley phonon scattering in graphene," *Physical Review B*, 2009, vol. 79, no. 11, pp. 115447.

[117] A. Jorio, R. Saito, G. Dresselhaus, M. Dresselhaus. Raman spectroscopy in graphene related systems. Weihheim: Wiley-Vch Verlag GmbH 2011, p. 329.

[118] F. Y. Xie, L. Gong, X. Liu, Y. T. Tao, W. H. Zhang, S. H. Chen, et al., "XPS studies on surface reduction of tungsten oxide nanowire film by Ar+ bombardment," *Journal of Electron Spectroscopy and Related Phenomena*, 2012, vol. 185, no. 3–4, pp. 112-118.

[119] P. Ghosh, M. Z. Yusop, S. Satoh, M. Subramanian, A. Hayashi, Y. Hayashi, et al., "Transparent and Flexible Field Electron Emitters Based on the Conical Nanocarbon Structures," *Journal of the American Chemical Society*, 2010, vol. 132, no. 12, pp. 4034-4035.

[120] W. E. Vanderlinde, A. L. Ruoff, "Reactive ion beam etching of polyimide thin films," *J Vac Sci Technol B*, 1988, vol. 6, no. 6, pp. 1621-1625.

[121] T. Okumoto, J. Taniguchi, Y. Kamiya, "Fabrication of carbon nanofibers using only ion beam irradiation to glassy carbon," *Microelectronic Engineering*, 2011, vol. 88, no. 8, pp. 1832-1835.

[122] [cited 02/05/2013]; Available from: http://equipment.lboro.ac.uk/item/x-ray-photoelectron-spectrometer/2121/image/images.jpg

[123] M. A. Pimenta, G. Dresselhaus, M. S. Dresselhaus, L. G. Cancado, A. Jorio, R. Saito, "Studying disorder in graphite-based systems by Raman spectroscopy," *Physical Chemistry Chemical Physics*, 2007, vol. 9, no. 11, pp. 1276-1290.

[124] A. M. Ektessabi, K. Yamaguchi, "Changes in chemical states of PET films due to low and high energy oxygen ion beam," *Thin Solid Films*, 2000, vol. 377–378, no. 0, pp. 793-797.

[125] S. Pylypenko, K. Artyushkova, J. E. Fulghum, "Application of XPS spectral subtraction and multivariate analysis for the characterization of Ar^+ ion beam

modified polyimide surfaces," *Applied Surface Science*, 2010, vol. 256, no. 10, pp. 3204-3210.

[126] J. W. Lee, T. H. Kim, S. H. Kim, C. Y. Kim, Y. H. Yoon, J. S. Lee, et al., "Investigation of ion bombarded polymer surfaces using SIMS, XPS and AFM," *Nuclear Instruments and Methods in Physics Research Section B: Beam Interactions with Materials and Atoms*, 1997, vol. 121, no. 1–4, pp. 474-479.

[127] A. Miyawaki, M. Zamri, T. Hayashi, Y. Hayashi, M. Tanemura, T. Tokunaga, "Fabrication of Ge nanoneedles by ion-irradiation method," *Surface and Coatings Technology*, 2011, vol. 206, no. 5, pp. 812-815.

[128] M. Tanemura, T. Okita, J. Tanaka, M. Kitazawa, K. Itoh, M. Lei, et al., "Room-Temperature Growth and Applications of Carbon Nanofibers: A Review," *Nanotechnology, IEEE Transactions on*, 2006, vol. 5, no. 5, pp. 587-594.

[129] M. Tanemura, J. Tanaka, K. Itoh, Y. Fujimoto, Y. Agawa, L. Miao, et al., "Field electron emission from sputter-induced carbon nanofibers grown at room temperature," *Appl Phys Lett*, 2005, vol. 86, no. 11, pp. 113107.

[130] C. Berger, Z. M. Song, X. B. Li, X. S. Wu, N. Brown, C. Naud, et al., "Electronic confinement and coherence in patterned epitaxial graphene," *Science*, 2006, vol. 312, no. 5777, pp. 1191-1196.

[131] W. A. de Heer, C. Berger, M. Ruan, M. Sprinkle, X. B. Li, Y. K. Hu, et al., "Large area and structured epitaxial graphene produced by confinement controlled sublimation of silicon carbide," *Proc Natl Acad Sci U S A*, 2011, vol. 108, no. 41, pp. 16900-16905.

[132] R. Zhang, Y. L. Dong, W. J. Kong, W. P. Han, P. H. Tan, Z. M. Liao, et al., "Growth of large domain epitaxial graphene on the C-face of SiC," *J Appl Phys*, 2012, vol. 112, no. 10, pp. 104307.

[133] H. Hu, A. Ruammaitree, H. Nakahara, K. Asaka, Y. Saito, "Few-layer epitaxial graphene with large domains on C-terminated 6H-SiC," *Surface and Interface Analysis*, 2012, vol. 44, no. 6, pp. 793-796.

[134] M. L. Bolen, S. E. Harrison, L. B. Biedermann, M. A. Capano, "Graphene formation mechanisms on 4H-SiC(0001)," *Physical Review B*, 2009, vol. 80, no. 11, pp. 115433.

[135] L. B. Biedermann, M. L. Bolen, M. A. Capano, D. Zemlyanov, R. G. Reifenberger, "Insights into few-layer epitaxial graphene growth on 4H-SiC(000(1)over-bar substrates from STM studies," *Physical Review B*, 2009, vol. 79, no. 12, pp. 125411.

[136] G. G. Jernigan, B. L. VanMil, J. L. Tedesco, J. G. Tischler, E. R. Glaser, A. Davidson, et al., "Comparison of Epitaxial Graphene on Si-face and C-face 4H SiC Formed by Ultrahigh Vacuum and RF Furnace Production," *Nano Letters*, 2009, vol. 9, no. 7, pp. 2605-2609.

[137] W. A. de Heer, C. Berger, X. S. Wu, P. N. First, E. H. Conrad, X. B. Li, et al., "Epitaxial graphene," *Solid State Communications*, 2007, vol. 143, no. 1-2, pp. 92-100.

[138] C. Virojanadara, M. Syvajarvi, R. Yakimova, L. I. Johansson, A. A. Zakharov, T. Balasubramanian, "Homogeneous large-area graphene layer growth on 6H-SiC(0001)," *Physical Review B*, 2008, vol. 78, no. 24, pp. 245403.

[139] J. S. Moon, D. Curtis, M. Hu, D. Wong, C. McGuire, P. M. Campbell, et al., "Epitaxial-Graphene RF Field-Effect Transistors on Si-Face 6H-SiC Substrates," *IEEE Electron Device Lett*, 2009, vol. 30, no. 6, pp. 650-652.

[140] N. Srivastava, H. Guowei, Luxmi, P. C. Mende, R. M. Feenstra, S. Yugang, "Graphene formed on SiC under various environments: comparison of Si-face and C-face," *Journal of Physics D: Applied Physics*, 2012, vol. 45, no. 15, pp. 154001.

[141] E. Velez-Fort, C. Mathieu, E. Pallecchi, M. Pigneur, M. G. Silly, R. Belkhou, et al., "Epitaxial Graphene on 4H-SiC(0001) Grown under Nitrogen Flux: Evidence of Low Nitrogen Doping and High Charge Transfer," *ACS Nano*, 2012, vol. 6, no. 12, pp. 10893-10900.

[142] H. Sadowski, R. Helbig, "Sublimation studies of SiC by using a quadrupole mass spectrometer," *J Electrochem Soc*, 1998, vol. 145, no. 10, pp. 3556-3560.

[143] Z. H. Ni, H. M. Wang, J. Kasim, H. M. Fan, T. Yu, Y. H. Wu, et al., "Graphene Thickness Determination Using Reflection and Contrast Spectroscopy," *Nano Letters*, 2007, vol. 7, no. 9, pp. 2758-2763.